Search for oscillations between axion-like particles and very high energy gamma rays in the H.E.S.S. spectrum of M87

Master´s Thesis in Physics

Presented by

Phillip Beck

Submission date: 14.09.2021

Erlangen Centre for Astroparticle Physics
Physikalisches Institut
Friedrich-Alexander-Universität
Erlangen-Nürnberg

Supervisor: Prof. Dr. Stefan Funk

Acknowledgements

I would like to thank Manuel Meyer, who looked after me during the past year despite all the difficulties. He always supported me with advice and played a major role in the realization of this work.

My very special thanks go to my wife Christine, without whom I would never have survived the last year!

Abstract

Since the realization that many cosmological observations cannot be explained if the universe consists exclusively of visible matter, so-called dark matter has been one of the major research areas in astrophysics. Another unsolved mystery of physics is that of the unobserved violation of CP symmetry in quantum chromodynamics. The new particle called axion, or its generalization of axion-like particles (ALP), that emerged from a proposed solution to this "strong CP problem" would be a candidate for dark matter if it had suitable mass and coupling strength to the electromagnetic field. A photon can transform into an ALP when traversing a coherent magnetic field. In this work, an attempt is made to detect this effect. To do so, high-energy photons observed by the High Energy Stereoscopic System Telecope (H.E.S.S.), which are produced in the jet of the active galactic nucleus of the galaxy M87 in the Virgo galaxy cluster, are examined for traces of these conversions. The generated gamma photons pass through large-scale magnetic fields that traverse the galaxy cluster on their way to Earth. The exact structure of these magnetic fields is unknown and must be modeled using observations of the electromagnetic spectrum received from this region. This model can be used to calculate the theoretical conversion of photons into ALPs. Spectral analysis of the H.E.S.S. data and a subsequent statistical analysis allow an assessment of whether or not the received spectrum of the M87 AGN was modulated by ALP. Two conclusions can be drawn from the results of this work. First, there appears to be a slight preference for assuming such modulation. Second, there is evidence that only statistical fluctuations of the spectrum were overfitted. With a larger amount of spectral data, as well as more refined models, the approach of this work could serve as a basis to effectively search for photon ALP oscillations in the spectra of active Galactic nuclei in the future.

Kurzfassung

Seit der Erkenntnis, dass sich viele kosmologische Beobachtungen nicht erklären lassen, falls das Universum ausschließlich aus sichtbare Materie besteht, ist die sogenannte dunkle Materie eines der großen Forschungsgebiete der Astrophysik. Ein weiteres ungelöstes Rätsel der Physik ist das der nicht beobachteten Verletzung der CP Symmetrie in der Quantenchromodynamik. Das aus einem Lösungsvorschlag für dieses „starke CP Problem“ hervorgegangene neue Teilchen namens Axion bzw. seine Verallgemeinerung der Axion-artigen Teilchen (ALP) wäre bei geeigneter Masse und Kopplungsstärke an das elektromagnetische Feld ein Kandidat für dunkle Materie. Ein Photon kann sich bei der Durchquerung eines kohärenten Magnetfeldes in ein ALP umwandeln. In dieser Arbeit wird versucht diesen Effekt nachzuweisen. Dafür werden die vom High Energy Stereoscopic System Telekop (H.E.S.S.) beobachteten hochenergetischen Photonen, die im Jet des aktiven galaktischen Kerns der Galaxie M87 im Virgo Galaxienkluster entstehen, auf Spuren dieser Umwandlungen untersucht. Die erzeugten Gammaphotonen durchlaufen auf ihrem Weg zur Erde großflächige Magnetfelder, die den Galaxienkluster durchziehen. Die genaue Struktur dieser Magnetfelder ist unbekannt und muss mit Hilfe von Beobachtungen des aus diesem Gebiet empfangenen elektromagnetischen Spektrums modelliert werden. Mit diesem Modell kann die theoretische Umwandlung von Photonen in ALPs berechnet werden. Die Spektralanalyse der H.E.S.S. Daten und eine anschließende statistische Auswertung ermöglichen eine Einschätzung, ob das empfangene Spektrum des M87 AGN durch ALP moduliert wurde oder nicht. Die Ergebnisse dieser Arbeit lassen zwei Schlüsse zu. Zum einen scheint es eine leichte Bevorzugung der Annahme einer solchen Modulation zu geben. Zum anderen gibt es Anzeichen, dass nur statistische Fluktuationen des Spektrums überfittet wurden. Mit einer größeren Menge an spektralen Daten sowie verfeinerten Modellen könnte der Ansatz dieser Arbeit als Grundlage dazu dienen, in Zukunft effektiv nach Photon-ALP Oszillationen in den Spektren aktiver galaktischer Kerne zu suchen.

Contents

1. Introduction

Physics has come a long way since its development from natural philosophy. It has done a remarkable job in describing nature and increasing our understanding of why things are the way they are. In particular, the world beyond our perception, that is, the world in the very smallest and the very largest is the subject of modern physics.
The latter is already investigated since centuries by astrophysics and increased with a plethora of discoveries and models our understanding of the cosmos. Examples are the models of celestial mechanics worked out by Gallileo, Copernicus and Keppler (Keppler's laws) as well as the astronomical discoveries of Halley (Halley's comet), Friedrich Herrschel (compilation of a double star catalog and theoretical structure of the Milky Way) and Edwin Hubble (description of the recessional velocity of galaxies). Further discoveries in the 20th century like those of radio emission from our home galaxy (Jansky, 1931), the cosmic background radiation (Penzias, Wilson, 1964) as well as black holes (from their postulation as "dark stars" by John Mitchell 1783 over the theoretical bases of Albert Einstein, Karls Schwarzschild and Subrahmanyan Chandrasekhar in the 20's and Robert Oppenheimer, 1939, up to the first discovery 1972 with Cygnus X-1) contributed to extend our picture of the cosmos. With the tremendously rapid development of methods to receive an ever-widening spectrum of electromagnetic radiation from the depths of space, more sophisticated models were developed that continue to push the limits of our knowledge. In many astrophysical processes light is emitted, which covers the complete spectrum of electromagnetic radiation. Thus, for light in the range of radio waves over visible light to x-rays or gamma radiation, there are different ground or satellite-based detectors that are sensitive in the respective range.

Let us temporarily turn our backs on astrophysics and instead turn our attention to the world at its smallest. The natural philosophical concept of a smallest unit of which our whole world should consist already appeared in ancient Greece and was the basis of atomism (atomos = indivisible). After that it remained quiet for a long time around the not yet developed field of particle physics. At the end of the 19th century it was found out that these smallest units called atoms were not as indivisible as thought. At first Sir Joseph John Thomson and some other physicists discovered the negatively charged electron and at the beginning of the 20th century Rutherford's gold foil experiment proved the positively charged atomic nucleus (see Rutherford's atomic model). With the help of quantum mechanics, which was emerging at the same time, and the accompanying consideration of spin, quantum statistics and symmetry groups, the knowledge of atomic and subatomic structures could be further refined. Many of the particles predicted in quantum theory, such as the positron or the neutrino, could later be detected with the help of particle accelerators or the studies of cosmic rays. Cosmic rays are particles (primarily protons and light atomic nuclei) that come from space and collide with the Earth's atmosphere to produce detectable showers of light secondary particles (such as electrons, muons, and photons). Increasingly powerful particle accelerators and modern quantum field theory brought particle physics to its present state, which is condensed in the Standard Model of particle physics. This consists, at present, of 22 elementary particles (thus particles, which cannot be further divided according to today's knowledge) which are divided into fermions (half-integer spin) and bosons (whole-integer spin). The fermions include the quarks (the building blocks of atomic nuclei) and the leptons (the family of electrons and the associated neutrinos). The carriers of the four elementary forces (photon - electromagnetic force, W and Z bosons - weak interaction, gluons - strong interaction and the not yet discovered graviton - gravitational force) as well as the recently discovered Higgs boson belong to the group of bosons. The example of the discovery of the Higgs boson (2012 at the Large Hadron Collider, CERN) shows that many particles, which were already predicted by theoretical physics (for example based on symmetry considerations), could only be experimentally detected much later with sufficiently powerful technology.

So now we have the standard model of particle physics, which describes the world in the very smallest and the (multispectral) astrophysics, which brings us closer to the cosmos, i.e. the world in the very largest. That means, we can lean back contentedly, right? Far from it, because there are still many stubborn problems in physics. From the many unsolved riddles of physics there are two of them, which are of special interest in this work. There is on the one hand the problem of the missing (visible) mass in the universe. Some observations, like the formation of galaxies in general, the orbital velocity of outer stars around the center of their galaxy and the gravitational lensing effect (where light is deflected by extremely high masses) cannot be explained if it is assumed that the visible mass represents the total mass of the universe. Currently, it is assumed that only about one sixth of the total matter in the universe is visible and accounted for in the Standard Model. The remaining matter is provided by the so-called dark matter, which resists any discovery until today. The second problem which is to be illuminated here lurks in the depths of the quantum field theory. As already described, symmetries play an important role in physics. Symmetries can be as vivid as the rotational symmetry (continuous symmetry) or the mirror symmetry (discrete symmetry) but also more abstract like the charge conjugation (reversal of the sign of the electric charge) or the combination of several symmetries like the mirror symmetry and the charge conjugation (also called charge parity symmetry). If a physical system is changed (transformed) with respect to such a symmetry without changing its state, it is said to be invariant with respect to this symmetry transformation. If this invariance is cancelled by small fluctuations, one speaks of symmetry breaking. So far it has been shown that nature breaks the symmetry of physical systems in which this is theoretically allowed. In the case of the CP symmetry of the strong interaction, which the theory admits a symmetry breaking, this symmetry breaking has not been discovered until today.

The solution to this so-called strong CP problem, as well as a potential candidate for dark matter, could be a new particle called an axion, or axion-like particle (ALP). ALPs can be converted from photons when they pass through a magnetic field, which makes the basic setup of experiments to detect them very simple in principle. The fact that these particles have not been detected until today shows that there must be some considerable difficulties. On the one hand, there is the extremely small assumed mass of the ALPs and on the other hand their minimal interaction with other particles of the standard model and the rare events of the transformation which go along with it. Energy and number of photons, strength of the magnetic field as well as the interaction length between photons and magnetic field are the determining factors of corresponding experiments. In this work we will consider photons from the bright center of the Virgo galaxy cluster, which on their way to us pass through a magnetic field that traverses the cluster. In the observations of the photons arriving at Earth, we will try to detect signs of photon - ALP conversions.

Chapter 2 first elaborates the theory of ALPs, addressing both the motivation for their postulation and the mathematics behind the mixing between photons and ALPs. In the last section of the chapter, the different types of existing experiments for their detection are briefly described. We receive light from the entire electromagnetic spectrum from the Virgo Cluster (in particular from the central galaxy M87). Which parts of the spectrum are interesting for our purpose and how photons of the corresponding energy can be detected is explained in chapter 3, as well as the relevant environmental conditions of the Virgo Cluster. In chapter 4 the model assumptions of the "experimental environment" of the Virgo Cluster are worked out and finally, based on the resulting model, the conversion probabilities of photons to ALPs are calculated. In the 5th chapter, statistical methods are used to analyze whether real measurements from a telescope pointed at M87 justify the existence of ALPs.

2. Axions and axion-like particles

Axions and axion-like particles, particles that have been the subject of intense physical research for about 50 years. Their discovery could not only solve one of the great physical mysteries. Postulated in 1973 as a possible solution to the great CP problem, the axion quickly became the subject of numerous experiments. Important properties of axions are the strength with which they couple to particles of the Standard Model and their mass. If these properties are in a suitable region, they are potential candidates for dark matter. By extending the axion model to a larger group of particles, the axion-like particles (ALPs), experiments could search for them in the complete parameter space of coupling strength and mass. The coupling of axions to photons is of particular interest for this search because our detection methods for electromagnetic radiation are well developed. In the first section of this chapter, we first discuss in more detail the motivations of the axion and its generalization to the ALP. In the second section, we consider the coupling of the ALP to the electromagnetic field and the mathematical formulation of the photon - ALP mixing. In the last section we discuss three important types of experiments for the detection of ALP.

2.1. Strong CP problem

Symmetry violation

"If a system has a continuous symmetry property, then there are corresponding quantities whose values are conserved in time". The importance of Noether's theorem (E. Noether, 1918) for physics and thus of the concept of symmetry cannot be overstated. In the following, however, we will not deal with continuous symmetries and conservation variables, but with discrete symmetries and their violation. The important symmetries of particle physics are:

1. charge conjugation (C), where each particle is replaced by its antiparticle
2. parity transformation (P), where each particle is mirrored on a coordinate axis, and
3. time reversal symmetry (T), where the time course direction is reversed.

The phenomenon is called symmetry breaking, when a physical system is at a metastable point with respect to a symmetry and decides by minimal fluctuations, which branch of a bifurcation is taken. If these fluctuations are not observable from the outside, the outcome of this process seems random. Thus, symmetry breaking brings a system from a symmetric but unstable state to a more stable one. In the following, we consider the combination of parity symmetry and charge reversal. The twofold combined CP symmetry was introduced

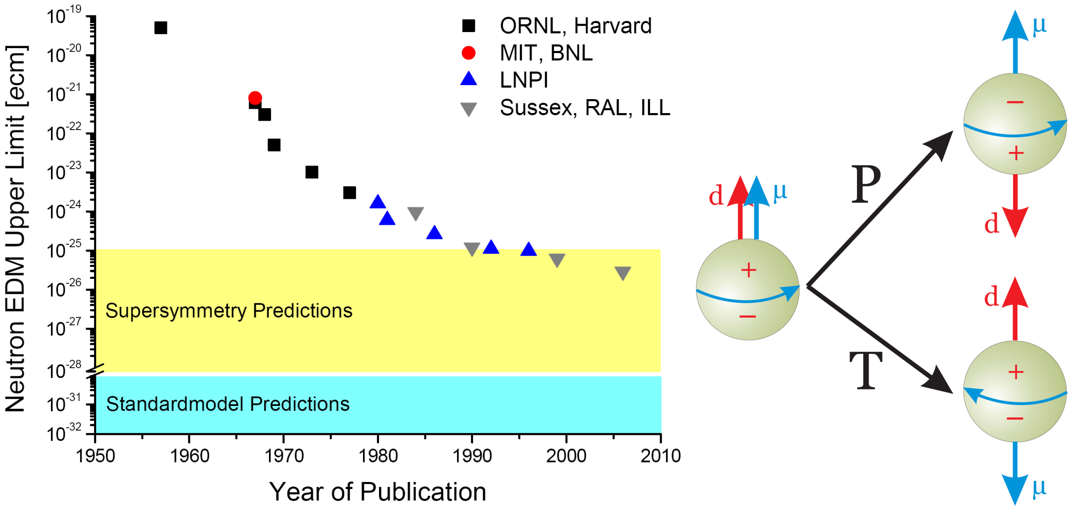

Figure 2.1.: Parity and time-reversal violation due to an electric dipole moment shown on the right side and history of the upper limit on the EDM of the neutron along with the predictions coming from Supersymmetry and the Standard Model are gillustrated on the left side (illustrations created by A. Knecht).

after (Wu, Ambler, Hayward, Hoppes, & Hudson, 1957) proved the violation of parity in the beta decay of cobalt-60. The violation of CP symmetry was finally demonstrated by (Christenson, Cronin, Fitch, & Turlay, 1964) in the electroweak decay of neutral kaons. Also in quantum chromodynamics (QCD), the theory of strong interaction between quarks and gluons, the current mathematical formulation would allow violation of CP symmetry. The mathematical description of a physical system is usually done by means of the Lagrangian function $\mathcal{L} = T - V$, where T stands for the kinetic energy of the system and V for its potential energy. If one chooses a non-zero value for the angle theta in the QCD lagrangian, formulated in equation 2.1, a violation of the CP symmetry would be expected, which, however, is not observed.

Neutron electric dipole moment

An example to experimentally prove the CP violation of QCD is the measurement of the electric dipole moment (EDM) of neutrons. Since the neutron has a non-zero spin and is asymmetric with respect to P and T inversion, it should have a permanent EDM (see figure 2.1 on the right side).

If one makes the usual assumption of invariance with respect to the combined CPT symmetry, this also implies the violation of the CP symmetry. First attempts to find or at least to limit the EDM of the neutron took place already in the 1950s. In these, neutron beams were used which were subjected to a magnetic resonance investigation [Smith1957]. Thereby the experimental limit could be reduced from 5×10^{20} e cm to 3×10^{24} e cm (Dress, Miller, Pendlebury, Perrin, & Ramsey, 1977), where e is the electric charge of the proton. Modern experiments use ultracold neutrons trapped in vacuum chambers with neutron velocities of $7\frac{m}{s}$. Thus, in 2015, the upper limit of the EDM could be reduced to 3.6×10^{-26}e cm (Pendlebury et al., 2015). Further experiments are planned to reduce this limit even further and even actually measure the EDM. The development of the measurement results for the upper limit of the EDM is illustrated in figure 2.1 on the left.

The strong CP problem

The EDM predicted by QCD is approximately $VALUE$, where θ describes the vacuum angle of the QCD Lagrangian. The original QCD Lagrangian is not suitable to address the vacuum properties of the theory sufficiently of the vacuum expectation values. By a suitable Legendre transformation an effective Lagrangian depending on theta can be defined (Halperin & Zhitnitsky, 1998), which reads:

$$\mathcal{L}_{QCD} = -\frac{1}{4} G_{\mu\nu\ a} G_a^{\mu\nu} + \sum_q i\bar{q}\gamma^\mu D_\mu q - qm\bar{q} + \frac{\alpha_s}{8\pi} \theta G_{\mu\nu\ a} \tilde{G}_a^{\mu\nu} \tag{2.1}$$

where $G_{\mu\nu\ a}$ represents the gluon field strength tensor and q,$\bar{q}$ which stands for the three Dirac spinor fields corresponding to the quarks with the three color charges. Furthermore, γ^μ stands for the gamma matrices and D_μ for the covariant derivative. The theta term is Lorentz and gauge invariant and responsible for CP violation. Let

$$q = \begin{pmatrix} u \\ d \end{pmatrix} \tag{2.2}$$

be the quark fields and

$$M = \begin{pmatrix} m_u & 0 \\ 0 & m_d \end{pmatrix} \tag{2.3}$$

the quark mass matrix. If one performs an axial $U(1)_A$ rotation for example at the up-quark

$$u \mapsto e^{i\alpha\gamma^5} u \tag{2.4}$$

it becomes clear that this is chiral, i.e. does not lead to a self-image. The reason for this is that left-handed and right-handed fields transform differently:

$$u_L \mapsto e^{-i\alpha} u_L \ , \ u_R \mapsto e^{i\alpha} u_R \tag{2.5}$$

In such a rotation the quark mass term is not invariant:

$$-m_u \bar{u}_L u_R + h.c. \mapsto -m_u e^{2i\alpha} \bar{u}_L u_R + h.c. \tag{2.6}$$

where the expression $h.c.$ is an abbreviated notation for the hermitian conjugate components. The consequence of equation 2.6 is that under the assumption that the quark mass is nonzero, $U(1)_A$ is not a symmetry in equation 2.4. The $U(1)_A$ symmetry is broken by quantum effects (Adler-Bell-Jackiw anomaly, see (Jackiw, 2008)). Even for the case where massless quarks exist, a $U(1)_A$ rotation would have implications for the theta term of the QCD Lagrangian. Also setting the parameter theta to zero would not solve the problem, because on the one hand the theta term is indispensable for the solution of the $U(1)_A$ problem and on the other hand another contribution to the symmetry breaking comes via the quark mass. For this reason it makes sense to introduce the term

$$\bar{\theta} = \theta + \mathcal{O}(M). \tag{2.7}$$

If one sets the θ-term of the QCD Lagrangian equal to zero, one nevertheless gets a non-zero $\bar{\theta}$. With the limits of the EDM of the neutron discussed in the previous section, one obtains an extremly small upper limit of $\bar{\theta} < 10^{10}$, although this would rather be expected at $\bar{\theta} \sim \mathcal{O}(1)$. This is the strong CP problem.

The Peccei–Quinn aproach

In 1977, Peccei and Quinn presented as a solution to this problem a complex scalar field φ and a new global chiral $U(1)_{PQ}$ symmetry which can rotate $\bar{\theta}$ away (Peccei & Quinn, 1977). The potential associated with ϕ is

$$V(\varphi) = \lambda(|\varphi|^2 - \frac{f_a^2}{2})^2, \tag{2.8}$$

which is shaped like a Mexican hat, as shown in Figure 2.2.

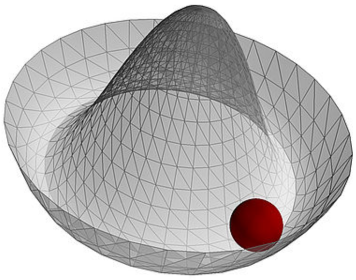

Figure 2.2.: The "mexican hat" shaped PQ potential. The axion field is represented by the red dot. The oscillation of the axion field around the potential minimum gives the axion its mass (Institute for Theoretical Physics Wuppertal).

f_a is the axion decay constant, which was originally set to the electroweak scale (Fermi scale) $f_a \approx 246$GeV. In this case, f_a is related to the vacuum expectation value of φ via $< \varphi >= \frac{f_a}{\sqrt{2}}$.

The spontaneous symmetry breaking of $U(1)_{PQ}$ at eneries $\sim f_a$ gives rise to a Nambu–Goldstone boson ((Nambu, 1960) and (Goldstone, 1961)), the axion a (where $a \sim f_a\bar{\theta}$, see (Weinberg, 1978)). Due to the fact that the axion is assumed to have a mass, it is not a real NG boson. Axion mass and decay constant are related via $m_a \approx \frac{f_\pi m_\pi}{f_a}$, where m_π and f_π stand for mass and decay constant of the pion. This leads to the following numerical relation

$$m_a = 0.6eV \frac{10^7 GeV}{f_a}, \tag{2.9}$$

and to the fact that in this model only one parameter has to be considered (Massó, 2003). By the findings on high energy laboratory experiments the lower limit $f_a > 10^4$GeV or $m_a < 1$keV was determined. If one takes astrophysical considerations, as for example from the analysis of supernova neutrinos (i.e. SN1987A, because there is only one supernova event where neutrinos could be detected), the lower limit is $f_a > 6 \times 10^8$GeV
If one considers still higher values for f_a, which would mean an axion mass in the range $m_a \sim 10^{-3} - 10^{-6}$eV, the axion would be a possible part of the cold dark matter of the universe.
The axion couples to normal matter such as electrons and protons, but also to gauge bosons. On the one hand the coupling to two gluons

$$\mathcal{L}_{agg} = \frac{1}{f_a} \frac{\alpha_s}{8\pi} G \cdot \tilde{G} a \tag{2.10}$$

has to be mentioned, on the other hand the coupling to two photons

$$\mathcal{L}_{a\gamma\gamma} = c_\gamma \frac{\alpha}{\pi f_a} F \cdot \tilde{F} a = -g_{a\gamma\gamma} \vec{E} \vec{B} a. \tag{2.11}$$

In the last two equations α_s stands for the coupling constant of the strong interaction (QCD) and α for the coupling constant of the electromagnetic interaction. F denotes the electromagnetic field strength tensor and $\tilde{F}$ its dual, which is defined via $\tilde{F}^{\mu\nu} = \frac{1}{2}\epsilon^{\mu\nu\alpha\beta} F_{\alpha\beta}$, with $F_{\alpha\beta}$ being the covariant field strength tensor. The parameters c_γ depend on the respective axion model. The coupling described by $\mathcal{L}_{a\gamma\gamma}$ is particularly interesting because it opens up manifold possibilities of discovery, which will be described in more detail at the end of this chapter.
The process, which is mainly responsible for the production of axions according to equation 2.11, comes from the Primakoff effect. Here the axion couples to two photons (see figure 2.3) where one photon is placed by an electromagnetic field. This field can also be induced, for example, by the protons and electrons of a plasma.

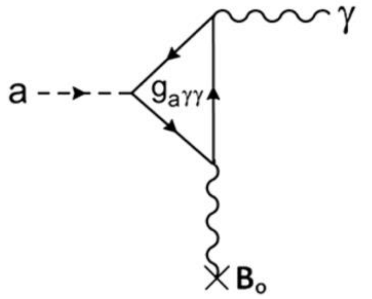

Figure 2.3.: Feynman diagram of the Primakoff effect. An axion decays via interaction with a magnetic field photon into a photon, also known as a 2 photon vertex (with coupling strength $g_{a\gamma\gamma}$). The inverse process is also possible (Stern, 2016).

Axion-like particle

If global symmetries are broken spontaneously, NG bosons are created. There are many examples of this, some of which originate from string theory. So the axion is only one NG boson of many proposed. But one thing is common to all of them, namely that they couple to photons. This results in the advantage that in experiments, in which axions are searched for, also other bosons can be found. To unlock the door to this, the dependence of f_a and m_a shown in equation 2.9 is broken, resulting in two free parameters: m_a and $g_{a\gamma}$ (the coupling to Photons).
In figure 2.7, at the end of this chapter, the parameter space which is thus spanned, together with some experimental constraints already found, is shown.
In the further course, for a better distinction, the ALP (or the ALP field strength) is denoted with a, while the axion is led with a_{QCD}. Furthermore, the coupling strength is abbreviated from now on with $g_{a\gamma}$.

2.2. Photon - ALP mixing

ALPs can couple to various particles of the Standard Model. In this work, only the interaction with photons is of interest. The following derivation follows in principle the approach of (Meyer, Horns, & Raue, 2013). The coupling of ALPs to photons is described by the Lagrangian

$$\mathcal{L}_{a\gamma} = \frac{1}{4} g_{a\gamma} \tilde{F}_{\mu\nu} F^{\mu\nu} a = g_{a\gamma} \mathbf{E} \cdot \mathbf{B} a \tag{2.12}$$

where $F^{\mu\nu}$ denotes the electromagnetic field tensor and $\tilde{F}_{\mu\nu}$ its dual. Furthermore a denotes the ALP field strength and $g_{a\gamma}$ the photon-ALP coupling strength (which has the dimension $[energy]^{-1}$).
The complete interaction between photons and ALPs is described by the Lagrangian

$$\mathcal{L} = \mathcal{L}_{a\gamma} + \mathcal{L}_{EH} + \mathcal{L}_a \tag{2.13}$$

with $\mathcal{L}_{a\gamma}$ specified in 2.12. $\mathcal{L}_{EH}$ is the effective Euler-Heisenberg Lagrangian which accounts for one-loop corrections in the photon propagator and ALP kinetic and mass terms are described by

$$\mathcal{L}_a = \frac{1}{2}\partial_\mu a \partial^\mu a - \frac{1}{2} m_a^2 a^2 \tag{2.14}$$

In order for ALPs to couple to photons, the presence of a magnetic field is required whose component $\mathbf{B}_\perp$ is transverse to the direction of propagation $\mathbf{k}$. Furthermore, the states of the photons' polarisation must lie in the plane spanned by $\mathbf{B}$ and $\mathbf{k}$. For a monochromatic polarized photon beam of energy E propagating along the x_3-axis in a homogeneous magnetic field in a cold plasma, $\mathcal{L}$ leads to an equation of motion which is similar in structure to the Schrödinger equation Raffelt1988a.

$$(i\frac{d}{dx_3} + E + \mathcal{M}_0) \begin{pmatrix} A_1(x_3) \\ A_2(x_3) \\ a(x_3) \end{pmatrix} = 0 \tag{2.15}$$

with $\mathcal{M}_0$ being the mixing matrix, $A_1(x_3)$, $A_2(x_3)$ describes the linear photon polarization amplitudes and $a(x_3$ stands for the strength of the ALP field.

$$\mathcal{M}_0 = \begin{pmatrix} \Delta_\perp & 0 & 0 \\ 0 & \Delta_\parallel & \Delta_{a\gamma} \\ 0 & \Delta_{a\gamma} & \Delta_a \end{pmatrix} \tag{2.16}$$

The individual terms of the mixing matrix are composed as follows:

$\mathcal{M}_0$ term	stands for	origin
$\Delta_\perp$	$\Delta_{pl} + 2\Delta_{QED}$	photon propagation in a plasma (Δ_{pl})
$\Delta_\parallel$	$\Delta_{pl} + \frac{7}{2}\Delta_{QED}$	and QED vacuum polarisation (Δ_{QED})
Δ_a	$-\frac{m_a^2}{2E}$	ALP kinetic term
$\Delta_{a\gamma}$	$\frac{g_{a\gamma}B}{2}$	off-diagonal elements determine photon-ALP mixing
Δ_{pl}	$-\frac{\omega_{pl}}{2E}$	plasma frequency $\omega_{pl} \approx 0.037\sqrt{n_{cm^{-3}}}\text{neV}$
Δ_{QED}	$\frac{\alpha E}{45\pi(B/B_{cr})^2}$	critical magnetic field $B_{cr} = \frac{m_e^2}{\lvert e \rvert} \approx 4.4 \times 10^{13}\text{G}$

Table 2.1.: Elements of the Mixing matrix $\mathcal{M}_0$ and their meaning

Equation 2.15 can be solved using the transfer function $\mathcal{T}(x_3, 0; E)$ with an initial condition $\mathcal{T}(0, 0; E) = 1$.
Neglecting the effect of QED vacuum birefringence, which is considered in Δ_{QED}, the critical energy at which photon ALP conversions become maximal and independent of energy E and ALP mass m is calculated from equation 2.17. In the range between this energy to a maximum energy given in equation 2.18 is the so-called strong mixing regime.

$$E_{crit} = \frac{\mid m_a^2 - \omega_{pl}^2 \mid}{2g_{a\gamma}B} \sim 2.5GeV \mid m_{neV}^2 - 1.4 \times 10^{-3} n_{cm^{-3}} \mid g_{11}^{-1} B_{\mu G}^{-1} \tag{2.17}$$

$$E_{max} = \frac{90\pi}{7\alpha} \frac{B_{cr}^2 g_{a\gamma}}{B} \sim 2.12 \times 10^6 GeV g_{11} B_{\mu G}^{-1} \tag{2.18}$$

Since the polarization of very high energy (VHE) photons cannot (yet) be measured, the polarized photon beam assumed so far from equation 2.15 must be replaced by an unpolarized one. For this purpose, a general polarization matrix in the form of a density matrix is introduced:

$$\rho(x_3) = \begin{pmatrix} A_1(x_3) \\ A_2(x_3) \\ a(x_3) \end{pmatrix} \otimes (A_1(x_3)\ A_2(x_3)\ a(x_3))^* \tag{2.19}$$

where $\otimes$ indicates that we are dealing with a tensor product.
By this reformulation, the equation of motion takes the form of a Neumann equation, which is given by

$$i\frac{d\rho}{dx_3} = [\rho, \mathcal{M}_0]\,. \tag{2.20}$$

This is solved by $\rho(x_3, E) = \mathcal{T}(x_3, 0; E)\rho(0)\mathcal{T}^\dagger(x_3, 0; E)$
For the case, relevant in the further course, that the photon beam runs through n regions in which in each case a constant homogeneous magnetic field with changing orientation and strength prevails, the transfer matrix is calculated from the product over all regions

$$\mathcal{T}(x_{3,n}, x_{3,0}; E) = \prod_{i=0}^{n-1} \mathcal{T}_i(x_{3,i+1}, x_{3,i}; E) \tag{2.21}$$

with a mixing matrix $\mathcal{M}_k$ for each region.
To obtain the expectation value of a system described by a density matrix, the corresponding trace must be calculated. Thus, the transition probability to find a photon / ALP beam in a final state ρ_{final} after it has traversed n regions results in

$$P_{final} = Tr(\rho_{final}\mathcal{T}(x_{3,n}, x_{3,0}; E)\rho(x_3, 0)\mathcal{T}^\dagger(x_{3,n}, x_{3,0}, 0; E)(2.22)$$

Since the ALP beam fraction cannot be measured, one calculates the photon survival probability of an originally unpolarized photon beam $\rho_0 = \frac{1}{2}diag(1, 1, 0)$, which is

$$P_{\gamma\gamma} = P_{11} + P22 = Tr((\rho_{11} + \rho_{22})\mathcal{T}\rho_0\mathcal{T}^\dagger), \tag{2.23}$$

where $\rho_{11} = diag(1, 0, 0)$ and $\rho_{22} = diag(0, 1, 0)$ and *diag* stands for a diagonal matrix which is a square matrix having entries different from zero only on the main diagonal where it is filled with the values of the *diag* expression.

2.3. Search for ALPs

Since the postulation of axions and axion-like particles, there are of course also attempts to find them experimentally. For the most part, the coupling to the 2 photon vertex and thus the coupling to the electromagnetic field is used. The conversion of photons to ALP in magnetic fields opens up a whole range of experiments, which have enormous differences in the size of their experimental setup. One of the most prominent experiments performed here on Earth in the laboratory are the "light shining through a wall" (LSW) experimental setups. An experiment with a "setup" of a good 8 light minutes is the Axion Helioscope, where solar axions and ALP shall be detected. The galactic or extragalactic search for traces of ALP reaches cosmological scales. Here we search the electromagnetic spectrum of the halo of our home galaxy or extremely bright astrophysical objects like supernovae or active galactic nuclei for signs of Photon ALP conversions. These three types of experiments will be briefly presented in the following.

"light shining through a wall"

The general setup of an LSW experiment consists of a strong light source such as a laser, which directs its light through a magnetic field onto an optical obstacle (the wall). ALPs, which are assumed to convert from some photons in this magnetic field, can penetrate this wall due to their extremely weak interaction with other particles. Behind the wall, another magnetic field is generated, in which some ALPs transform back into photons. These photons are then counted by a detector.

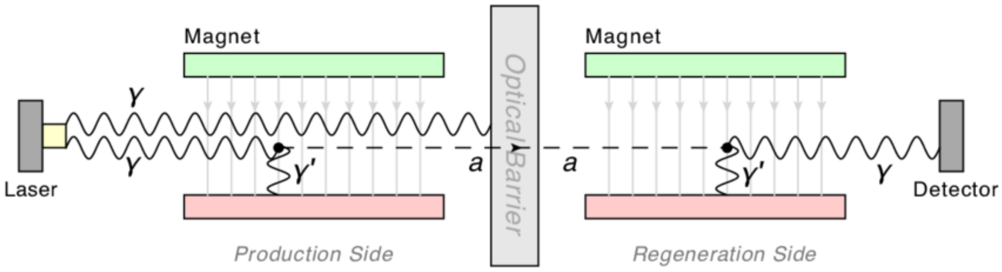

Figure 2.4.: Concept of light-shining-through-a-wall experiments (Battesti et al., 2018)

The number of photons N_γ arriving at the detector is proportional to the magnetic field strength B, the interaction length L between photon and magnetic field and the effective power $\mathcal{P}$ of the light source.

$$N_\gamma \propto (g_{a\gamma} B L)^4 \mathcal{P} \tag{2.24}$$

There is a proportionality with the fourth power for field strength and interaction length (2 powers for generation, 2 powers for reconversion). An example of a currently running LSW experiment is the "Any light particle 2" (ALP-2) project (Bähre et al., 2013). Considering the technical capabilities of the experiment with respect to the parameters given in equation

2.24, the expected amount of photons arriving at the detector can be estimated to be about one photon every 700000 years. This rough estimate gives an idea of the technical difficulties of a detection of ALPs. The challenge of this kind of experiments is to modify the parameters in a way that the number of detectable photons is pushed into a range that allows a detection within the lifetime of such an experiment. For this purpose, light sources of higher energy are used as well as stronger magnetic fields or resonators to increase the interaction length. Using resonators around one photon per day is expected in the experiment (for a coupling of 2×10^{-11} GeV^{-}1)

Axion helioscope

Already in the early 1980s the possibility was considered to experimentally detect the "invisible axion" in the emissions of astronomical objects like our Sun [Sikivie1983]. Thus, the hot stellar plasma, which has already been identified as a birthplace for the extremely light neutrinos, should also be an effective producer for axions or ALPs. In the electromagnetic field of the charged particles of the plasma, photons convert by Primakoff effect into ALPs, which leave it due to their extremely low interaction probability. The incoming flux of ALPs on Earth is guided by an experimental setup into a transverse magnetic field, in which they convert back into photons by the inverse Primakoff effect. According to the energy of their origin, the reconverted photons are also in the X-ray energy range. The corresponding experimental setup, which was already proposed by Pierre Sikivie in 1983, is called Axion Helioscope. One of the most famous experiments of this kind is the CERN Axion Solar Telescope (CAST, (Kuster et al., 2007)), which was put into operation in 2003.

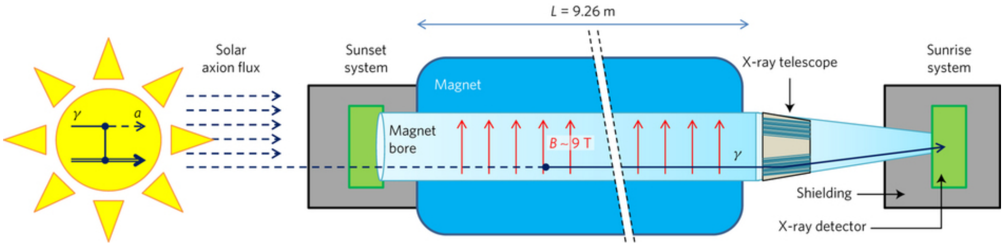

Figure 2.5.: Schematic representation of the CERN Axion Solar Telescope [(Anastassopoulos et al., 2017)]

The transverse magnetic field is generated by a superconducting dipole magnet with a maximum strength of 9.5T. The interaction length between magnetic field and ALP is 9.26m. To detect photons in the X-ray energy range, one of the four detector positions is equipped with an X-ray mirror optics of the Wolter type, which focuses them onto a CCD silicon detector. This setup closely resembles the design of X-ray telescopes in space which will be further described in chapter 3. The other detector positions are equipped with detectors which can register photons of other energy ranges. These can be produced by the reconversion of axions, which are either produced in other regions of the sun or which are not produced by the Primakoff effect (but for example by nuclear processes). The CAST experiment will be replaced in the near future by the International Axion Observatory (IAXO), a fourth generation Axion helioscope (Vogel et al., 2013). This will search for solar axions and ALPs with greatly improved sensitivity.

Large scale astrophysical ALP searches

If we do not only stay in the astrophysical neighborhood and look further out into space, we find celestial bodies which produce enormous amounts of electromagnetic radiation up to the TeV range. For example, ALP produced in core-collapse supernovae (SN1987A) are searched for (Lucente & Carenza, 2021). Also photon-ALP oscillations in the spectra of photons from comparatively close active galactic nuclei (AGN) such as the AGN of the central galaxy of the Perseus galaxy cluster NGC1275 (Berg et al., 2017), (Malyshev, Neronov, Semikoz, Santangelo, & Jochum, 2018) or, as in this work, the AGN of the central galaxy of the Virgo galaxy cluster, M87 are searched for (Marsh et al., 2017). Even very high distant AGN like quasars (Dominguez, Sanchez-Conde, & Prada, 2011) or BL Lacertae objects (Abramowski et al., 2013) are target of such searches. Due to the presence of astrophysical magnetic fields, which remain coherent on a large scale, such sources can become effective photon ALP converters. This work will focus on the conversion of very high energy (VHE) photons to ALP in galaxy clusters. Specifically, it will deal with gamma photons produced in the jet of the active galactic nucleus of the galaxy Messier 87. M87 is a giant elliptical galaxy in the center of the Virgo galaxy cluster and a strong source of radio and X-ray electromagnetic radiation. From the accretion disk of the central black hole of the AGN emerges vertically a highly collimated jet of matter which extends from near the core about 2pc. The electromagnetic emissions of this jet, which cover almost the entire spectrum, extend to at least 1500pc. Gamma photons produced close to the nucleus pass through extensive magnetic fields on their way to Earth, where a conversion to ALP can take place. Due to our very limited capabilities to characterize these magnetic fields precisely, we have to rely on indirect methods to build models of these fields. In irregularities of the received gamma spectra traces of photon ALP conversion can be searched for.

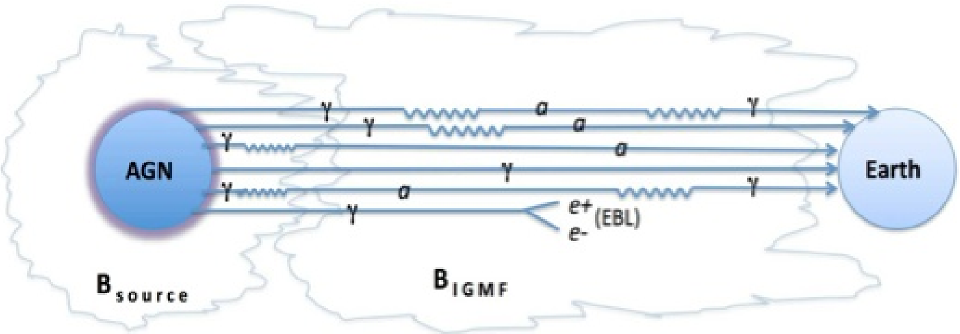

Figure 2.6.: Photon-ALP conversion from cosmic sources like active galactic nuclei (Sánchez-Conde et al., 2009)

Finally for this introductory chapter the ALP parameter space should be presented once descriptively. In figure 3 the ALP mass is plotted against the coupling strength. There, the areas in which previous and future experiments are sensitive are marked in color. For example, LSW experiments (red) such as ALPS-1 or ALPS-2 tend to be sensitive in the region of higher coupling strengths ($g_{a\gamma} \sim 10^{-7}\text{GeV}^{-1}$ for ALPS-1 and up to $g_{a\gamma} \sim 10^{-10}\text{GeV}^{-1}$ for ALPS-2), while searches of solar ALPs in CAST (dark red) or IAXO (transparent blue) are sensitive in regions of smaller coupling strength ($g_{a\gamma} \sim 10^{-10}\text{GeV}^{-1}$ for CAST and $g_{a\gamma} \sim 10^{-11}\text{GeV}^{-1}$ for IAXO). In a similar range of ALP couplings like IAXO and small ALP masses ($10^{-9}\text{eV} < m_a < 10^{-7}\text{eV}$), the search for traces of photon - ALP conversion of galactic and intergalactic photon sources takes place (green). Observations of the Perseus galaxy cluster are found in this region, as well as searches for ALP in observations of supernovae. The H.E.S.S. telescope, which is described in more detail in the next chapter and from which the observations studied in this thesis were made, and the Fermi gamma-ray satellite are also sensitive in this region. The allowed range for the original axions, for which there is a tight relation between mass and coupling already described, is shown in orange. The abbreviations KSVZ and DFSZ refer to established axion models. Research is also being carried out with the aim of extending this close relation (Farina, Pappadopulo, Rompineve, & Tesi, 2017).

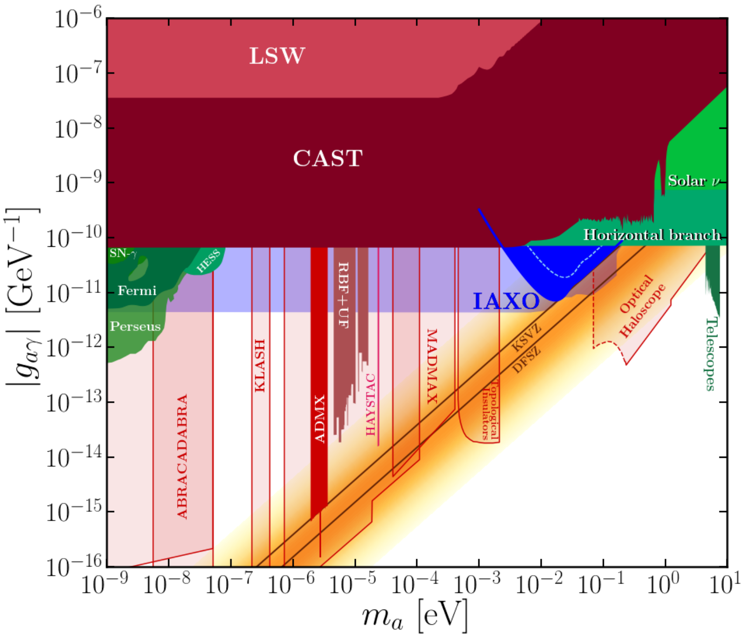

Figure 2.7.: ALP parameter space with plotted limit values, which were found in various experiments (Dafni et al., 2019)

3. M87 and the Virgo cluster

In this work, the search for ALP is performed on a large astrophysical scale. The object of interest is the Virgo galaxy cluster. The light source is the active galactic nucleus of the central galaxy M87 and the magnetic field is the Virgo intracluster magnetic field. Although Virgo is a relatively close galaxy cluster by comparison, its enormous distance presents us with enormous challenges. Neither the exact properties of the light source or the magnetic field are known, nor the exact distance of this galaxy cluster. All these questions depend on observations of the electromagnetic spectrum of this astronomical object. Since even with the knowledge gained from these observations it is far from being possible to create an exact picture, models must be created to determine the properties of the Virgocluster and the galaxy M87 as well as possible. This chapter is devoted in the first section to the introduction of the Virgo galaxy cluster, its central galaxy M87, and to the determination of its distance. In the second section, the observation of the electromagnetic spectrum we receive from Virgo and M87 is discussed, and the techniques and equipment needed to do this are explained. The last chapter describes which models have to be built for the further procedure and how the made observations can be used for it.

3.1. Characteristics and morphology

3.1.1. The Virgo galaxy cluster

The Virgo Cluster is the closest galaxy cluster to us and part of the Virgo Supercluster, which also includes the local group that contains our Milky Way (figure 3.1 on the left side). Due to its proximity and brightness, the Virgo galaxy cluster is the object of numerous studies in different regions of the electromagnetic spectrum. Around 2000 galaxies (Binggeli, Sandage, & Tammann, 1985) are estimated to belong to this galaxy cluster. The first astronomical mention of the Virgo galaxy cluster comes from Charles Messier's "Catalogue des Nébuleuses des amas d'Étoiles" published in 1781. Today this first mentioned object is known as Messier 49 and is part of the Messier catalog, which includes 109 bright astronomical objects such as galaxies, star clusters, and nebulae. Messier observed an unusually high concentration of bright objects in this region of space and indeed 15 of the 109 "Messier objects" are located in the Virgo cluster (for example figure 3.1 on the right side). The absolute distance of the Virgo cluster is still not clarified and subject of scientific research. Distances of 15 to 22 Mpc are quoted. One possibility is to base the determination of the distance of the cluster exclusively on its dominant galaxy M87.

As a rich galaxy cluster (Mei et al., 2007), Virgo not only contains many member galaxies but also has a nearly spherical shape with the most massive galaxies in the center. Fur-

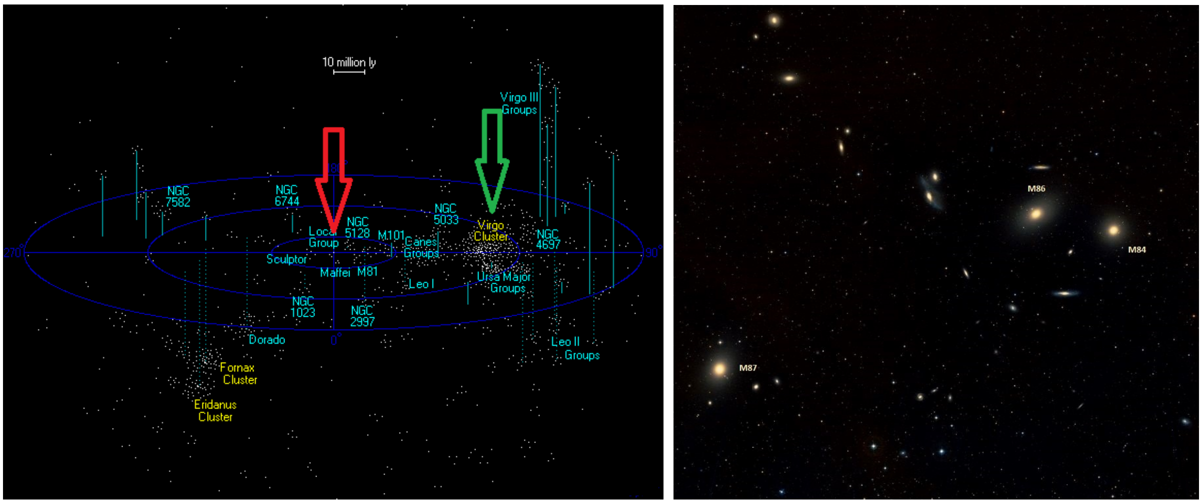

Figure 3.1.: The left image (open source) shows a map of the Virgo Supercluster centered on the Local Group, where our galaxy is located. The Virgo Cluster is visible in the center right. The right image (taken from messier-objects.com) shows a section of the Virgo galaxy cluster

thermore, it is rich in gas, dust, and nebulae. The Virgo cluster is a collection of at least 3 subclusters concentrated around M87, M86 and M49. The motions of the surrounding dwarf galaxies and the structure of the X-ray emitting gas in which they are embedded suggest that the subclusters M87 and M86 are in the process of merging (Binggeli, 1999). Together they are also called "Cluster A". The subcluster around M49 is called "cluster B" according to this nomenclature and a possible subcluster around M60 is called "cluster C". Although it is not exactly in the center, it seems to have an enormous influence on the morphology of the whole cluster. Thus, there are two cluster-internal "main matter axes" along which the subclusters are oriented, one in north-south direction and one in east-northwest direction, where the first axis aligns almost perfectly with the outer isophotes of M87 and the second axis aligns perfectly with the jet axis of M87. Isophotes are lines of equal brightness and can be described quite accurately by concentric ellipses. Elliptical galaxies are divided into classes E0 (circular) to E7 (highly oblate) according to the shape of these ellipses (Schneider, 2008). The Virgo cluster is permeated with a hot thin plasma with a highly complex structure, which has a high gas density near the galaxy M87. This so-called intracluster medium (ICM) also contains a large amount of intergalactic stars and planetary nebulae. Since the plasma emits electromagnetic radiation in the X-ray range, its structure can be studied with X-ray telescopes. For a more precise description of the ICM, non-thermal processes must also be considered. Observations in the radio wave range reveal such processes. They arise, for example, from synchrotron radiation, which results from the acceleration of relativistic charged particles in a magnetic field. For synchrotron radiation to occur in such an environment, a population of GeV-electrons and a cluster magnetic field strength in the μG range is required (Murgia et al., 2004).

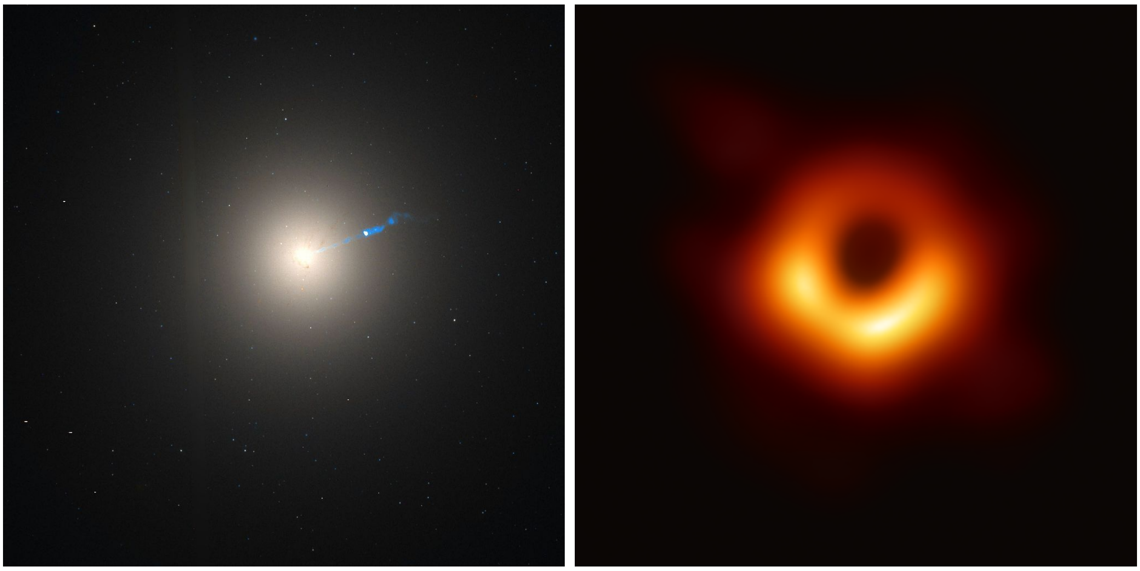

Figure 3.2.: The left image (NASA and The Hubble Heritage Team) shows black hole-powered jet of electrons and sub-atomic particles streaming from the center of M87, whereas the right image shows the first image of a supermassive black hole, the central black hole of M87.

3.1.2. M87

The galaxy M87, which is of central importance in this work, was discovered in 1781. M87 is a galaxy close to the center of the Virgo galaxy cluster, whose AGN M87* is a supermassive black hole estimated to be more than 6×10^9 solar masses (Walsh, Barth, Ho, & Sarzi, 2013). It is one of the most massive black holes discovered to date, and in 2019 became the first astronomical object of this magnitude to be "photographed" from data collected by the "Event Horizon Telescope Collaboration" (Collaboration, 2019)(right image of figure 3.2].

A strongly collimated relativistic matter jet emanates from this AGN, extending about 1.5 kpc. This jet is an intense outflow of magnetized relativistic plasma from the active Galactic core of M87, acting as a cosmic particle accelerator. How exactly the acceleration mechanism of these jets works is not known until today. The accelerated electrons and positrons emit electromagnetic radiation from the radio wave to the TeV gamma ray range via synchrotron radiation and inverse Compton processes. Observations of the jet suggest that its energy consists mainly of electromagnetic radiation at distances above about 10pc (Alves, Zrake, & Fiuza, 2018). Thus, the path of gamma photons detected by H.E.S.S. can be assumed to have started some parsecs away from the central black hole.

3.1.3. Distance measurement

In astronomy, distances are usually given in parallax seconds (parsecs). The reference value for a parsec is the astronomical unit (AU), i.e. the mean distance of the earth to the sun. A parsec is then the distance from which 1AU would be seen at an angle of one arcsecond. This corresponds to 3.26 light years. For nearby stars we are in the "normal" parsec range, but within our galaxy we calculate in the kiloparsec range (kpc). Distances to other galaxies or galaxy clusters, however, are given in megaparsecs (Mpc). The limit of the observable universe is about 14 gigaparsecs (Gpc). For distances in our solar system or to closer stars, several hundred light years, trigonometric parallax can be used. To get the largest possible basis for determining the parallax angle, stars whose distance is to be determined are measured at intervals of half a year. Thus the size of the base is 2AU. Due to the decreasing parallax angle, the errors of this measurement exceed a critical level at large distances, so that another method must be resorted to. Here the spectroscopic parallax comes into play, for which the absolute and apparent brightness of an astronomical object are brought into relation. The apparent brightness corresponds to the brightness perceivable on Earth. The absolute brightness on the other hand is the actual brightness of an astronomical object. To determine this absolute brightness, the period-luminosity relation of radially pulsating stars can be used or, more inaccurately, it can be derived from the Hertzsprung-Russell diagram. In the first case, the absolute magnitude is calculated from the mean pulsation period using $M_{mean} = k\ log_{10}(\frac{P}{d}) + q$, where P is the pulsation period in days d. The values for k and q depend on the spectra of the pulsation. The Hertzsprung-Russell diagram, on the other hand, shows the rough evolutionary distribution of stars, with the absolute magnitude of a star plotted against its spectral type. Astronomical objects whose absolute brightness can be determined particularly well are called standard candles. Once the absolute magnitude is determined the distance can be calculated by Distance modulus $\mu = 5\ log_{10}(d) - 5$, where $\mu = M - m$ is the difference between absolute and apparent magnitude. If one wants to calculate the distance of other galaxies one looks for standard candles, which are within these galaxies. To create an adequate model for the Virgo Cluster, the distances of the galaxies M87 and M84 as well as the distance of both galaxies to each other are needed.

3.2. Electromagnetic spectrum

3.2.1. Radio observations

In the following, the regions of the electromagnetic spectrum of interest for this work and the methods for observing them will be presented. The beginning is made by radio waves, which fall into the field of radio astronomy. Radio astronomy has a history of almost 100 years and exists in principle since the first discovery of radio waves from our Milky Way in 1932 by Karl Jansky. Due to the impermeability of our atmosphere for radio waves with a frequency below 10MHz (reflection by the ionosphere) and above 100GHz (absorption by atmospheric water vapor) the window for receivable radio waves is limited. Due to the sometimes extreme distances of astronomical objects, the intensity of the received radio waves is very low. For this reason, radio telescopes either need large antennas for bundling or have to be connected to an interferometer to increase the effective antenna area. One such telescope is the Very Large Array (VLA) telescope.

The facility is located on the San Agustin plain in New Mexico (USA). The 27 individual radio telescopes are mounted in a y-shape (each with a 120° angle) on rails on which they can be moved. At its maximum extent, the effective area of the antenna is equivalent to that of a single 36km telescope. The VLA receives radio waves from 4m to 7mm wavelength. Electromagnetic radiation in this range is emitted by a variety of astronomical objects. These radio sources include our Sun, supernova remnants and pulsars, interstellar gases, radio galaxies (i.e., active galaxies that radiate very brightly in the radio range), and many more. One object well studied by the VLA telescope is the galaxy M87. The resulting observations are the basis for analyzing the strength and structure of the magnetic field that permeates the Virgo Cluster. This will be discussed in more detail in the last section of this chapter.

Figure 3.3.: Aerial view of the central area of the 27 individual radio telescopes of the Very Large Array (made by Dave Finley, courtesy National Radio Astronomy Observatory and Associated Universities, Inc.)

3.2.2. X-ray observations

With wavelengths from 12nm to about 2.5pm, X-rays are much more energetic than radio waves. Since the Earth's atmosphere is opaque to this region of the electromagnetic spectrum, X-ray astronomy relies on satellite-based telescopes. A peculiarity of X-ray optics makes this area of astronomy a major technical challenge: Since X-rays are absorbed or transmitted by most materials when they strike at approximately right angles, special X-ray mirrors must be used in which the angle to the reflection plane is very small (typically 10 arcminutes to 2 degrees). A combination of a paraboloid and a hyperboloid mirror system of this type is used in so-called Wolter telescopes. These focus the X-ray photons onto the detector used in the respective telescope. In this work, data from two X-ray satellites, the ROSAT X-ray satellite launched in 1990 and the Chandra X-ray Observatory launched in 1999, are used. The former uses a position-sensitive proportional counter tube to detect the X-ray photons, achieving an angular resolution of slightly less than 5 arcseconds. ROSAT is

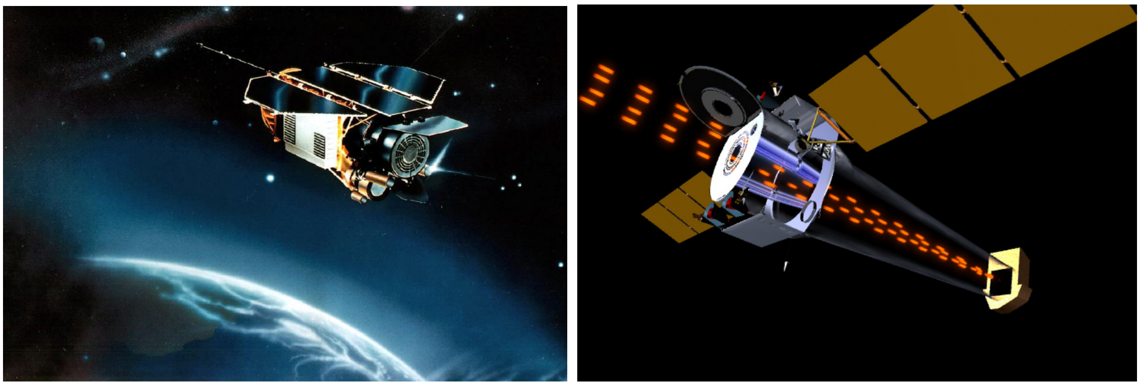

Figure 3.4.: The left image shows an artist's rendering of the ROSAT X-ray observatory (DARA, NASA).The right image shows the light path of the Chandra X-ray space observatory. Incoming X-ray photons are reflected at the grazing angle and focused on a detector to produce an image of the cosmic source (*chandra.harvard.edu/resources/chandraMission.html*)

sensitive to photons with energies from 0.1 - 2keV. Chandra uses an Advanced CCD Imaging Spectrometer (ACIS) as a detector, where CCD stands for charge-coupled device. The operation of the CCD sensors, 10 of which are built into the ACIS, is based on the internal photoelectric effect. With this setup, Chandra achieves a resolution of 0.5 arcseconds and operates in an energy range of 0.2 - 10keV. The object of observation of these satellites are astrophysical X-ray sources like our Sun, supernova remnants, galaxy clusters (in particular hot gas passing through these clusters), active galactic nuclei and many more. In this work, the object of interest is the cluster-internal hot gas of the Virgo cluster starting from its center, the galaxy M87.

3.2.3. Gamma-ray observations

Gamma astronomy is dedicated to the observation of cosmic phenomena in the highest energy ranges of electromagnetic radiation. The energy range of gamma photons is $E_\gamma > 500$keV and testifies to astronomical processes where enormous amounts of energy are released. Examples for such processes are gamma-ray bursts from supernova explosions or shock waves from ejected gas shells as well as active galactic nuclei. The mechanisms by which gamma rays are released include electron positron annihilation or the inverse Compton effect. However, the telescopes described so far are not sensitive in this region of the electromagnetic spectrum. In addition, gamma radiation, like X-rays, is absorbed by the Earth's atmosphere. Therefore, corresponding telescopes must either operate satellite-based or, in the Earth-bound case, rely on indirect measurement. Satellite-based gamma-ray telescopes mainly use scintillation detectors with attached photomultipliers for detection. The primary instrument of the Gamma-ray Space Telescope, the Large Area Telescope (Fermi LAT), uses pair conversion to detect gamma photons. Gamma photons collide with a layer of tungsten to create

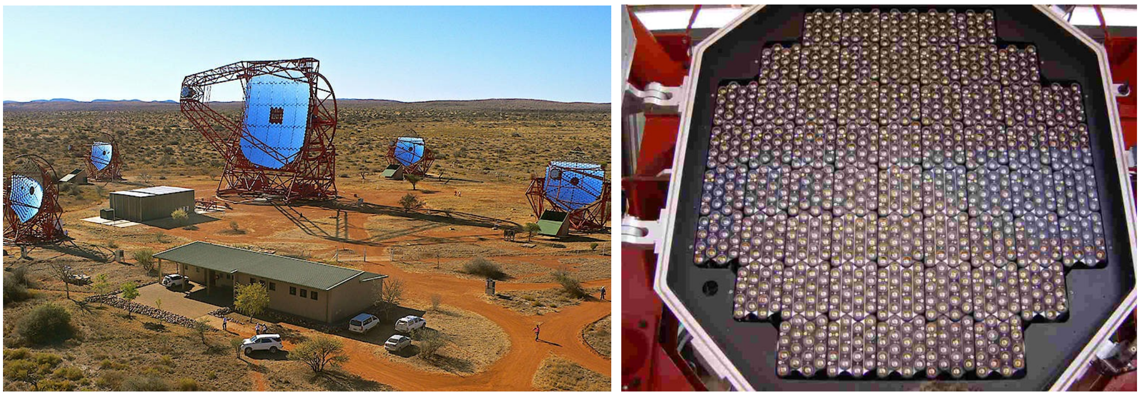

Figure 3.5.: The left image shows the H.E.S.S. facility installed in Namibia in its phase 2, whereas the right image shows the camera system of the telescopes in top view. The individual pixels can be recognized very well here.

an electron-positron pair. Using precision scintillation detectors, these particle showers are analyzed with respect to the energy and direction of the original gamma photon. The Fermi LAT is sensitive in an energy range from 20MeV to about 300GeV. In this work, however, Earth-based detectors for cosmic gamma rays are of interest. Compared to satellite-based telescopes, these have a considerably larger detector area and use the Earth's atmosphere as detector medium.

High Energy Stereoscopic System

In particular, the High Energy Stereoscopic System, or H.E.S.S., will be discussed here, with all information and images taken from the public H.E.S.S. pages of the Max Planck Institute for Nuclear Physics Heidelberg (*www.mpi-hd.mpg.de/hfm/HESS/*). Observations of gamma photons produced at the center of M87 will be examined for evidence of photon ALP conversions. H.E.S.S. is a so-called Imaging Air Cherenkov Telescope (IACT) and covers an energy range from 30GeV to a few 10 TeV. Located in Namibia near the Gamsberg mountain, the Cherenkov Telescope is actually a system of 5 telescopes (as shown in Figure 3.5, left). Its location was chosen because of the optimal optical properties of this area. Namibia, along with Chile, is one of the top five global locations for astronomical observations. The special design allows it to increase the effective detection area or lower the energy threshold. In 2004, 4 telescopes were initially built, each about 12m in diameter, arranged in a square of 120m side length. This arrangement is called H.E.S.S Phase 1. In 2012, a fifth telescope, built at the intersection of the diagonals of the first four telescopes, was added to this system. This telescope has a diameter of 28m. Together, the 5 telescopes form H.E.S.S Phase 2. A further planned expansion was abandoned for financial reasons. The telescopes of phase 1 consist of 382 round mirror facets of 60cm each, the fifth telescope has 875 hexagonal mirror facets of 90cm diameter each. In the following, the operation of a Cherenkov telescope will be briefly outlined.

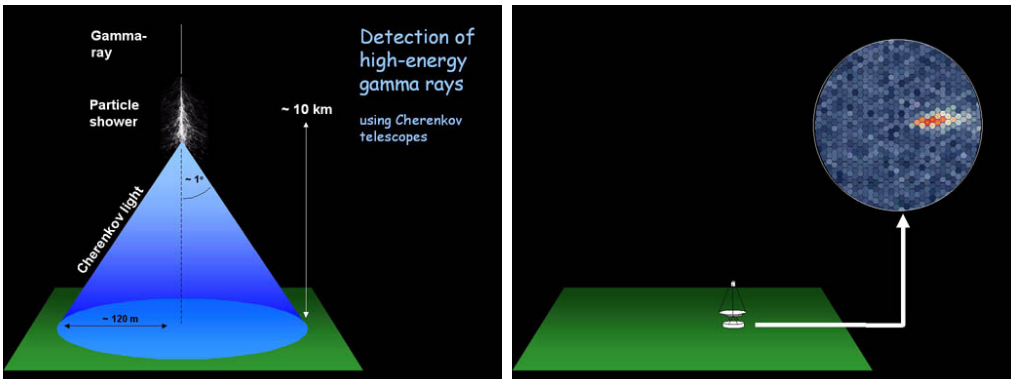

Figure 3.6.: The left image shows the formation of the Cherenkov light cone which is triggered by incident high energy photons in the atmosphere and the associated shower formation. The right figure shows the image of one of the telescope cameras after an incident Cherenkov photon was recorded.

Imaging air Cherenkov technique

The detection of gamma photons in the TeV range is done using the imaging air Cherenkov technique. When high-energy photons hit the upper atmosphere, showers of secondary particles are generated. This occurs through pair generation when gamma photons interact with matter in the Earth's atmosphere. The electrons and positrons resulting from this pair production react again with other particles of the atmosphere or emit photons via bremsstrahlung. The resulting particle cascade consists predominantly of electrons, positrons and photons. These particles travel at close to the speed of light, which is why they emit Cherenkov radiation. This bluish radiation is produced when charged particles move at a speed greater than the speed of light in the medium through which they are traveling.

The charged particles of the air shower emit Cherenkov radiation in a narrow cone starting from the trajectory of the original gamma photon, striking the ground in an area of about 120m radius (see Figure 3.6 on the left), with about 100 Cherenkov photons arriving at intervals of a few nanoseconds. To detect enough of these incoming photons, a Cherenkov telescope requires an effective area of about 50000m^2 (compared to the area of less than 1m^2 of satellite-bound gamma-ray detectors). When a photon of the Cherenkov light cone falls on one of the H.E.S.S. telescopes, it is reflected by mirrors of the collecting surface to the camera (which can be seen on the right side in Figure 3.5), which has 960 or 2048 photodetector elements ("pixels") with attached photomultiplier tubes. By combining the images (like the exemplary one shown in Figure 3.6 on the right) from all H.E.S.S. telescopes, it is possible to reconstruct the track of the particle shower and thus the original particle.

The intensity of the images allows to determine the energy of the original gamma photon. In order to identify which measured signals really originate from the targeted object, images must also be taken that serve to exclude background signals. For this purpose, in the case of the "wobble observation mode", the focus of the telescope can be moved slightly away from the targeted area (±0.5° source offset in the field of view). It is also possible to select several background regions around the targeted area, which allows the creation of a background map. The resulting data set of observations of gamma rays coming from M87 is presented again separately in Chapter 5.

3.3. Modeling the Virgo Cluster

3.3.1. The electron density

In this chapter, 3 different regions of the electromagnetic spectrum and the methods used to detect them were highlighted. While the data of the H.E.S.S. telescope will be examined for signs of photon - ALP conversion, the data and findings from the measurements of radio waves and X-rays are needed to better understand the place where this conversion takes place. The galaxies of a galaxy cluster are embedded in a hot X-ray emitting gas. And although this gas, which consists mainly of hydrogen and helium in the ionized state, has an extremely low density (on the order of 10^{-3} particles per cubic centimeter), it represents about 10% of the total mass of a galaxy cluster. The density of this intracluster medium (ICM) increases sharply towards the center of the cluster. The temperature of the ICM is between 10 and 100 megakelvin, which is responsible for the fact that the ICM is in the state of a plasma, in which the gas is a particle mixture of ions and free electrons. The high temperatures are due to gravitational energy released during the formation of the cluster. Due to the high density of the gas in the center region, especially large amounts of X-rays are emitted there, which is why a cooling of the gas would actually be expected. However, the jet driven by the accretion onto the supermassive black hole in the center of M87 heats up the gas again. The intensity of the emitted X-rays is proportional to the gas density. The X-ray satellites measure the X-ray spectrum of the ICM and can image the X-ray brightness. From the surface brightness profile thus obtained, the gas density can be determined. Based on the state of the gas, it is thus also possible to infer the electron density, which is required for the following reasons:

1. Determination of the strength of the intracluster magnetic field (Formula 4.9), which is modeled in chapter 4.2.
2. Calculation of the rotation measure (Formula 4.14), with which the magnetic field model parameters are constrained.
3. Determination of the critical energy at which the probability of photon ALP conversion becomes maximum (Formula 2.17).

3.3.2. The intra cluster magnetic field

Ultimately crucial for the conversion of gamma photons into ALP is the magnetic field through which the photons fly on their way from their point of origin at the jet of the central black hole to Earth. In this respect, a large part of the efforts of both current and past research, but also of this work, is devoted to determining this field as precisely as possible. The two most important factors for a transformation to occur at all are both the magnetic field strength and the coherence length. For this reason, in the following for the interaction between photons and magnetic field only the contribution of the Virgo intracluster magnetic field and the galactic magnetic field of our Milky Way. The magnetic field of Galaxy M87 which hosts the jet-producing AGN as well as the intergalactic magnetic field are not considered. The reason for their exclusion is a too low coherence length in the host galaxy and a too low magnetic field strength in the IGMF.

4. Modeling photon - ALP oscillations in Virgo

In this chapter, radio and X-ray spectrum observations are used to build models of the intracluster medium as well as the intracluster magnetic field. Here, essentially the approach of the work of (Marsh et al., 2017) is reproduced and the results compared to their findings. In the first section, a model of the electron density of the ICM is constructed using data from two X-ray satellites. In the second section, the model of the ICMF is constructed. The parameters of the model are constrained using the rotational measure calculated from the Faraday rotation of radio waves. In the last section, the created models are used to calculate the photon survival probability assuming photon-ALP conversion. This is done for some combinations of ALP mass and coupling strength. The Python package GammaALPs (Meyer, Davies, & Kuhlmann, 2021) was used to calculate the magnetic field model, the rotation measure and the photon survival probability. The code written for this can be found in Appendix B.

4.1. Modeling the Virgo Cluster electron density

Preparation of the X-ray data

In chapter 3.3 it was shown that the observations of the X-Ray satellites differ strongly with respect to resolution. While Chandra took very detailed, high-resolution images of the central region of M87, the ROSAT images are rather poor in detail, but go further out into the outer regions.

Therefore it makes sense to combine the data of both satellites to get a complete picture of the electron density of the Virgo Cluster. The Chandra data mentioned in (Russell, Fabian, McNamara, & Broderick, 2015) were kindly provided by Helen Russel and are listed in Appendix C. The data from the ROSAT X-ray satellite used in this work (Nulsen & Bohringer, 1995) was collected in the second half of 1992 during an observation of the Virgo Cluster aimed at M87 using a Position Sensitive Proportional Counter (PSPC). The total duration of the measurement was 30452s and about 1.8×10^6 photons were detected. The field of view of the PSPC was divided into 38 rings, with some more compact background sources and distortions removed. This is important because the Virgo Cluster is assumed to be approximately spherical [Forman et al.,1982] with moderate variations having no significant effect on the results [White et al.,1994]. Due to the spherical symmetry, the electron density of the intracluster plasma can be determined from the surface brightness profile using an iterative approach. First, the X-ray emission per unit volume is determined for one shell.

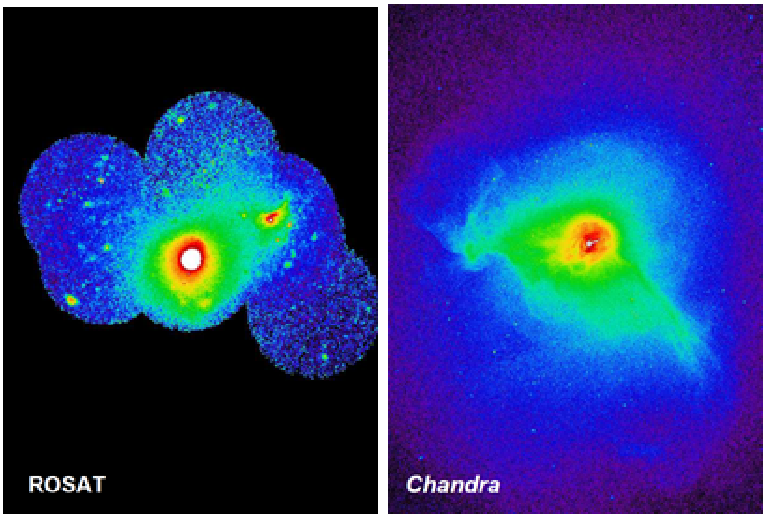

Figure 4.1.: X-ray images of the centre of the Virgo cluster: left ROSAT (left), Chandra (right). The increasing resolution has shows a complex structure in the hot gas (Guidetti, 2011)

Thus, the contribution of this shell to the emission of all included rings is known and can be removed. By the time one arrives at a particular ring with this procedure, the contributions of all outer shells have already been removed. The authors started at the outer rim, with ring 38 being omitted due to problems with theyr fitted surface brightness model. The outer limits of the rings are given in the angular size arcmin and must first be converted to the linear size of kpc to obtain the radii of the corresponding shells. This is done by means of the formula

$$r = aD_c(a) \times \theta \tag{4.1}$$

where $D_c(a)$ is the comoving distance between two points, r the radius we are looking for and θ the given angle in arcseconds.
The comoving distance is calculated using

$$D_c = c\int_a^1 \frac{1}{a * \dot{a}} da, \tag{4.2}$$

where the scaling factor a depends on the redshift z by

$$a = \frac{1}{1+z} \tag{4.3}$$

and

$$\dot{a} = H_0\sqrt{\frac{\Omega_R}{a^2} + \frac{\Omega_M}{a} + \Omega_K + \Omega_A a^2}. \tag{4.4}$$

H_0 is the Hubble constant and Ω_R, Ω_M, Ω_K and Ω_A stand for different energy densities of the universe. The cosmological model Planck2018 was used for these parameters (Aghanim et al., 2020). The calculations were carried out with the help of the program *arc2parc* (designed by Álvaro Bernis, María Bernis and Jose Oñorbe). All calculated radii as well as the corresponding electron densities are listed in Appendix A.
Figure 4.2 shows the electron density as a function of distance from the central AGN of M87.

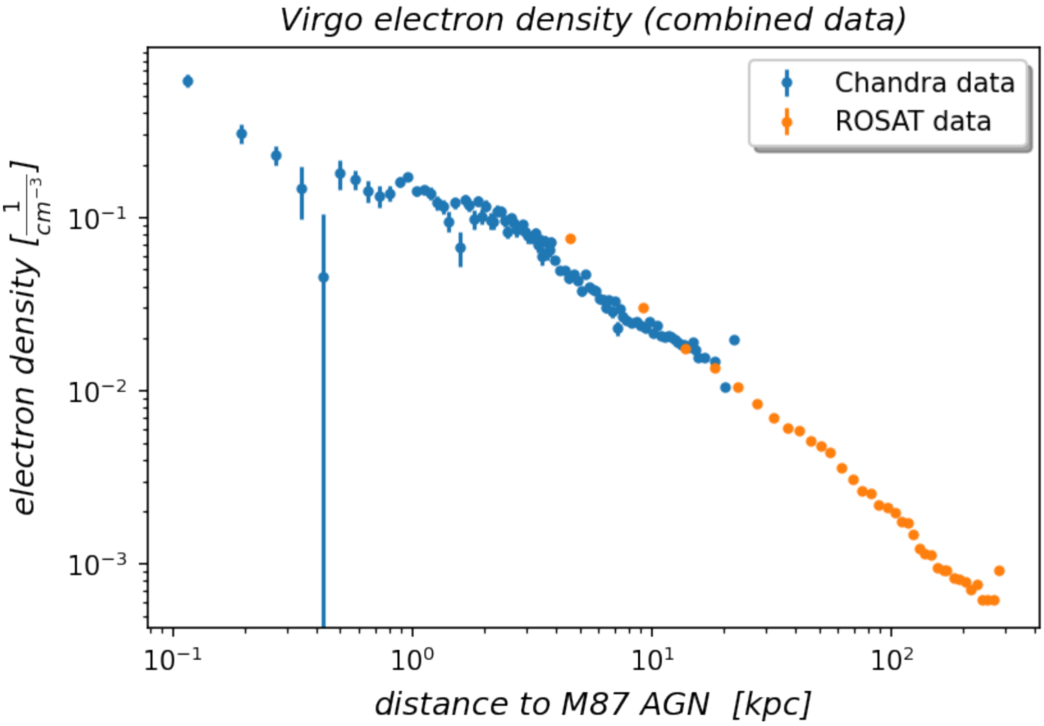

Figure 4.2.: Combined data points from the Chandra and ROSAT X-ray satellites

Fitting the electron density model

The task that now follows is to find a suitable fit for the combined values of the electron density. In an attempt to model the electron density of the Perseus cluster (Churazov, Forman, Jones, & Böhringer, 2003), an analytical approximation function was used to describe the radial behavior of the intracluster medium.

$$n_e(r) = \frac{n_0}{[1 + (\frac{r}{r_{core}})^2]^{\beta}} + \frac{n_2}{[1 + (\frac{r}{r_{core2}})^2]^{\beta_2}} \tag{4.5}$$

This generic "double beta" function contains the normalization parameters n_0 and n_2 but also r_{core}, r_{core2}, β and β_2 - parameters which relate the electron density to the size ratio of the considered galaxy cluster and thus to the radial dependence of the gas density.

Here, the second term describes the electron density at higher distances and was taken from [Jones1999]. This function will also be used in this work to model the electron density of the Virgo galaxy cluster. In particular, the special characteristics of the inner region are to be taken into account. To perform the fitting of the "double beta" function to the data points and their errors, the Python based ecosystem *Scipy* was used. Here the methods *leastsq*, *curvefit* as well as *minimize* of the *Scipy.Optimize* package as well as the method *UnivariateSpline* of the package *Scipy.Interpolate* were used. The obtained results were then compared with respect to their physical statement as well as the goodness of fit. To determine the goodness of fit, the reduced chi-squared statistic was used. This is defined as chi-square per degree of freedom:

$$\chi^2_\nu = \frac{\chi^2}{\nu} \tag{4.6}$$

where $\nu = n - m$ whith n denoting the number of data points and m the number of fit parameter. Values for χ^2_ν can be (significantly) greater than, less than, or approximately (equal to) one. In the former case, the model does not capture all the data (or is just generally poorly fitted) in the latter, it is overfitted. Is $\chi^2_\nu \approx 1$ one may expect that the extent of the match between observations and estimates is in accord with the error variance. The expected shape of the fitted curve provides for a strong increase of the electron density in the inner region, whereas it does not increase further after a certain distance when approaching the gamma ray source further. This is important because we do not start our observation directly at the black hole but some 1pc away, where the AGN jet produces the gamma photons. In the outer regions, a continuous decrease of the electron density is expected, which is shown as a straight line in the double logarithmic plot. The latter is in this respect consistent with the results of previous work. Fitting the function turned out to be extremely difficult, since the 6 fitting parameters are strongly correlated. Moreover, in order to achieve a satisfactory fit at all, some values had to be excluded. The data points describing the electron density with the highest and the smallest distance of the ROSAT measurement were already described as problematic in the corresponding work. The same applies to the outermost data point of the Chandra image, which was removed together with the data point at 0.4 kpc. The latter made any attempt to model the inner region futile due to its extremely high error margin. All discarded values are listed in Table 4.1.

r (kpc)	n_{el} $(cm^{-3)})$	dataset (satellite)
0.42	0.045185	Chandra
4.58	0.0763	ROSAT
22.08	0.019866	Chandra
282.69	0.000919	ROSAT

Table 4.1.: omitted electron density data points

The best result was obtained with the *minimize* method. This method uses the Nelder-Mead Simplex Algorithm, which is explained in more detail in Appendix B. The expected shape of the electron density curve described above is achieved with a goodness of fit of $\chi^2_\nu \approx 1.1$ and is shown in Figure 4.3. The best fit parameters are listed in Table 4.2.

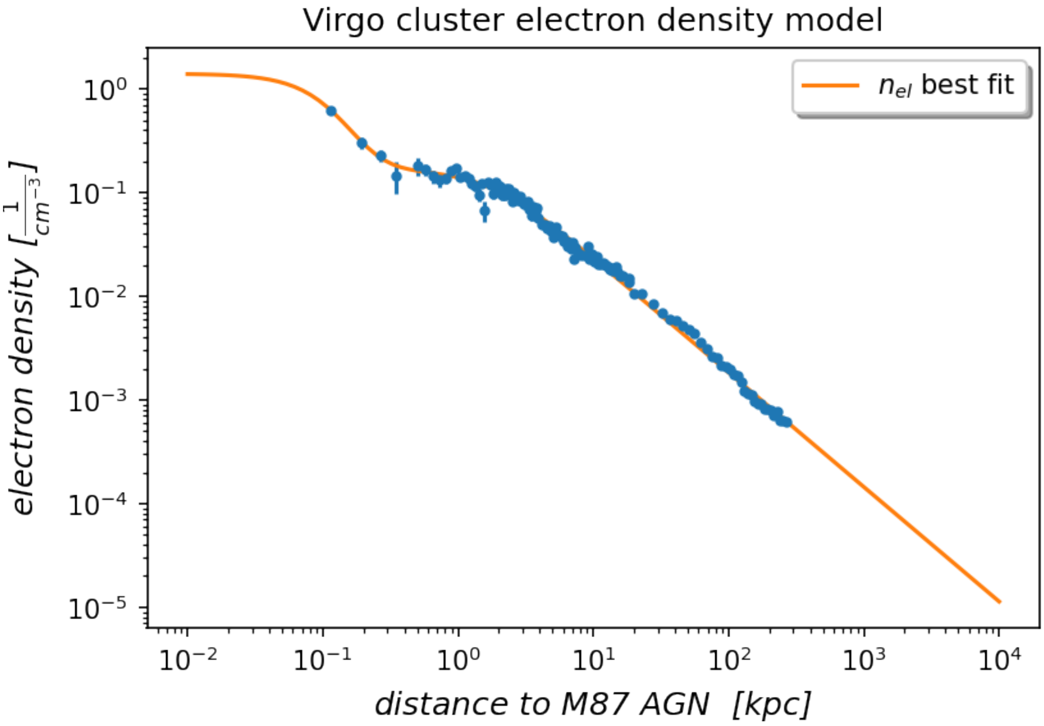

Figure 4.3.: electron density data points with best fitted double beta function plotted.

4.2. Modeling the Virgo intra cluster magnetic field

Development of the magnetic field model

In order to build the intracluster magnetic field model, it is first necessary to clarify how the magnetic field environment is structured in the observed region. In the simplest case this would be a homogeneous magnetic field, as it is applied for example in some LFW experiments. Certainly, this simplest of all situations is not realistic in the complex and highly turbulent intracluster magnetic field, especially in the vicinity of the M87 AGN jet. Since the jet is not directly aligned in the line of sight to Earth, but is inclined at an angle of some 22° [Biretta, 1995], even a jet-specific magnetic field model (such as a simple toroidal or a spiral tangled one) is inappropriate for our purpose. Investigations of M87 using measured Faraday rotation motivate assuming a turbulent magnetic field environment [Guidetti]. The strength of the magnetic field depends on the electron density of the intracluster medium[Feretti 2012] and is estimated by (Ajello et al., 2016) to be

$$B(r) = B_0 \left(\frac{n_e(r)}{n_e(r=0)} \right)^{\eta} \tag{4.7}$$

where B_0 indicates the central magnetic field strength and η determines the decrease of the field relative to the electron density of the intracluster medium. The magnetic field is now modeled along the line of sight, assuming that it extends radially from the cluster center. Further it is assumed that the field consists of N domains in which it is constant:

$$\vec{B}(r) = \sum_{i=0}^{N} (\vec{B})_i(r) \tag{4.8}$$

In each domain, the orientation of the field is described by an isotropically distributed unit vector $(\vec{b})_i$. Together with 4.7, the following model function for the intracluster magnetic field is obtained [Marsh2017]:

$$(\vec{B})_i = B_0 (\frac{n_e(r)}{n_e(r=0)})^{\eta} (\vec{b})_i \tag{4.9}$$

The turbulent field, which has constant field strength in each of the domains, is assumed to have a cell-like structure. The edge length of the cells is determined by the coherence length. As coherence length often the order of magnitude of a galaxy with about $10kpc$ is used. In the further work, however, the approach is used that there is a divergence-free homogeneous magnetic field with isotropic Gaussian turbulence in the intra cluster medium, which has a mean value of zero and a variance of $\mathcal{B}^2$. This gives a much better description of the observed large and small scale fluctuations [Murgia2004]. The turbulence is supposed to follow a power law in wavenumbers $M(k) \propto k^q$ between $k_L \leq k \leq k_H$ and zero otherwise. Here q denotes the turbulence spectral index whereas k_L and k_H indicate the minimum and maximum turbulence scale, which are calculated from

$$k_{L,H} = \frac{2\pi}{\Lambda_{max,min}} \tag{4.10}$$

where $\Lambda_{max,min}$ gives the maximum and minimum field fluctuations in kpc, respectively. For the mixing of photons and ALPs only the magnetic field component transversal to the photon propagation direction (z) is relevant. The spatial correlation of this component can be calculated using

$$C(z) = \langle B_\perp(\vec{x}) B_\perp(\vec{x} + z\vec{e}_3) \rangle \tag{4.11}$$

Via the integral along the line of sight the coherence length can now be calculated

$$L_{coh} = \frac{1}{C(0)} \int_0^\infty C(z) dz \tag{4.12}$$

Now that the general morphology of the ICM has been clarified and the most important properties such as turbulence scales or turbulence spectral index and coherence length have been introduced, it is time to take a closer look at the special features to be considered in the case of the virgo cluster.
The extreme conditions near the central black hole, which are also underlined by the electron density model, motivate to divide the ICM into two regimes which follow the same morphology, but differ significantly in terms of turbulence and coherence length.
The subdivision is made such that there is an "inner" magnetic field regime , which extends to a distance of 2kpc from the central AGN, and an outer one, which extends from 2kpc to 1000kpc, the virial radius.
For the inner part, the magnetic field is changed with respect to the turbulence scales and the turbulence spectral index so far that 10 domains result, for which a coherence length of 0.2kpc each is calculated as proposed by (Guidetti, 2011). The modeling of the magnetic fields and the calculation of the coherence length is done with the *gammaALPs* framework.
For the first magnetic field regime, a maximum turbulence scale of $k_H = 6800\text{kpc}^{-1}$ is obtained, corresponding to very small minimum field fluctuations, which may well be expected near the highly active central zone. The minimum turbulence scale is $k_L = 0.42\text{kpc}^{-1}$ and the turbulence spectral index is $q = -2.9$. In the outer magnetic field regime, the maximum turbulence scale changes to $k_H = 12\text{kpc}^{-1}$ and the spectral index to $q = -2.5$, whereas the minimum turbulence scale does not change. All values are consistent with or taken from already introduced literature.
To model the ICMF along the line of sight to M84, which is only needed to perform the Faraday rotation comparison, the same magnetic field parameters are used as for the previously discussed outer magnetic field, due to the large distance to the M87 AGN.
The relationship of the electron density of the ICM and the transverse components of the corresponding magnetic fields is shown in Figure 4.4. Here, the motivation to divide the magnetic field into two regimes becomes clearly visible by the strongly increasing electron density in the center region. A realization of the two magnetic field regimes along the line of sight to M87 and a comparative representation of the Virgo ICMF along the lines of sight to M87 and M84 respectively are shown in Figure 4.5.
The final ingredient for the intracluster magnetic field model is the central magnetic field strength, B_0, and its decrease with increasing distance, η, from formula 4.7.

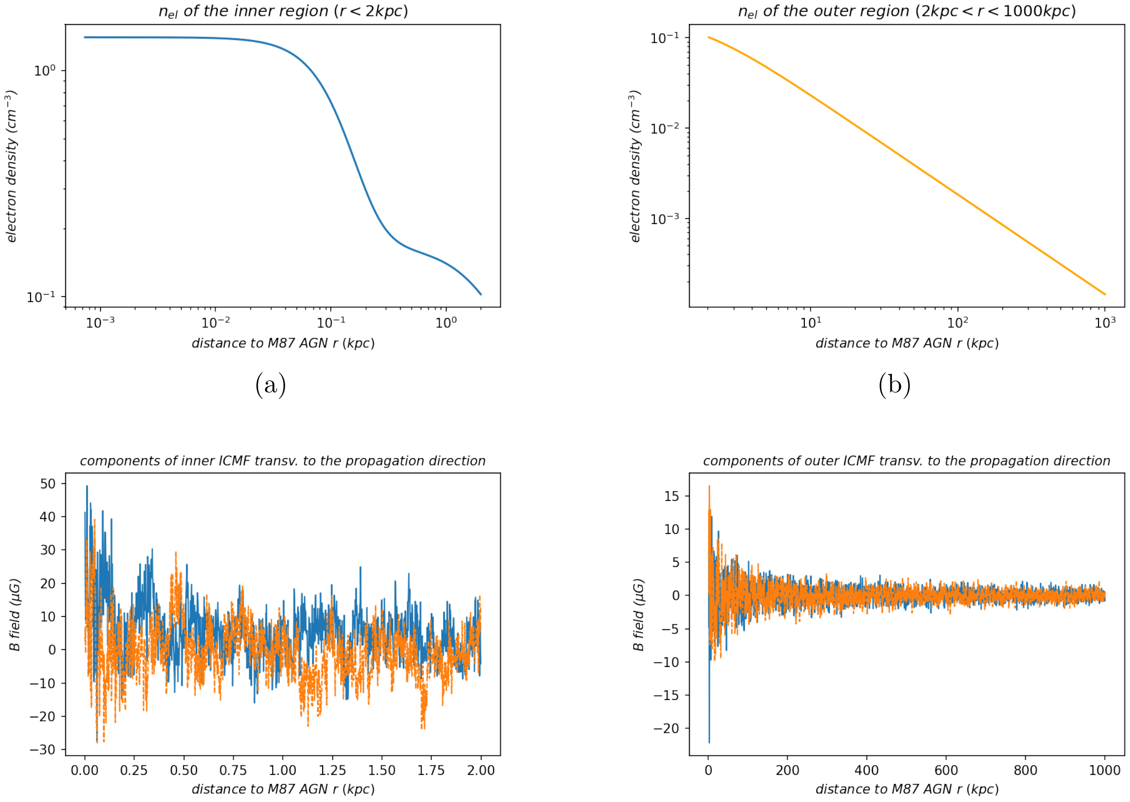

(a)

(b)

(c)

(d)

Figure 4.4.: Figure (*a*) and (*b*) show the model of the electron density for the inner as well as for the outer region as it is integrated by *gammaALPs* with the help of the passed fitting parameters. Figures (*c*) and (*d*) show the transverse components of the magnetic field along the line of sight for both the inner and outer regions. For the latter, all parameters of the magnetic field are already determined (see Table 4.2) and passed to *gammaALPs*.

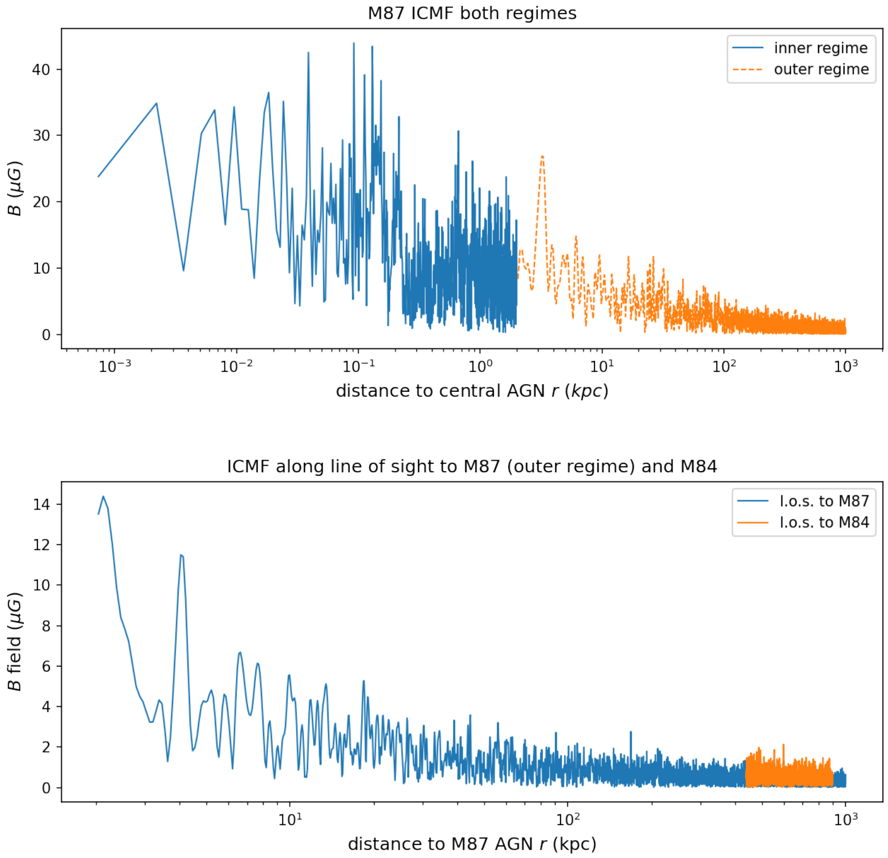

Figure 4.5.: The upper panel shows the strength of a random realization of the turbulent magnetic field (both regimes in succession). The lower panel, on the other hand, shows the outer magnetic field regime (of the same realization) along the line of sight to M87 compared to the field along the line of sight to M84.

Constraining the model parameters

To narrow down these parameters, simulated and observed Faraday rotations or their derived quantity rotationmeasure are used. The Faraday effect refers to the magneto-optical effect which is responsible for the fact that the polarization axis of a linearly polarized electromagnetic wave rotates when it interacts with a magnetic field parallel to its propagation direction while passing through a medium. This is illustrated in figure 4.6

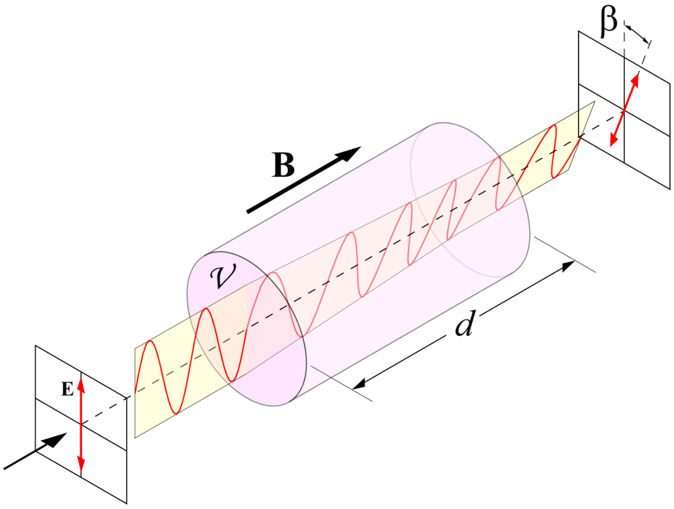

Figure 4.6.: Polarization mechanism due to the Faraday effect. (open source)

The rotation $\Delta\Psi$ of the position angle of the electric field vector $\vec{E}$ of linearly polarized radiation by magnetized plasma is given by:

$$\Delta\Psi_{obs} = \Psi(\lambda) - \Psi_{int} = \lambda^2 \times RM \tag{4.13}$$

where $\Psi(\lambda)$ is the observed position angle of $\vec{E}$ observed at a wavelength λ and Ψ_{int} its intrinsic angle. RM is the rotation measure and can be calculated from the line-of-sight integral:

$$RM_{[rad\ m^{-2}]} \approx 812 \int_0^z dz' B_{\|}(z') n_{el} z' \tag{4.14}$$

where n_{el} is the electron density and $B_{\|}(z)$ is the magnetic field parallel to the propagation direction. From 4.14 it is visible that if the electron density is known, conclusions can be drawn about the strength of the magnetic field along the line of sight by means of observed or simulated RM.

In order to use this to constrain our magnetic field model with respect to B_0 and η, the approach from (Marsh et al., 2017) is applied. First, the RM is simulated by means of 4.14 for 500 realizations of the magnetic field and several combinations of the parameters B_0 and η using the *gammaALPs*. Since a statistically isotropic magnetic field is uniformly distributed

around zero, the average of several *RM* simulations must also be zero. Nevertheless, to obtain reasonable values for the fluctuations of the *RM* to constrain the ICMF, its standard deviation is used instead. In the following, the *RM* is calculated via a loop over B_0 with $14\mu G \leq B_0 \leq 62\mu G$ ($\Delta B_0 = 4\mu G$) as well as over η with $0.1 \leq \eta \leq 0.7$ ($\Delta\eta = 0.1$) and the variance of the *RM* over all realizations is stored for each combination of B_0 and η. The square root is used to obtain the standard deviation, which is color-coded in a grid spanned by the two parameters. In order to obtain a finer grid, the obtained values for $\sigma(RM)$ are interpolated using the *RectBivariateSpline* method of the *Python Scipy* library to obtain $\Delta B_0 = 0.5\mu$ G and a $\Delta\eta = 0.01$. Figures 4.7 and 4.8 show the $\sigma(RM)$ along the line of sight to both M87 and M84 already in the finer grid as well as each with the contour lines of constant $\sigma(RM)$ values. If the contours of both figures are superimposed, the color-coded values for RM lose their meaning and their dependence on the values for the parameters B_0 and η can be seen.
It is expected that the results will be similar to those of the authors, but will have different values due to the particular focus on the center region of the M87 AGN. Also the different approach in the determination of the distance of the two galaxies to the Earth, or the distance to each other, can certainly lead to a deviation of the *RM* values. To make the influence of the center region visible, the *RM* was calculated three times, once starting directly at the source, i.e., a few pc away from the black hole, once starting 500pc away, and once starting 1kpc away (see Figure 4.7).
Comparing the contour lines of the three figures, it can be seen that the RM very close to the black hole depends very strongly on the central magnetic field strength B_0 and less on the attenuation coefficient η. This is expected since the attenuation depends on the distance to the origin, i.e. $n_{el}(r = 0)$. With increasing distance, one sees a larger and larger influence of η. Also, high *RM* values are only reached at comparatively high B_0. Also as expected, this development is much more pronounced in the first 500pc than at further distance to 1000pc.
For M84, of course, the considerations made for M87 are completely irrelevant, since the RM is calculated along the line of sight to Earth. What is clearly of interest, however, is the distance between the two galaxies (the problem of this distance has already been explained in Chapter 3). Since we assume that the electron density of the Virgo cluster decreases radially with their distance to the central AGN and thus also the magnetic field strength, 600kpc between minimum and maximum distance of the two galaxies is quite a quantity which can have influence on the RM calculation. Figure 4.8 shows the contour lines for the maximum and minimum distance between M87 and M84.
The figures suggest that the *RM* at distances from the central black hole of this magnitude depends mainly on η. This dependence does not change significantly with increasing distance, but the value of the RM decreases.
A comparison with the literature shows that the values obtained here for the RM of M87 are about 1000rad m^{-2} higher for the same regions of B_0 and η. For M84, they are significantly lower. In the case of M87, the high values obtained are quite consistent with the observations from (Guidetti, 2011) and result from the different treatment of the center region. The difference in the values for M84 may be due to the higher assumed distance to M87 as well as to slight differences in the underlying model of the electron density. Analogous to

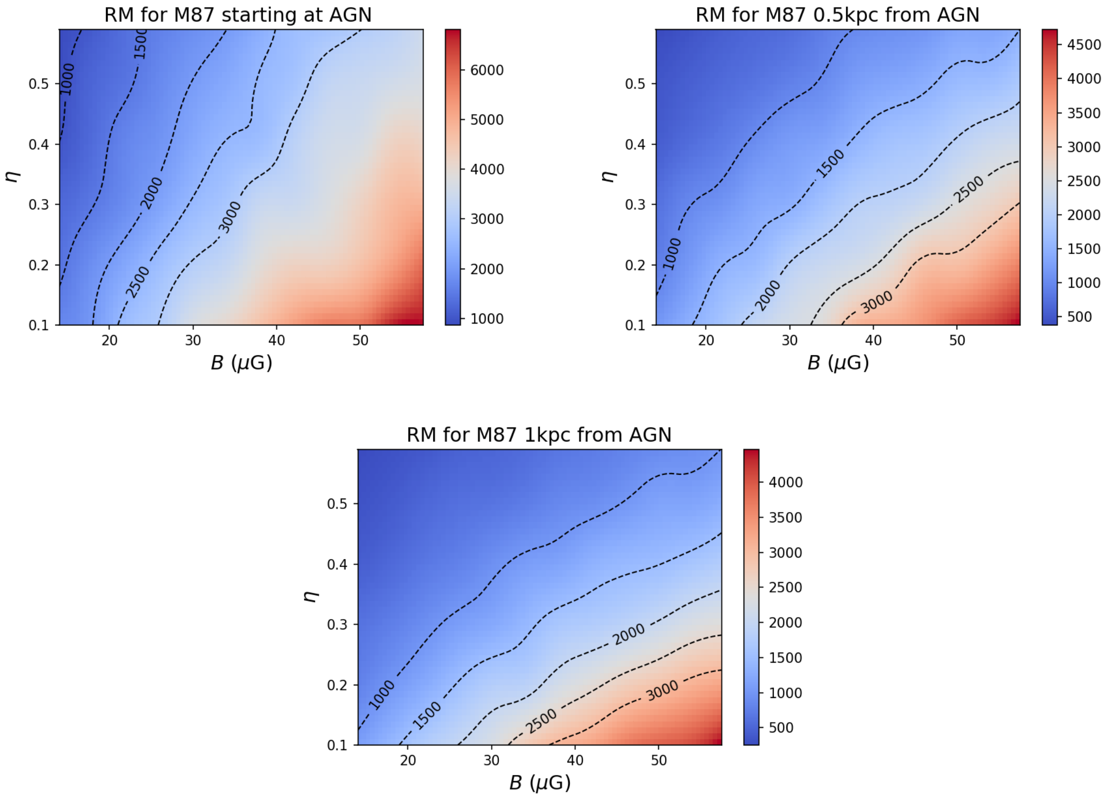

Figure 4.7.: $\sigma(RM)$ contour lines for RM calculations started directly at the source (top left), 500pc away (top right) and 1000pc away (bottom center). All values in rad m^{-2}

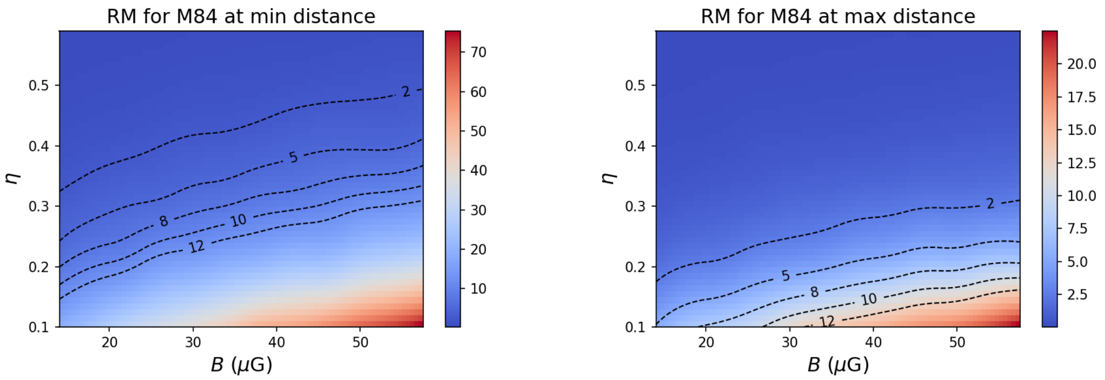

Figure 4.8.: $\sigma(RM)$ contour lines for RM calculations with an assumed distance between M87 to M84 of $440kpc$ (left) and $1200kpc$ (right). All values in rad m^{-2}

the literature, the intersection of a contour line of M87 and one of M84 are chosen for the determination of the parameters B_0 and η as shown in Figure 4.10. Based on the differences described above, the $\sigma(RM_{M87}) = 2500$rad m^{-2} line was chosen for M87 instead of the 1500rad m^{-2} line and the $\sigma(RM_{M84}) = 2.5$rad m^{-2} line was chosen for M84 instead of the 5rad m^{-2} line. The corresponding values for B_0 and η are 36.9μG and 0.44, respectively (versus 31.6μG and 0.54).

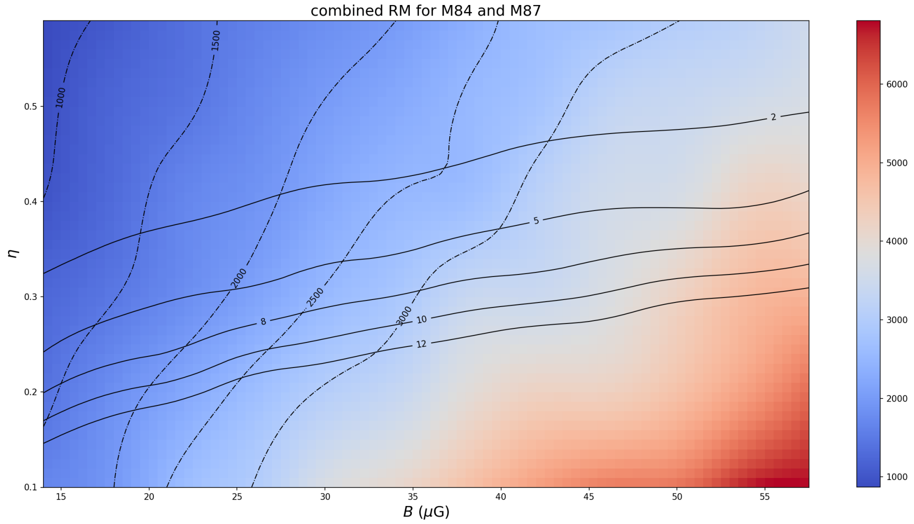

Figure 4.9.: Superimposed contour lines of equal values of $\sigma(RM)$ calculations along the lines of sight to M87 and M84 (solid lines for M87, dashed dotted lines for M84). The underlying values of the RM are those for M87 and are no longer relevant for the consideration of the contour lines. To determine the parameters of the magnetic field, the intersection of the $\sigma(RM_{M87}) = 2500\text{rad m}^{-2}$ line and the $\sigma(RM_{M84}) = 2.5\text{rad m}^{-2}$ line was chosen (shown as $\sigma(RM_{M84}) = 2\text{rad m}^{-2}$ line in the figure), which gives the parameter pair $(B_0, \eta) = (36.9\mu G, 0.44)$

The chosen values are quite consistent with the estimated values in the literature. In a simulation of the M87 RM based on VLA data, it can be seen that values around 2500rad m^{-2} may well be expected in the central region of the galaxy.

The higher central magnetic field strength can be explained by the fact that the model of the electron density is much closer to the central AGN and has an electron density at the maximum that is higher by a scant order of magnitude. The stronger decrease of the field strength with increasing distance caused by η, on the other hand, cannot be explained unambiguously, but may possibly be related to the differences in the electron density model. Table 4.2 shows the complete model for the Virgo galaxy cluster with respect to the electron density of the intracluster medium as well as the intracluster magnetic field in particular. This model forms the basis for the following analysis of the theoretical photon ALP conversion, which is performed by calculating the photon survival probability.

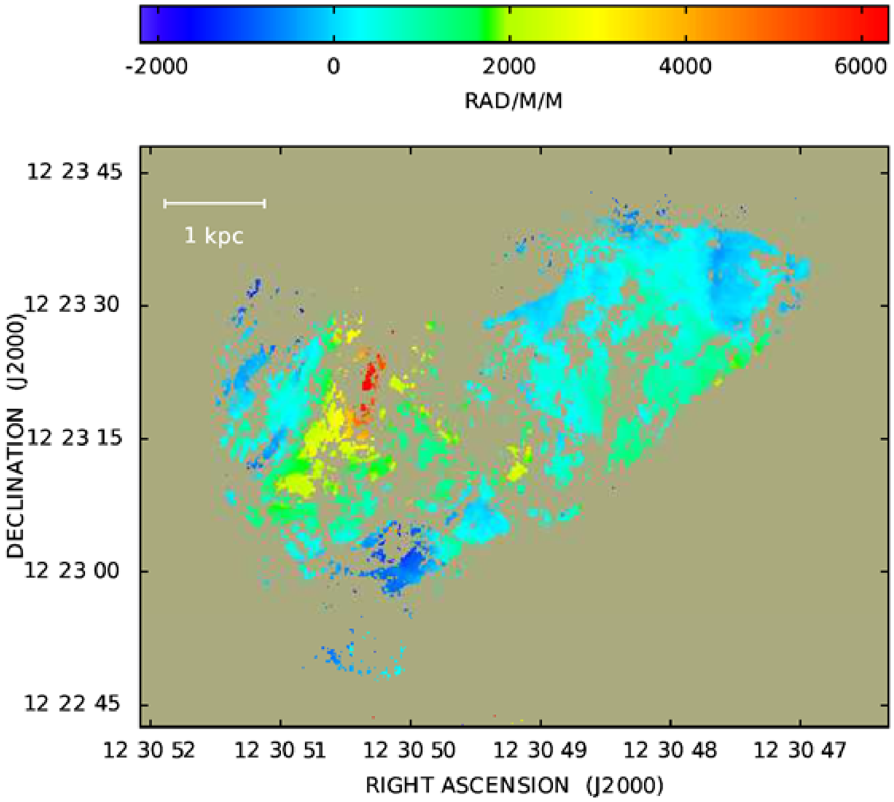

Figure 4.10.: Computed rotation measure of M87

ICM		ICMF	
n_0	123.73	B_0	36.9μG
n_2	164.15	η	0.44
β	2.25	$k_{min,1}$	6800kpc^{-1}
β_2	0.55	$k_{max,1}$	0.42kpc^{-1}
r_{core}	0.15	q_1	-2.9
r_{core2}	1.72	$k_{min,2}$	12kpc^{-1}
		$k_{max,2}$	0.42kpc^{-1}
		q_2	-2.5
		r_{max}	1000kpc

Table 4.2.: Model parameters of the "*double beta*" fitting function for the intracluster medium (ICM) as well as those of the subdivided intracluster magnetic field (ICMF)

4.3. Conversion probability

Now that the model for the Virgo cluster, consisting of ICMF and the ICM electron density, is set up, we proceed to the calculation of the conversion probability. The path of gamma photons considered in this work is divided into photon propagation modules. Each module takes into account a possible attenuation of the photon beam, either by photon ALP conversion or attenuation by the extragalactic background light (EBL, which will be explained in chapter 5). The modules considered are

1. Modul 1, ICMF (inner region)
2. Modul 1, ICMF (outer)
3. Modul 2, EBL attenuation
4. Modul 3, galactic magnetic field (of our milkyway)

The elaborated model parameters for the ICMF are passed to the *GammaALPs* code. For the modules 3 and 4 already existing models are taken over and are not of further importance. Besides the photon propagation modules, the number of random magnetic field realizations can be specified and the values of the parameters ALP mass and coupling strength can be preset. The photon - ALP conversion was already derived in chapter 2. For all following calculations an initial unpolarized photon beam is assumed. It is further assumed that at the origin of the gamma photons only photons and no ALPs are produced and therefore the third diagonal element of the polarization matrix, which represents the ALP state, is zero. The probability of the polarization state at the end of the photon's journey is described by equation 2.23, where the individual diagonal elements are exactly the objet of interest of the further procedure.
The matrices $\mathcal{T}(z_{i+1}, z_i; E)$ are calculated by the *GammaALPs* code for all desired energies as 4-dimensional arrays (stacks of 3-dimensional arrays, containing polarization state and energy) and then matrix multiplied along the z-Axis.
The result of this calculation will be a value for the final photon polarization $\rho(x)$ or in $\rho(y)$ direction for a detected photon. To be able to detect a photon at all, it must of course arrive as such and not as (non-detectable) ALP. This is why the photon survival probability $\rho(x) + \rho(y)$ is calculated. If the added probability is smaller than 1, photons of the corresponding energy must have been lost either by scattering or adsorption, or must have arrived as ALP at the detector.

In order to make a good choice of ALP parameters for which $\rho(x) + \rho(y)$ shall be calculated, first the critical energy (see equation 2.17) for some combinations of m_a and g_a was calculated and checked whether it´s magnitude lies within the range which we expect for gamma photons (and which are in the sensitive range of the H.E.S.S. telescope). The resulting survival probability is plotted against the photon energy and examined for dips at certain energies. Such "dips" should then be interpreted as photons "lost" by photon-ALP conversion.

For the calculation of the photon survival probability the following values for ALP parameter, number of magnetic field realizations and energy bins were chosen respectively.

Parameter	values				
ALP mass m_a (neV)	31.6	100.0	316.2	1000.0	
ALP coupling constant g_a (10^{-11}GeV)	0.1	0.32	1.0	3.16	10.0
Energy bins	200				
Magnetic field realizations	500				

Table 4.3.: Values for ALP mass m_a and coupling strength g_a as well as energy bins are evenly spaced in logarithmic scale. Thus, the values for the ALP mass goes in four steps from $10^{1.5}$ to 10^3 and the coupling strength in five steps from 10^{-1} to 10^1. The energy range is 100GeV - 50TeV.

For better clarity, only the results of the largest and smallest ALP parameter combinations are shown here in Figure 4.11. When focusing the figures of the parameter pairs ($m_{a,1} = 31.6neV, g_{a,1} = 0.1 \times 10-11GeV^{-1}$) and ($m_{a,2} = 1000neV, g_{a,2} = 10.0 \times 10^{-11}\mathrm{GeV}^{-1}$), it becomes clear on what to pay attention to when interpreting the photon survival probability curves. In the first case, it is noticeable that although the curve contains a lot of "dips", the survival probability never falls below 99%. Photon - ALP oscillations won't be observable here. The second pair of parameters presents a completely different picture. Here there is a small dip at about 100GeV and strong dips at energies above one TeV. With these ALP values, photon - ALP conversions in the energy range of interest (i.e. sensitive energy range of the H.E.S.S. telescope) could be assumed. In the final chapter we will investigate to what extent the observations of the calculations performed in this section can also be transferred to a real H.E.S.S. data set.

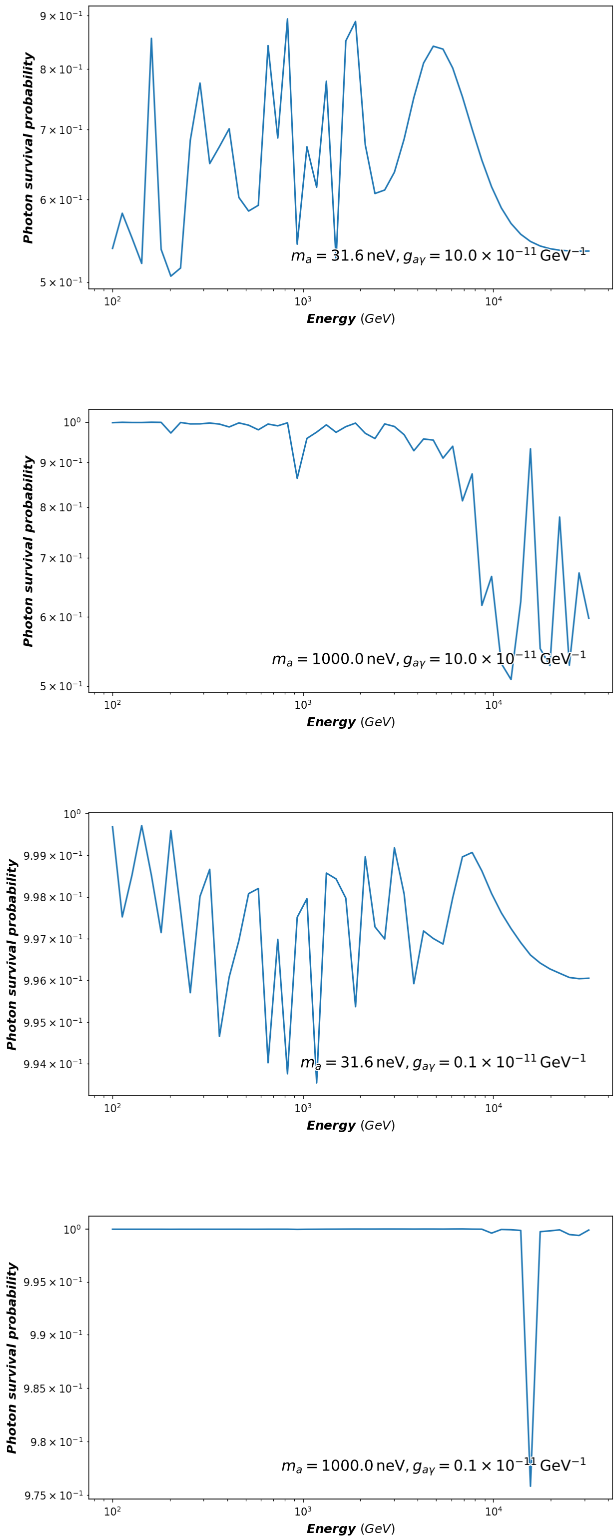

Figure 4.11.: Photon survival probabilities of the combinations with respectively largest and smallest mass and coupling constant

5. Searching for photon - ALP oscillations in the spectrum of M87

In the final chapter of this thesis, the photon survival probabilities calculated using the model constructed in Chapter 4 are used to search for photon ALP oscillations in the M87 spectrum. This search is divided into 4 sections: The first section presents the HESS telescope data set used. Then, in the second section, a spectral model is fitted to this data set using the phython module gammapy. In the same way, a spectral fit to the data set is now fitted for each combination of ALP parameters from Chapter 4. In the process, each fit is given a "score value" which evaluates the plausibility of the fit. Section 4 introduces the statistical method profile likelihood, which is used to make a statement with the score values whether a spectral fit with assumed Photon ALP transformation describes the data set better than the conventional fit from the second section. All spectral fits to the H.E.S.S. data set as well as their graphical representations were created using the Python package *gammapy* version 0.18.2. The corresponding code written for this chapter can be found in Appendix B.

5.1. The H.E.S.S. data set

HAP analysis data

The H.E.S.S. telescope was already introduced in chapter 2. Now the origin of the spectral data set used in this chapter shall be briefly discussed. This originated in a series of observations made between 2004 and 2016 as part of a long-term monitoring of M87. The data used are from the HAP analysis chain and was provided as a high level dataset, the corresponding analyses were not performed or reviewed in this work. Table 5.1 contains a summary of the observations, where the annually performed runs, the respective orientation with respect to the zenith as well as the measurement duration in hours are given. The value for Signal corresponds to the significance of the measurement.

Year	Runs	Zenith [°]	Live time [h]	Signal	Safe energy range [TeV]	Livetime [h]	Signal
2004	69	36 - 50	29.0	7.4	0.24 - 62	24.3	6.2
2005	50	36 - 51	19.8	18.3	0.26 - 68	18.1	18.2
2006	9	36 - 45	3.6	5.1	0.29 - 62	2.5	4.4
2008	28	36 - 58	12.0	4.5	0.29 - 62	8.1	1.9
2010	21	36 - 49	9.3	13.4	0.32 - 91	7.9	7.5
2011	5	36 - 37	2.1	1.5	0.32 - 62	2.1	1.5
2012	15	36 - 50	6.4	6.0	0.29 - 62	5.6	5.2
2013	24	36 - 48	9.7	4.8	0.29 - 62	9.7	4.8
2015	123	36 - 51	58.4	9.4	0.22 - 62	55.3	9.0
2016	18	36 - 53	7.5	1.9	0.32 - 62	3.9	1.6

Table 5.1.: M87 Observation summary for H.E.S.S HAP analysis chain with the available runs on the left side and the runs surviving the spectral selection on the right side

The evaluation of the statistical reliability of measured gamma photon events is an important part of the analysis. Since a measurement of gamma photons from M87 is a counting experiment, it must be assumed that it obeys a Poisson law. For this reason, significance can be determined by the ratio of the observed signal (i.e., the probable number of photons originating from the source) with its standard deviation (Li & Ma, 1983). The number of signal photons n_S is obtained from the number of photons from the source area reduced by the background photons. The latter are determined by a measurement of the background, where the difference of the measurement time of source and background is considered by the quantity α. The background signals are thus estimated by $n_b = \alpha n_{off}$. The variance of the source photons is calculated by

$$\sigma^2(n_S) = \sigma^2(n_{on}) + \sigma^2(\alpha n_{off}) = \sigma^2(n_{on}) + \alpha^2\sigma^2(n_{off}) \tag{5.1}$$

and thus the standard deviation by

$$\sigma(n_S) = \sqrt{\sigma^2(n_{on}) + \alpha^2\sigma^2(n_{off})} = \sqrt{n_{on} + \alpha^2 n_{off}}. \tag{5.2}$$

The significance results thus to

$$S = \frac{n_S}{\sigma(n_S} = \frac{n_{on} - \alpha n_{off}}{\sqrt{n_{on} + \alpha^2 n_{off}}} \tag{5.3}$$

The left image in Figure 5.1 is an example of a skymap (Dyrda et al., 2015) where the significance is plottet. The particularly bright region in the center, where the significance is maximum, is the object of interest. In the figure, this object is the galaxy PKS 0625-354, but using M87 AGN as object of interest provides a comparable picture. The right image of figure 5.1 shows an example for the selection of background regions as it is performed by *gammapy*. It is performed by setting several additional regions distributed on the skymap outside the source.

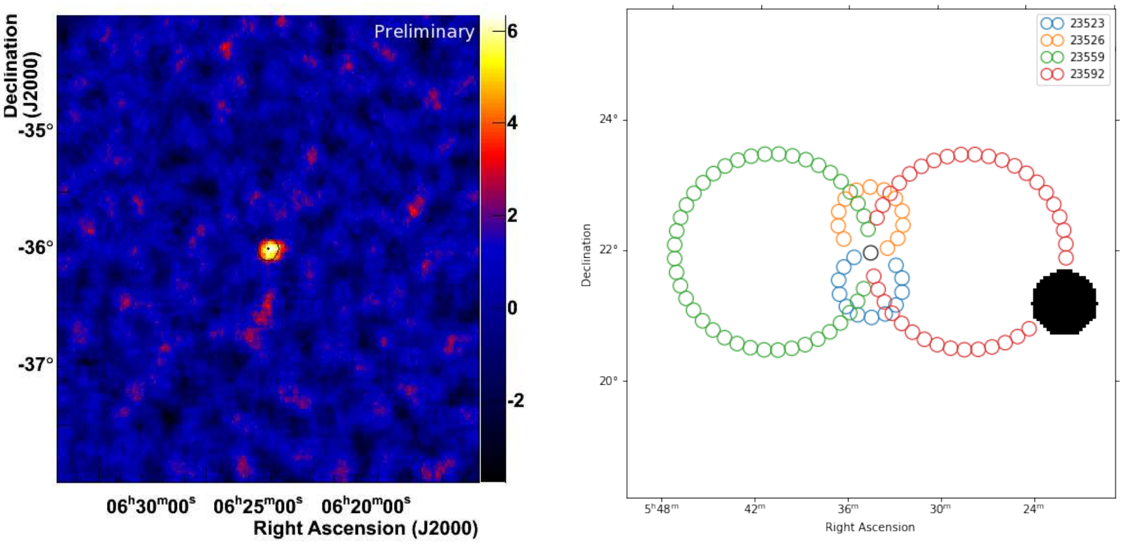

Figure 5.1.: The left image shows a significance map of VHE photons of the galaxy PKS 0625-354, which were detected by H.E.S.S.. The source of the photons, i.e. the region of interest, is marked by a circle in the center. The right image shows an example of a method to place off-regions to estimate the background level. The black mark in the middle is again the region of interesst.

Also with this method the signals must be put into relation with each other, because many off regions are selected but only one on region. If the amount of background signals related to the source is determined, this can be subtracted from the amount of all signals and the excess counts are obtained. Figure 5.3 shows these excess counts divided into several photon energy intervals, the energy bins.

5.2. Fit of a global model to the spectrum

Now, the H.E.S.S. data set is subjected to a spectral analysis. For this purpose, all observations are stacked and a global model shall be fitted to the spectrum. In this work, in addition to the usual power law (equation 5.4), a more general logParabola model (equation 5.5) is also fitted to the spectral data.

$$\phi(E) = \phi_0 \cdot \left(\frac{E}{E_0}\right)^{-\Gamma} \tag{5.4}$$

$$\phi(E) = \phi_0 \cdot \left(\frac{E}{E_0}\right)^{-\alpha-\beta\ ln(\frac{E}{E_0})} \tag{5.5}$$

The attenuation of the photon beam by the Extragalactic Background Light (EBL), which has not been taken into account so far, must also be added to the spectral model. For the optical density τ of the EBL the model of (Finke, Razzaque, & Dermer, 2010) is used in this work. The attenuation depends on the photon energy and the distance given as redshift z and is calculated as follows

$$\text{EBL attenuation} = e^{-\tau(E,z)}. \tag{5.6}$$

In a first attempt it was assumed, due to the relatively small distance, that the EBL does not cause a significant attenuation in this case. After a comparison of the attenuation with EBL and without the described EBL model (see Figure 5.2) it became obvious that the EBL attenuation is quite significant.

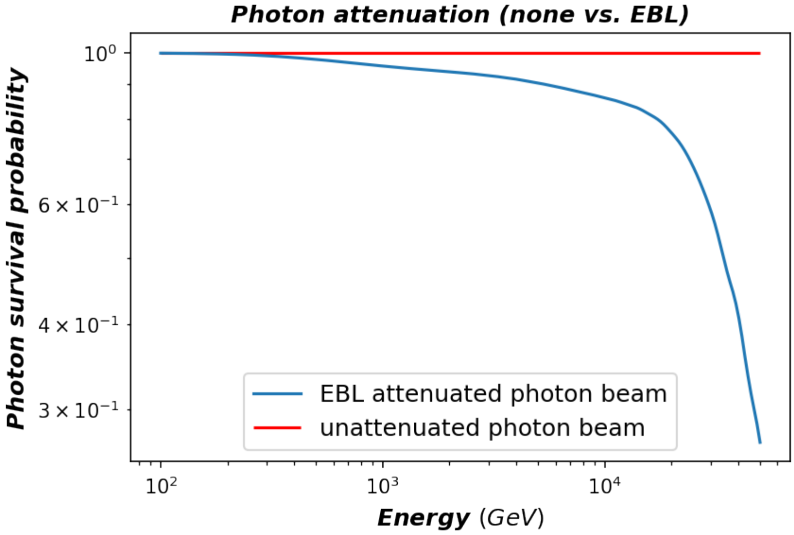

Figure 5.2.: Attenuation of the photon beam due to extragalactic background light compared to an unattenuated photon beam representing a photon survival probability of 100%.

The graphic shows that at an energy of 1TeV an attenuation of 20% has to be expected. In order to modify the models accordingly, an adaptable template model is created which reflects the percentage attenuation due to the EBL. This is integrated into the spectral models. The result is a called a compound model.

The maximum likelihood method

For a selected model ϕ, gammapy calculates the expected number of signal counts using

$$\mu_i(\boldsymbol{\xi}) = T_{obs} \int_{\Delta E_i'} dE' \int_{E-range} dE \int_{\boldsymbol{p}-range} d\boldsymbol{p}\; R(E, E', \boldsymbol{p})\phi(E, \boldsymbol{p}, \boldsymbol{\xi}) \tag{5.7}$$

where ϕ represents the selected spectral model (in units $\mathrm{TeV}^{-1}\mathrm{cm}^{-2}\mathrm{s}^{-1}$) and $\boldsymbol{\xi}$ its parameters. R stands for the instrument response function which includes the effective area, the point spread function (PSF) and energy dispersion. Although the photon source is treated as a point source, the detector cannot represent one as such. The PSF indicates how point objects are imaged by the detector. For such point sources, ϕ contains a delta function in $\boldsymbol{p}$.The integral over the range of $\boldsymbol{p}$ performs the convolution of the PSF with the chosen spectral model.

In the case of the power law, the parameters amplitute ϕ_0 and index Γ are to be fitted to the model, while the reference energy is set to $E_0 = 1TeV$. In the case of the logparabola model, the amplitute ϕ_0, but also the numerical values for the curvature α and β are to be fitted. The reference energy $E_0 = 1$TeV is kept in this case. The energy range of the H.E.S.S. data set is from 0.26 TeV to 100 TeV, where the measured photon counts are divided into 73 energy bins equally spaced in logarithmic energy. Looking at the excces counts plotted in Figure 5.3 it can be seen, that for energies above an energy of 20TeV, there is a maximum of one estimated excess count. This shows that only extremely few photons with an energy above 20TeV were detected. It was found that these low counts led to numerically instable fit results. As a consequence the energy bins with the 17 highest energies are excluded and the resluting energy range then goes from 0.26 TeV to 19.57 TeV.

To calculate the best fit parameters of the models the maximum likelihood method is used. The likelihood function is a real-valued function of mathematical statistics, which is obtained from a probability density function. It measures the goodness of fit of a statistical model to a data set. The difference between likelihood and probability is that probability is a property of a data set, i.e. how likely it is to obtain exactly this data given the parameters of the distribution function. Likelihood, on the other hand, is a property of the parameters (Gorman, 1960). Let there be a probability model for a given data set, which depends on the parameters of interest $\mu = (\mu_1, ..., \mu_k)$ but also on the background parameters $b = (b_1, ..., b_l)$. If we have independent observations $X = (X_1, ..., X_n)$ and a probability density function $f(x|\mu, b)$, the complete likelihood function is given by

$$L(\mu, b|X) = \prod_{i=1}^{n} f(X_i|\mu, b). \tag{5.8}$$

In our case, $(\mu_1, ..., \mu_k)$ represent the expected counts, and $(b_1, ..., b_l)$ the background counts. In order to choose the best model parameters,the values that maximize the likelihood function have to be found. For this purpose the method of maximum likelihood is used. Most common probability distributions (especially the exponential family) are only logarithmically concave and the concavity plays a key role in the maximization (Kass, 1989). For this reason, log-likelihood lnL is used. Since the logarithm is a strictly monotonically increasing function, the maximization of the likelihood function is equivalent to the maximization of the lnL function. The maximum likelihood estimator can be found by solving

$$\frac{\partial lnL}{\partial \mu_i} = 0,\ i = 1, ..., n \tag{5.9}$$

Due to the already mentioned Poisson distribution of the signals, the logarithm of the Poisson likelihood is used, which in our case is

$$lnL(\mu, b; \alpha_{exp}|n_{on}, n_{off}) = n_{on}\ ln(\mu + b) - (\mu + b) + n_{off}\ ln\left(\frac{b}{\alpha_{exp}}\right) - \frac{b}{\alpha_{exp}} \tag{5.10}$$

where μ are the expected counts, b the background counts, n_{on} is the number of counts in the signal region and n_{off} the number of counts in the background region. The exposure ration between both regions is reflected by α.
For the best fit parameters of the model the likelihood function maximizes. Gammapy calculates these values using the MINUIT (James, 1994) algorithm and outputs the maximum likelihood value multiplied by (-2) as cash fit statistic

$$C = -2\ lnL, \tag{5.11}$$

Figure 5.3 shows the excess counts already described, the signal counts expected by the selected model (in this case the power law model) with calculated best fit parameters as well as the selected energy interval within which the fit was calculated.

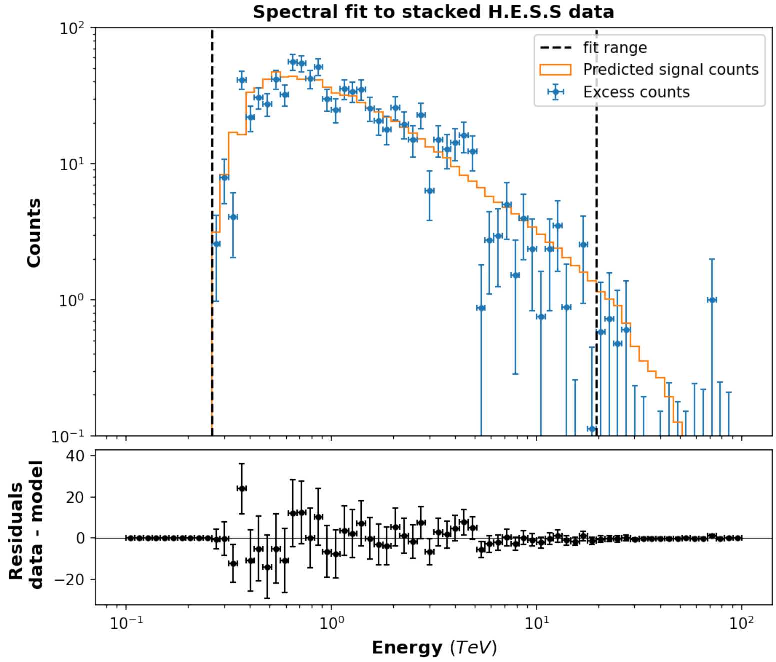

Figure 5.3.: Excess Counts (upper panel) with fitted power law model. The energy span over which the fit was calculated is indicated by dashed vertical lines. The difference between model and data points is shown in the lower panel.

To show both models more clearly, they are presented in figure 5.4 together with the flux points. In the case of the power law model, a version without EBL attenuation is also shown for comparison. The flux points are the result of a one point fitting over a small energy range. This corresponds to the measured maximum flux of gamma photons in the corresponding energy range. For greater clarity, the energy is squared on the ordinate.

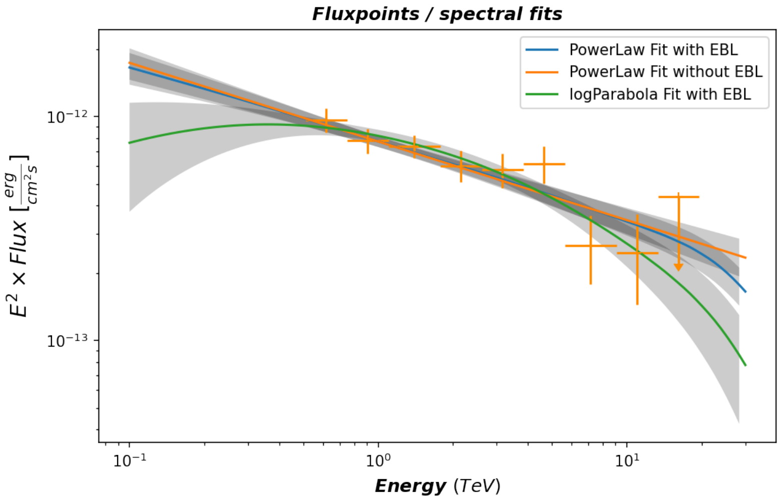

Figure 5.4.: Flux points of the stacked analysis (orange crosses) with the fitted spectral models: Power law without EBL attenuation (orange) and power law (blue) or logParabola (green) with attenuation.

The best fit values of both models are noted in Table 5.2.

Spectral model	Amplitude ϕ_0	Index Γ	α	β	$-2ln$L
Power Law	5.0531×10^{-13}	2.31	-	-	47.10
logParabola	5.3483×10^{-13}	-	2.1922	$1.0508 \times e^{-1}$	44.14

Table 5.2.: Spectral model best fit values

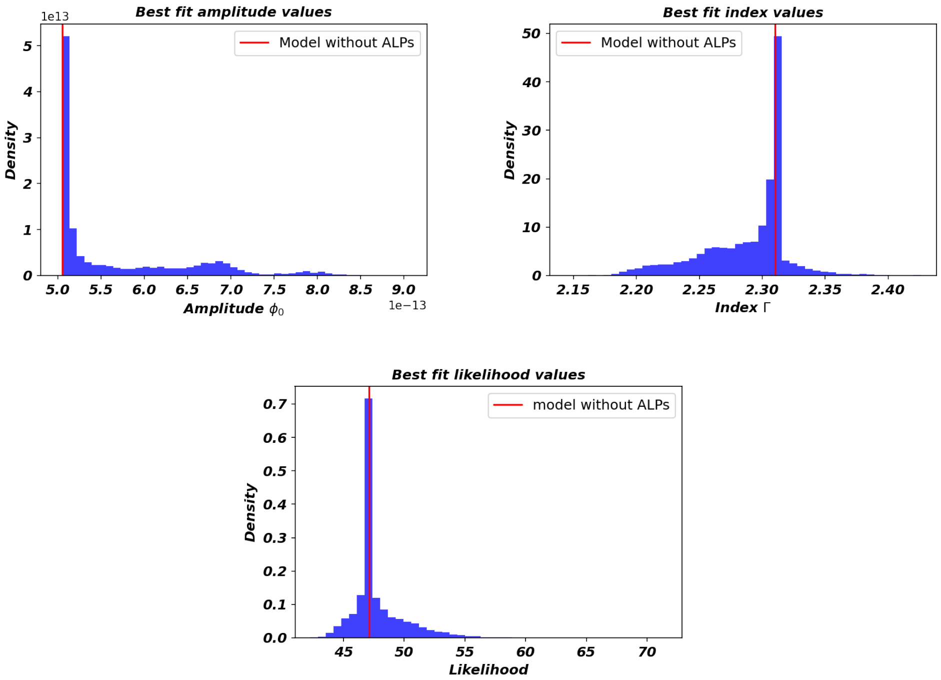

Figure 5.5.: Histograms of best fit values for power law spectral models with assumed photon ALP conversion. The parameters amplitude ϕ_0 and Index Γ were fitted. The likelihood value indicates the plausibility of the fit. The red lines correspond to the best fit value of the conventional power law spectral model.

5.3. Search for Photon ALP oscillations

To investigate whether the M87 AGN spectrum exhibits traces of photon ALP oscillations, the photon survival probabilities calculated in Chapter 4 must be taken into account when fitting the spectral models. To accomplish this, the same procedure is followed as before with EBL attenuation. The survival curves shown in figure 3, where the EBL attenuation is already taken into account, are integrated into the power law or logparabola model. Since we calculated the survival curves for each combination of the 5 chosen ALP coupling constants and 4 ALP masses and 500 magnetic field realizations each, 10000 fits each have to be calculated for the power law as well as the logparabola model. To illustrate the large amount of best fit parameters, a histogram was created for each parameter (see Figure 5.5 and 5.6). Here it is noticeable that the parameters scatter relatively closely around the best fit value of the model without assumed photon-ALP conversion. The only exception is the amplitute, which also peaks at the best fit value of the ALP free model, but nevertheless reaches values that are almost twice as high for both the power law and the logparabola model. One possible reason for this is the assumed initial unpolarized photon beam. A different initial condition of polarization could justify an amplitude of about double size.

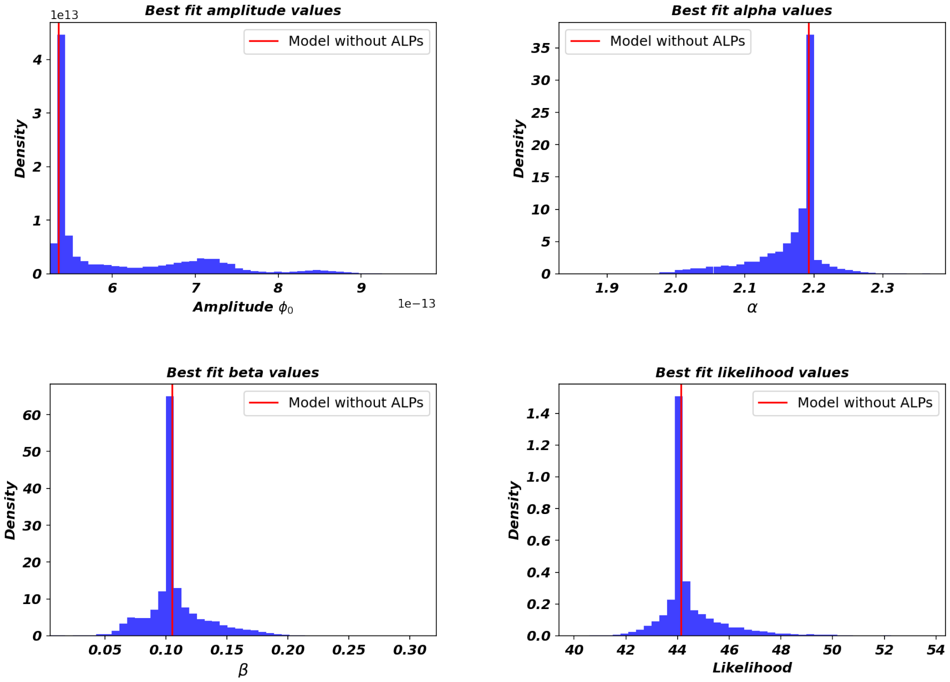

Figure 5.6.: Histograms of best fit values for logParabola spectral models with assumed photon ALP conversion. The parameters amplitude ϕ_0 and the values for α and β were fitted. The likelihood value indicates the plausibility of the fit. The red lines correspond to the best fit value of the conventional logParabola spectral model.

The profile likelihood method

In the next step, the classical way of hypothesis testing is taken, in which it is examined whether a hypothesis H_1 is statistically preferred with respect to the reference or the null-hypothesis H_0. The likelihood ratio test is based on the ratio between the maximum likelihood function of the H_1 hypothesis and the H_0 hypothesis. This ratio is given by

$$\lambda = \frac{max\ L(X|H_1)}{max\ L(X|H_0)}. \tag{5.12}$$

Wilks' theorem shows for sufficiently large μ and under the condition that certain regularity constraints are satisfied, that $2\ ln\lambda$ follows assymptotically a $\mathcal{X}^2$ distribution with n_{dof} degrees of freedom (Wilks, 1938). n_{dof} is the difference of the free parameters between H_1 and H_0. This shows why the output of the fit statistic in the form of 5.11 makes sense, because in this way $-2\ ln\lambda$ is simply the difference of the fit statistic of both hypotheses, i.e. ΔTS (TS for test statistic). For this reason, ΔTS also follows a $\mathcal{X}^2$ distribution with n_{dof} degrees of freedom, which leads to the fact that a classical significance can be calculated by simply taking the square root. Usually, the null hypothesis is the configuration in which the sought effect does not occur, which in our case is the existence of ALPs ($\pi = 0$).

It is important to note that the value for C is negative, that means the smaller the likelihood value the better it is. So, when looking at the ΔTS values, the following interpretation has to be made:

1. $\Delta TS\ >\ 0$, the null-hypothesis H_0 is to be preferred.
2. $\Delta TS\ <\ 0$, the alternative hypothesis H_1 is to be preferred.
3. $\Delta TS\ =\ 0$, neither of the two hypotheses is preferred.

Calculating the spectral fits over all ALP parameter combinations yields 500 each of the likelihood values C given in Equation 5.11. These 500 values correspond to the 500 random realizations of the magnetic field. In order to decide which realization to use, the likelihood values are sorted from worst to best and the realization at the 95% quantile is chosen (see Figure 5.7). This is to ensure that a good realization is chosen, but not one that just happens to fit the photon ALP conversion perfectly.
The profile likelihood is performed on the TS values of this 95% quantile. For this purpose, all values are arranged in a grid. The best (i.e. the smallest) value of this profile from ALP mass and coupling determines the best ALP parameters. This was the goal of this work.

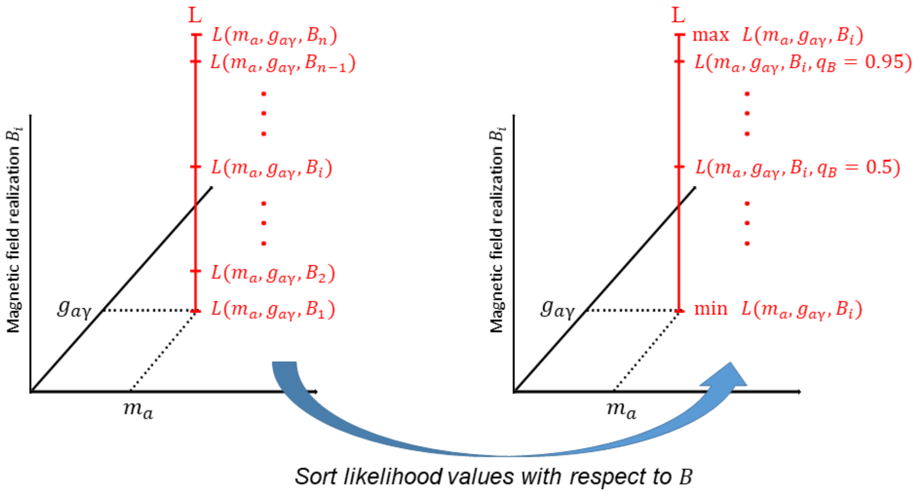

Figure 5.7.: Sorting the likelihood values of the random magnetic field realizations from worst to best (for each combination of ALP parameters) (Meyer et al., 2021)

Results and discussion

Figure 5.8 shows the resulting ΔTS values color coded for all combinations of m_a and $g_{a\gamma}$ for the power law as well as for the loparabola model. First, it is noticeable that higher values for the ALP coupling are preferred in both models. However, the plot of the power law model gives mixed results, which do not show a clear trend for the ALP mass. The most justifiable statement is that higher masses are preferred. For the generally slightly preferred logparabola model (see 5.2), however, a clear trend can be seen in the form of an imaginary diagonal from small ALP masses and couplings to large masses and couplings. Above this diagonal, the TS value improves in favor of the model with ALPs, with the best value being found at the smallest mass and the highest coupling. Below the diagonal, the TS value decreases to a value close to zero at the highest mass and the smallest coupling, where no statement can be made anymore which hypothesis is preferred. The preferred values for ALP mass and coupling are $m_a = 1000\text{neV}$ and $g_{a\gamma} = 10 \times 10^{-11}\text{GeV}^{-1}$ for the power law model and $m_a = 31.6\text{neV}$ and $g_{a\gamma} = 3.16 \times 10^{-11}\text{GeV}^{-1}$ for the logparabola model.

If Wilk's law is applicable, we can calculate the significance with which the best ALP model is preferred over the model without photon-ALP conversion via the square root of the TS value, which is equivalent to a significance σ between 1 and 2. This would be far from a detection requiring a significance of $\sigma \geq 5$ but still remarkable, since the conservative assumption is that the model without photon ALP conversion is preferred. Unfortunately, Wilk's theorem is not applicable in this case, since it requires that the background parameters of both hypotheses are known, which is not the case, since the background parameters of the ICMF are not considered in the null hypothesis. To take this into account, Monte Carlo simulations would have to be performed. Furthermore, the scatter of the likelihood values around the best fit without photon ALP conversion in the corresponding histogram in Figures 5.5 and 5.6 gives reason to assume that simply statistical fluctuations were fitted.

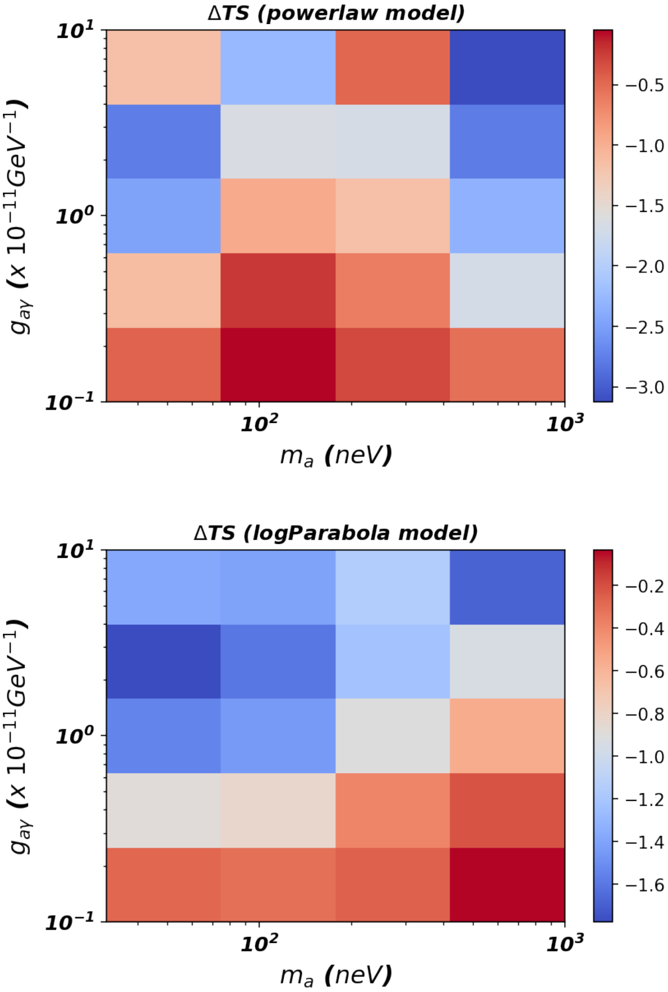

Figure 5.8.: ΔTS value for the spectral fit of all ALP parameters. The magnetic field realization was used, which was found at the 95% quantile of the likelihood value sorted from the worst to the best. The likelihood value of the model without assumed photon ALP conversion is subtracted from each value. In the upper panel the underlying spectral model is a power law model and in the lower panel it is a logParabola model.

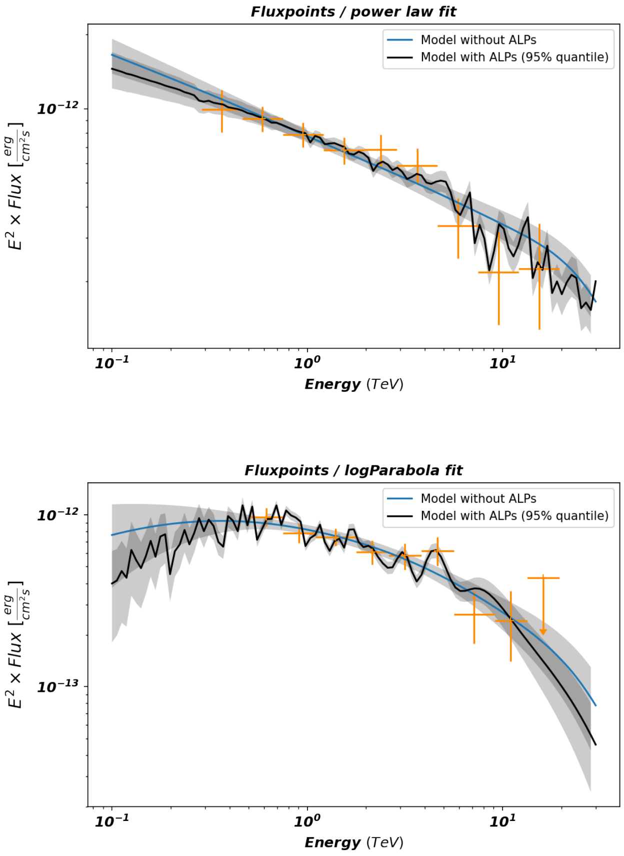

Figure 5.9.: The upper panel shows the comparison of the power law based fits with and without assumed photon-ALP transformation. The best fit ALP parameters are $m_a = 1000\text{neV}$ and $g_{a\gamma} = 10 \times 10^{-11}\text{GeV}^{-1}$. In the lower panel the fit is based on the logParabola model. Here the best fit ALP parameters are $m_a = 31.6\text{neV}$ and $g_{a\gamma} = 3.16 \times 10^{-11}\text{GeV}^{-1}$.

Finally, we compare the spectral fits of the null hypothesis, i.e. without assumed photon ALP conversion, and the best fit of the alternative hypothesis determined in this chapter. Figures 5.9 shows the comparison with the power law as the underlying model and the logParabola model, respectively. These figures also justify the assumption that only statistical fluctuations were actually fitted here.

6. Conclusion and Outlook

In the following, the concept and the most important findings of this work will be briefly summarized. Furthermore, the factors are named, which must be considered in order to be able to classify the compiled results adequately. Based on this, it will be discussed how the chosen approach could be refined and extended in future work. Finally, a view on future experiments for the detection of axion-like particles is given. In the first part of the thesis, the axion-like particle was motivated by the strong CP problem. The coupling of this particle to the electromagnetic field via the Primakoff effect was considered and the mixing between photons and ALPs was mathematically derived. High-energy photons from cosmic objects such as active galactic nuclei can thus covert into ALPs in extended magnetic fields on their way to Earth. The photon source chosen was the AGN of M87, the central galaxy of the Virgo Galaxy Cluter, and the magnetic fields considered were the intracluster magnetic field and the Galactic magnetic field of the Milky Way. In order to model the ICMF, a model of the electron density of the intracluster medium as a function of its distance from the AGN had to be created first, since the magnetic field model depends on it. For this purpose, data from the X-ray satellites ROSAT and Chandra were combined and fitted to a function already used to model the electron density of the Perseus ICM. Special attention was paid to the central region near the AGN, since the electron density increases extremely in this region. To account for this increase, the area under consideration was divided into two parts, with the inner part reflecting the central region of steeply increasing electron density and the outer part reflecting a steadily decreasing electron density with increasing distance. The ICMF, with assumed Gaussian turbulence, was also modeled according to this division. A magnetic field model established in the literature was used for this purpose. The field strength of this model decreases with increasing distance from the AGN and thus decreasing electron density. Due to the turbulence, the magnetic field model is composed of many sections with the extension of the coherence length, in which the magnetic field is assumed to be constant but randomly oriented. To constrain the model parameters of the magnetic field strength, simulations of the rotation measure derived from Faraday rotation are made and compared with the literature. to account for Gaussian turbulence, literature values of the turbulence scale are incorporated into the model and many random realizations of the magnetic field are calculated. For each of these realizations, the Photon survival probability was calculated using the derived equations for the photon-ALP mixture. This was done for a selected set of ALP parameter combinations in each case. In the last step, a data set with observations of VHE photons from M87 was analyzed. For this purpose, first a global spectral model was fitted to the data set using maximum likelihood method. The models chosen were firstly a spectral power law model and secondly a logparabola model. Subsequently, the photon survival probabilities were integrated into these models and fitted to the data set again for each ALP parameter combination and each magnetic field realization. A hypothesis test was performed using the profile likelihood method, where the model with no assumed photon ALP conversion was defined as the null hypothesis H_0. For the determination of the alternative hypothesis H_1, the likelihood values of all magnetic field realizations for each combination of ALP parameters were sorted from the worst to the best value and that realization was used which marked the 95% quantile. The test statistic value TS was calculated from the difference of H_1 and H_0 likelihood values. If this is negative, the null hypothesis is rejected; if it is positive, the null hypothesis is preferred. The results showed that for almost every combination of ALP parameters, the alternative hypothesis is to be preferred. Since Wilk's theorem is not applicable, significance cannot be directly inferred from the TS value. However, the processing of the likelihood values of all models with assumed photon ALP conversion in a histogram shows that possibly only statistical fluctuations were fitted here. Thus, the finding of this work is, in the best case, that although ALPs cannot be assumed to be detected, at least they are not rejected by the hypothesis test. In the worst case, only statistical noise was detected. Opportunities to follow up on this work and refine the methods used exist. A more possible approach is to revise the ICM electron density and ICMF models. Whether the electron density up to 2kpc distance from the AGN actually experiences this increase, or whether it is higher or lower, is unclear. Different models could be compared here. Also, modern X-ray satellites could provide better resolution data from the central region around the AGN. Another factor is the model of the ICMF. In a more advanced work, the model used here could be used, but the parameters B_0 and η could be treated as free parameters and the number of magnetic field realizations could be (significantly) increased. The Square Kilometre Array Observatory (SKA), currently under development, could improve our knowledge of the magnetic fields prevailing in M87 through a more accurate measurement of the Faraday rotation measure (Bonafede et al., 2015) and justify new ICMF models. Finally, a larger amount of spectral data from M87 in the targeted energy range is also needed. In this work, only the observations from H.E.S.S. have been analyzed. In a further work the addition of observations from the Magic IACT as well as the Fermi LAT gamma-ray space telescope would be conceivable.

The focus of this work was on creating a suitable workflow in using the Python packages GammaALPs and gammapy. This goal was achieved and the developed code can be used in future work. Due to the provided suggestions an extension and improvement is possible.

A. Electron density tables

ROSAT data for the ICM electron density

shell	$r(kpc)$	$n_e(cm^{-3}) \pm 1\sigma$	shell	$r(kpc)$	$n_e(cm^{-3}) \pm 1\sigma$
1	4.58	0.0763 ± 0.0004	20	110.32	0.00176 ± 0.00004
2	9.21	0.03017 ± 0.00021	21	117.21	0.00172 ± 0.00004
3	13.79	0.0175 ± 0.0006	22	124.11	0.00149 ± 0.00004
4	18.37	0.0136 ± 0.0005	23	131	0.00123 ± 0.00004
5	23	0.0105 ± 0.00025	24	137.9	0.00114 ± 0.00004
6	27.58	0.00839 ± 0.00021	25	147.11	0.001125 ± 0.000027
7	32.16	0.00697 ± 0.00018	26	156.27	0.000957 ± 0.000029
8	36.8	0.00607 ± 0.00016	27	165.48	0.000919 ± 0.000027
9	41.37	0.00588 ± 0.00019	28	171	0.000929 ± 0.000025
10	45.95	0.00515 ± 0.00011	29	183.84	0.000826 ± 0.000026
11	50.58	0.00478 ± 0.0001	30	193.06	0.000814 ± 0.000025
12	55.16	0.0044 ± 0.00007	31	204.53	0.000784 ± 0.00002
13	62.05	0.0036 ± 0.00005	32	216.06	0.000713 ± 0.00002
14	68.95	0.00311 ± 0.00005	33	227.53	0.000764 ± 0.000018
15	75.84	0.00265 ± 0.00005	34	239	0.000627 ± 0.000019
16	82.74	0.00255 ± 0.00005	35	252.79	0.000628 ± 0.000015
17	88.25	0.00218 ± 0.00005	36	266.58	0.000624 ± 0.000009
18	96.53	0.00211 ± 0.00004	36	282.69	0.000919 ± 0.000008
19	103.42	0.00198 ± 0.00004			

Table A.1.: Density for the Virgo intracluster medium. Determined from deprojected ring data, separately for each shell.

Chandra data for the ICM electron density

$r(kpc)$	$n_e(cm^{-3})$	Δn_e	$r(kpc)$	$n_e(cm^{-3})$	Δn_e
0.115209	6.207776×10^{-1}	5.440981×10^{-2}	3.725097	6.510538×10^{-2}	5.839077×10^{-3}
0.192015	3.053082×10^{-1}	3.803621×10^{-2}	3.801903	7.203775×10^{-2}	4.626846×10^{-3}
0.268821	2.290631×10^{-1}	2.895689×10^{-2}	3.936314	5.708401×10^{-2}	2.256207×10^{-3}
0.345628	1.471540×10^{-1}	4.899842×10^{-2}	4.128329	4.969896×10^{-2}	2.735874×10^{-3}
0.422434	4.518539×10^{-2}	5.876067×10^{-2}	4.320344	4.953741×10^{-2}	2.220608×10^{-3}
0.499240	1.798615×10^{-1}	3.508150×10^{-2}	4.512360	4.462937×10^{-2}	2.526164×10^{-3}
0.576046	1.658334×10^{-1}	2.071634×10^{-2}	4.704375	4.728635×10^{-2}	2.411406×10^{-3}
0.652852	1.434284×10^{-1}	2.027164×10^{-2}	4.896390	4.318471×10^{-2}	2.272209×10^{-3}
0.729658	1.327213×10^{-1}	1.919180×10^{-2}	5.088406	3.751237×10^{-2}	2.427290×10^{-3}
0.806464	1.375711×10^{-1}	1.420680×10^{-2}	5.280421	4.693383×10^{-2}	2.084298×10^{-3}
0.883270	1.608704×10^{-1}	1.121156×10^{-2}	5.472436	3.970174×10^{-2}	2.035424×10^{-3}
0.960077	1.719347×10^{-1}	9.810708×10^{-3}	5.664452	3.842201×10^{-2}	2.166642×10^{-3}
1.036883	1.423202×10^{-1}	8.615950×10^{-3}	5.856467	3.788025×10^{-2}	2.038717×10^{-3}
1.113689	1.437331×10^{-1}	9.200014×10^{-3}	6.048482	3.391618×10^{-2}	1.862087×10^{-3}
1.190495	1.377344×10^{-1}	1.083572×10^{-2}	6.240498	3.360760×10^{-2}	1.960160×10^{-3}
1.267301	1.222085×10^{-1}	1.122031×10^{-2}	6.432513	3.038453×10^{-2}	2.258035×10^{-3}
1.344107	1.151992×10^{-1}	1.129778×10^{-2}	6.624528	3.332620×10^{-2}	1.675217×10^{-3}
1.420913	9.537300×10^{-2}	1.274086×10^{-2}	6.816544	2.854969×10^{-2}	1.993840×10^{-3}
1.497719	1.212357×10^{-1}	9.071433×10^{-3}	7.008559	3.307439×10^{-2}	1.554303×10^{-3}
1.574525	6.746266×10^{-2}	1.515254×10^{-2}	7.200574	2.299182×10^{-2}	2.229687×10^{-3}
1.651332	1.258400×10^{-1}	9.483147×10^{-3}	7.392589	2.974493×10^{-2}	1.576944×10^{-3}
1.728138	1.188165×10^{-1}	1.001005×10^{-2}	7.584605	2.662334×10^{-2}	1.550753×10^{-3}
1.804944	9.865212×10^{-2}	1.256213×10^{-2}	7.872628	2.570831×10^{-2}	9.974299×10^{-4}
1.881750	1.246004×10^{-1}	8.559155×10^{-3}	8.256659	2.473356×10^{-2}	8.934370×10^{-4}
1.958556	1.020257×10^{-1}	1.014084×10^{-2}	8.640689	2.516745×10^{-2}	7.838181×10^{-4}
2.035362	1.165679×10^{-1}	8.995564×10^{-3}	9.024719	2.389777×10^{-2}	8.459191×10^{-4}
2.112168	9.582048×10^{-2}	1.087496×10^{-2}	9.408750	2.310414×10^{-2}	7.606030×10^{-4}
2.188974	9.468200×10^{-2}	9.745320×10^{-3}	9.792781	2.526924×10^{-2}	6.586408×10^{-4}
2.265781	1.090871×10^{-1}	8.271703×10^{-3}	10.176811	2.142878×10^{-2}	8.152542×10^{-4}
2.342587	1.080226×10^{-1}	7.224756×10^{-3}	10.560842	2.392438×10^{-2}	6.844361×10^{-4}
2.419393	9.625605×10^{-2}	7.537802×10^{-3}	10.944873	2.061819×10^{-2}	8.782246×10^{-4}
2.496199	8.288545×10^{-2}	7.622845×10^{-3}	11.328903	2.058295×10^{-2}	8.563302×10^{-4}
2.573005	9.894732×10^{-2}	6.109593×10^{-3}	11.712934	2.076002×10^{-2}	6.941638×10^{-4}
2.649811	9.377372×10^{-2}	6.700545×10^{-3}	12.096964	2.030060×10^{-2}	7.049344×10^{-4}
2.726617	8.500989×10^{-2}	7.552563×10^{-3}	12.480995	1.962356×10^{-2}	7.351975×10^{-4}
2.803423	8.678568×10^{-2}	6.991512×10^{-3}	12.865026	1.919081×10^{-2}	7.380284×10^{-4}
2.880230	9.146296×10^{-2}	5.446229×10^{-3}	13.249056	1.844244×10^{-2}	7.088344×10^{-4}
2.957036	8.233752×10^{-2}	6.630178×10^{-3}	13.633087	1.858012×10^{-2}	6.357814×10^{-4}
3.033842	7.792548×10^{-2}	6.587046×10^{-3}	14.017118	1.798358×10^{-2}	6.498974×10^{-4}
3.110648	7.688681×10^{-2}	6.347487×10^{-3}	14.401148	1.785794×10^{-2}	5.960661×10^{-4}
3.187454	7.698260×10^{-2}	6.615524×10^{-3}	14.785178	1.901739×10^{-2}	5.735681×10^{-4}
3.257161	8.150671×10^{-2}	5.843301×10^{-3}	15.169209	1.730554×10^{-2}	6.131883×10^{-4}
3.341066	6.975581×10^{-2}	6.736083×10^{-3}	15.553240	1.560916×10^{-2}	5.802891×10^{-4}
3.417872	7.351877×10^{-2}	5.886118×10^{-3}	16.513317	1.568659×10^{-2}	1.572851×10^{-4}
3.494678	6.020789×10^{-2}	7.198343×10^{-3}	18.241453	1.483967×10^{-2}	1.570939×10^{-4}
3.571485	7.320779×10^{-2}	5.608382×10^{-3}	20.161608	1.055147×10^{-2}	1.911250×10^{-4}
3.648291	6.295457×10^{-2}	6.116255×10^{-3}	22.081760	1.986676×10^{-2}	6.541907×10^{-5}

Table A.2.: Density for the Virgo intracluster medium. Chandra data.

B. Python notebooks

This code processes the X-ray data, initialzes the photon propagation modules, visualizes the ICMF and calculates the rotationmeasure to constrain the ICMF model using the GammaALPs package

In [ ]:

```
# import python modules

from gammaALPs.core import Source, ALP, ModuleList
from gammaALPs.base import environs, transfer
import numpy as np
import matplotlib.pyplot as plt
from matplotlib.patheffects import withStroke
from ebltable.tau_from_model import OptDepth
from astropy import constants as c
from scipy import optimize
```

In [ ]:

```
%matplotlib inline
```

In [ ]:

```
# import M87 electron density data

data_c = np.genfromtxt('deprojne_annuli352sum_subpsfnew.dat') # Chandra dat
data_r = np.genfromtxt('rosat_nel.txt') # Rosat data
```

In [ ]:

```
# x-value (R in kpc)
R_c=data_c[:,][1:,0]
R_r=data_r[:,][:,0]

# y-value (electron density in cm^-3)
n_el_c=data_c[:,][1:,4]
n_el_r=data_r[:,][:,1]

# y-error
sigma_c=data_c[:,][1:,5]
sigma_r=data_r[:,][:,2]

# combine data
R=np.concatenate((R_c,R_r), axis=None)
n_el=np.concatenate((n_el_c,n_el_r), axis=None)
sig_nel=np.concatenate((sigma_c,sigma_r), axis=None)
```

In [ ]:

```
sorted_indices = np.argsort(R)
n = n_el[sorted_indices]
sig = sig_nel[sorted_indices]
r = np.sort(R)
```

In [ ]:

```
# Sort out Outliers

n_new = np.delete(n, 4, axis=0)
r_new = np.delete(r, 4, axis=0)
sig_new = np.delete(sig, 4, axis=0)
n_new1 = np.delete(n_new, -1, axis=0)
r_new1 = np.delete(r_new, -1, axis=0)
sig_new1 = np.delete(sig_new, -1, axis=0)
n_new2 = np.delete(n_new1, 52, axis=0)
r_new2 = np.delete(r_new1, 52, axis=0)
sig_new2 = np.delete(sig_new1, 52, axis=0)
n_new3 = np.delete(n_new2, -33, axis=0)
r_new3 = np.delete(r_new2, -33, axis=0)
sig_new3 = np.delete(sig_new2, -33, axis=0)
```

In [ ]:

```
# Creating Fitting Function for Electron Density using Scipy Minimize

xFit = np.linspace(0.1,300,1000)

# fitting paramter are: r_core, r_core2, n0, n2, beta, beta2

x0 = [0.43829613, 0.43365725 ,1.14342585,1.28663634,0.44993495,0.45925254]

def func(r, p):
    r0 = (1+((r*p[0])**2))**p[4]
    r1 = (1+((r*p[1])**2))**p[5]
    f = ((p[2]/r0)+(p[3]/r1))
    return f

def objective(p, *args):
    obj = np.sum(((func(args[0], p) - args[1])**2.) / args[2]**2.)
    return obj


objective(x0, *(r_new3, n_new3, sig_new3))
```

In [ ]:

```
# choose a different set of initial values

x0_new = [1. / 0.1, 1. / 2., 0.2, 0.11, 0.4, 0.6]


sys = 0.
sys = 0.1

res = optimize.minimize(objective, x0_new,
                        args=(r_new3, n_new3, np.sqrt(sig_new3**2. + (sys *
                        options={'disp':True, 'maxiter': 5000}, method='Nel
```

In [ ]:

```
res
```

In [ ]:

```
# Electron Density M87 (measurement Data and Fit)

#plt.rcParams["figure.figsize"] = (10,5)
plt.errorbar(r_new3, n_new3, yerr=sig_new3, marker='.', ls='none')
plt.gca().set_xscale("log")
plt.gca().set_yscale("log")
plt.ylabel(r'electron density [$\frac{1}{cm^{-3}}$]', fontsize='large', wei
plt.xlabel('distance to M87 AGN  [$kpc$]', fontsize='large', fontweight='ro
plt.title("Virgo cluster electron density model", fontsize='large')
#legend = ax.legend(loc='upper center', shadow=True, fontsize='x-large')

r = np.logspace(-2, 4, 100)
plt.loglog(r, func(r, res.x), label='$n_{el}$ best fit')
plt.legend(loc='upper right', shadow=True, fontsize='medium')
#plt.savefig("nelvirgo.png", dpi = 150)
```

In [ ]:

```
# reduced chi2
res.fun / (n_new3.size - len(res.x))
```

In [ ]:

```
# initiate ALP mass and coupling strength
m, g = 1.,1.
alp = ALP(m,g)
```

In [ ]:

```
# M87
ngc4486 = Source(z = 0.00436, ra = '12h30m49.4s', dec = '+12d23m28s')
print (ngc4486.z)
print (ngc4486.ra, ngc4486.dec)
print (ngc4486.l, ngc4486.b)

# M84
ngc4374 = Source(z = 0.003392, ra = '12h25m3.7s', dec = '+12d53m13s')
print (ngc4374.z)
print (ngc4374.ra, ngc4374.dec)
print (ngc4374.l, ngc4374.b)
```

In [ ]:

```
r_87 = 16757 # redshift independent distance of M87 in kpc  - taken from ht
r_84 = 16966 # redshift independent distance of M84 in kpc  - taken from ht
r84test = r_84 - 50

x = np.sqrt(r_87**2 + r_84**2 - r_87*r_84*2*np.cos(1.5*np.pi/180)) # dista
y = r_84 - np.cos(1.5*np.pi/180)*r_87
h = np.cos(1.5*np.pi/180)*r_87
print('x =',x,'kpc')
```

In [ ]:

```
r84 = np.linspace(16966, 15966, 3576)
line84 = np.sqrt(r_87**2 + r84**2 - r_87*r84*2*np.cos(1.5*np.pi/180))
```

In [ ]:

```
# Visualize Distance Comparison between M87 and M84 (Distance to M87 Core F

m87 = np.linspace(16757., 15757., 3576) # distance to Earth (M87)
r_m87 = np.linspace(0., 1000., 3576) # distance to M87 center (M87)
fig, ax = plt.subplots()
ax.plot(r84, line84, label='distance M84')
ax.plot(m87, r_m87, label='distance M87')
ax.set_xlim(17000, 15757)
plt.ylabel('Distance to M87 Center [kpc]', fontsize='x-large')
plt.xlabel('Distance to Earth [kpc]', fontsize='x-large')
ax.set_title("Distance to Virgo Center for M87 and M84", fontsize='x-large'
legend = ax.legend(loc='upper center', shadow=True, fontsize='large')
#plt.savefig("distancem87_m84.png", dpi = 150)
#plt.show
```

In [ ]:

```
EGeV = np.logspace(2.,4.5,50)
```

In [ ]:

```
pin = np.diag((1.,1.,0.)) * 0.5
```

In [ ]:

```
# setup photon propagation modules for M87

m = ModuleList(alp, ngc4486, pin = pin, EGeV = EGeV)

# Cluster magnetic field up to 2 kpc from source
# turbulence scale calculated such that correlation length is 0.2 kpc

kH = 6800
m.add_propagation("ICMGaussTurb",
                  0, # position of module counted from the source.
                  nsim = 1, # number of random B-field realizations
                  B0 = 36.9, #31.6,  # rms of B field - taken from A New B
                  n0 = res.x[2] * 1e3 ,  # normalization of electron densit
                  n2 = res.x[3] * 1e3, # second normalization of electron
                  r_abell = 2., # Cluster up to 2 kpc from source
                  r_core = 1. / res.x[0],    # electron density parameter,
                  r_core2 = 1. / res.x[1], # electron density parameter, s
                  beta = res.x[4] / 1.5,   # electron density parameter, see
                  beta2= res.x[5] / 1.5, # electron density parameter, see
                  eta = 0.44, #0.5, # scaling of B-field with electron dens
                  kL = 0.42, # maximum turbulence scale in kpc^-1, taken f
                  kH = 6800,  # minimum turbulence scale, taken from XMAGN
                  q = -2.9, # turbulence spectral index, taken from XMAGNE
                  seed=None, # random seed for reproducibility, set to None
                  thinning = 10
                 )


# Cluster magnetic field beginning from 2 kpc away from source up to the v

kH = 12.
m.add_propagation("ICMGaussTurb",
                  1, # position of module counted from the source.
                  nsim = 1, # number of random B-field realizations
                  B0 = 36.9, # 31.6 # rms of B field - taken from A New Bo
                  n0 = res.x[2]*1e3,  # normalization of electron density
                  n2 = res.x[3] * 1e3, # second normalization of electron
                  rbounds = np.arange(2., 1000., 1. / kH), # extension of t
                  r_core = 1. / res.x[0],    # electron density parameter,
                  r_core2 = 1. / res.x[1], # electron density parameter, s
                  beta = res.x[4] / 1.5,   # electron density parameter, see
                  beta2= res.x[5] / 1.5, # electron density parameter, see
                  eta = 0.44,  #0.5, # scaling of B-field with electron de
                  kL = 0.42, # maximum turbulence scale in kpc^-1, taken f
                  kH = 12,  # minimum turbulence scale, taken from XMAGNET
                  q = -2.5, # turbulence spectral index, taken from A New
                  seed=None # random seed for reproducibility, set to None
                 )

m.modules[1].B *= (m.modules[0].B[-1] / m.modules[1].B[0])

# Cluster magnetic field for M84 (only needed for simulation of rotation m


m84 = ModuleList(alp, ngc4374, pin = pin, EGeV = EGeV)

m84.add_propagation("ICMGaussTurb",
                  0, # position of module counted from the source.
                  nsim = 1, # number of random B-field realizations
                  B0 = 36.9,  # rms of B field - taken from A New Bound on
                  n0 = res.x[2]*1e3,  # normalization of electron density
                  n2 = res.x[3] * 1e3, # second normalization of electron
```

```
                  kH = 12,  # minimum turbulence scale, taken from XMAGNETI
                  q = -2.5, # turbulence spectral index, taken from A New E
                  seed=None # random seed for reproducability, set to None
                 )




#m.add_propagation("EBL",2, model = 'dominguez') # EBL dominguez model (not
m.add_propagation("EBL",2, model = 'finke') # EBL attenuation comes second,
m.add_propagation("GMF",3, model = 'jansson12', model_sum = 'ASS') # final
```

In [ ]:

```
# selection of ALP parameter

m_list = np.logspace(1.5, 3., 4)
g_list = np.logspace(-1, 1, 5)
```

In [ ]:

```
# calculate photon survival probability for specific ALP parameter

m.alp.m = m_list[2]
m.alp.g = g_list[1]

px,py,pa = m.run(multiprocess=2)

print ("ALP mass =", m.alp.m, "ALP coupling =", m.alp.g)


pgg = px + py # the total photon survival probability

#print (pgg.shape)
#print (np.min(np.median(pgg, axis = 0)))
#print (np.min(np.max(pgg, axis = 0)))
effect = dict(path_effects=[withStroke(foreground="w", linewidth=2)])

#for p in pgg: # plot all realizations

plt.semilogx(m.EGeV, pgg.flatten())

plt.xlabel('Energy $(GeV)$',fontsize='large', fontweight='demibold',fontsty
plt.ylabel('Photon survival probability', fontsize='large',fontweight='demi
#plt.legend(loc = 0, fontsize = 'medium')

plt.annotate(r'$m_a = {0:.1f}\,\mathrm{{neV}}, g_{{a\gamma}} = {1:.1f} \tim
             xy = (0.95,0.1), size = 'x-large', xycoords = 'axes fraction',

plt.gca().set_xscale('log')
plt.gca().set_yscale('log')
plt.xticks(fontweight='demibold')
plt.yticks(fontweight='demibold')
plt.subplots_adjust(left = 0.2)
#plt.savefig("pggm3g0.png", dpi = 150)
```

In [ ]:

```
#np.save('pgg5_0m150run10.npy', pgg)
```

In [ ]:

```
# Compare M87 and M84 B Field
plt.figure(figsize=(10, 4))
plt.semilogx(m.modules[1].r, m.modules[1].B, label="l.o.s. to M87", lw=1)
plt.semilogx(m84.modules[0].r, m84.modules[0].B,ls='-', lw=1, label="l.o.s.
plt.legend()
plt.ylabel('$B$ field ($\mu G$)', fontsize='large')
plt.xlabel('distance to M87 AGN $r$ (kpc)', fontsize='large')
plt.title ('ICMF along line of sight to M87 (outer regime) and M84')
plt.savefig("BM87M84.png", dpi = 150)
```

In [ ]:

```
# components of inner ICMF transversal to the propagation direction

plt.plot(m.modules[0].r,m.modules[0].B * np.sin(m.modules[0].psi),
         lw=1)
plt.plot(m.modules[0].r,m.modules[0].B * np.cos(m.modules[0].psi),
         lw=1, ls = '--')
plt.ylabel('$B$ field ($\mu G$)', fontsize='medium', fontweight='roman', fo
plt.xlabel('distance to M87 AGN $r$ $(kpc)$', fontsize='medium', fontweight
plt.title ('components of inner ICMF transv. to the propagation direction',
plt.savefig("Binnercomp.png", dpi = 150)
plt.show
```

In [ ]:

```
# electron density of inner 2kpc

plt.loglog(m.modules[0].r,m.modules[0].nel * 1e-3)
plt.ylabel('$electron$ $density$ ($cm^{-3}$)', fontsize='medium', fontweigh
plt.xlabel('distance to M87 AGN $r$ $(kpc)$', fontsize='medium', fontweight
plt.title ('$n_{el}$ of the inner region $(r < 2kpc)$', fontsize='large', f
plt.savefig("nelinner.png", dpi = 150)
plt.show
```

In [ ]:

```
# components of outer ICMF transversal to the propagation direction

plt.plot(m.modules[1].r,m.modules[1].B * np.sin(m.modules[1].psi),
         lw=1)
plt.plot(m.modules[1].r,m.modules[1].B * np.cos(m.modules[1].psi),
         lw=1, ls = '--')
plt.ylabel('$B$ field ($\mu$G)', fontsize='medium', fontweight='roman', for
plt.xlabel('distance to M87 AGN $r$ $(kpc)$', fontsize='medium', fontweight
plt.title ('components of outer ICMF transv. to the propagation direction',
plt.savefig("Boutercomp.png", dpi = 150)
plt.show
```

In [ ]:

```
# electron density of region 2kpc < r < 1000kpc

plt.loglog(m.modules[1].r,m.modules[1].nel * 1e-3, color = 'orange')
plt.ylabel('$electron$ $density$ ($cm^{-3}$)', fontsize='medium', fontweigh
plt.xlabel('distance to M87 AGN $r$ $(kpc)$', fontsize='medium', fontweight
plt.title ('$n_{el}$ of the outer region $(2kpc < r < 1000kpc)$', fontsize=
plt.savefig("nelouter.png", dpi = 150)
plt.show
```

In [ ]:

```
# Visualize both B field regimes of M87

plt.figure(figsize=(10, 4))
plt.semilogx(m.modules[0].r,m.modules[0].B, label="inner regime", lw=1)
#plt.semilogx(r, B, ls='--')
plt.plot(m.modules[1].r, m.modules[1].B * (m.modules[0].B[-1] / m.modules[1
#plt.semilogx(m.modules[1].r, m.modules[1].B, label="outer regime", ls='--
plt.legend()
#plt.ylabel('$B$ ($\mu$G)')
#plt.xlabel('$r$ (kpc)')
plt.xlabel('distance to central AGN $r$ $(kpc)$', fontsize='large')
plt.ylabel('$B$ ($\mu G$)', fontsize='large')
plt.title ('M87 ICMF both regimes')
plt.savefig("B0B1M87.png", dpi = 150)
```

In [ ]:

```
# Calculate RM Mean and Variation for M87 l.o.s.

var_eta = np.arange(0.1, 0.7, 0.1)
var_B0 = np.arange(14., 62., 4)


nsim = 500  # start with 100 for testing, increase to a 1000 later

rm1 = np.zeros((len(var_eta), len(var_B0), nsim))  # 3D array with shape: r
rm2 = np.zeros((len(var_eta), len(var_B0), nsim))

var = np.zeros((len(var_eta), len(var_B0)))
mean = np.zeros((len(var_eta), len(var_B0)))

for i, etavar in enumerate(var_eta):
    for j, B0var in enumerate(var_B0):
        print (i,j)
        m = ModuleList(alp, ngc4486, pin = pin, EGeV = EGeV)

        kH = 6800.
        m.add_propagation("ICMGaussTurb",
                  0, # position of module counted from the source.
                  nsim = 1, # number of random B-field realizations
                  B0 = B0var,  # rms of B field - taken from A New Bound on
                  n0 = res.x[2]*1e3 ,  # normalization of electron density
                  n2 = res.x[3] * 1e3, # second normalization of electron d
                  r_abell = 2., # extension of the cluster
                  r_core = 1. / res.x[0],   # electron density parameter, s
                  r_core2 = 1. / res.x[1], # electron density parameter, se
                  beta = res.x[4] / 1.5,  # electron density parameter, see
                  beta2= res.x[5] / 1.5, # electron density parameter, see
                  eta = etavar, # scaling of B-field with electron denstiy
                  kL = 0.42, # maximum turbulence scale in kpc^-1, taken fr
                  kH = 6800,  # minimum turbulence scale, taken from XMAGNE
                  q = -2.9, # turbulence spectral index, taken from XMAGNET
                  seed=None, # random seed for reproducability, set to None
                  thinning = 10
                 )
        kH = 12.
        m.add_propagation("ICMGaussTurb",
                  1, # position of module counted from the source.
                  nsim = 1, # number of random B-field realizations
                  B0 = B0var,  # rms of B field - taken from A New Bound on
                  n0 = res.x[2]*1e3,  # normalization of electron density
                  n2 = res.x[3] * 1e3, # second normalization of electron d
                  rbounds = np.arange(2., 1000., 1. / kH), # extension of t
                  r_core = 1. / res.x[0],   # electron density parameter, s
                  r_core2 = 1. / res.x[1], # electron density parameter, se
                  beta = res.x[4] / 1.5,  # electron density parameter, see
                  beta2= res.x[5] / 1.5, # electron density parameter, see
                  eta = etavar, # scaling of B-field with electron denstiy
                  kL = 0.42, # maximum turbulence scale in kpc^-1, taken fr
                  kH = 12,  # minimum turbulence scale, taken from XMAGNETI
                  q = -2.5, # turbulence spectral index, taken from XMAGNET
                  seed=None # random seed for reproducability, set to None
                 )

        m.modules[1].B *= (m.modules[0].B[-1] / m.modules[1].B[0])
        Bscale0 = m.modules[0].nel_model.Bscale(m.modules[0].r)
        Bscale1 = m.modules[1].nel_model.Bscale(m.modules[1].r)
```

```
                                                               n_el=m.modul
                                                               Bscale=Bscal
                                                               nsim=nsim)


        rm = rm1[i, j]+rm2[i, j]

        var[i, j] = np.var(rm)
        mean[i, j] = np.mean(rm)

        del m
```

In [ ]:

```
# Calculate RM Mean and Variation for M84 l.o.s.

var_eta = np.arange(0.1, 0.7, 0.1)
var_B0 = np.arange(14., 62., 4)

nsim = 500  # start with 100 for testing, increase to a 1000 later

rm84 = np.zeros((len(var_eta), len(var_B0), nsim))  # 3D array with shape:

var84 = np.zeros((len(var_eta), len(var_B0)))
mean84 = np.zeros((len(var_eta), len(var_B0)))

for i, etavar in enumerate(var_eta):
    for j, B0var in enumerate(var_B0):
        print (i,j)
        m84 = ModuleList(alp, ngc4374, pin = pin, EGeV = EGeV)

        m84.add_propagation("ICMGaussTurb",
                  0, # position of module counted from the source.
                  nsim = 50, # number of random B-field realizations
                  B0 = B0var,  # rms of B field - taken from A New Bound or
                  n0 = res.x[2]*1e3,  # normalization of electron density
                  n2 = res.x[3] * 1e3, # second normalization of electron
                  rbounds = line84, # extension of the cluster
                  r_core = 1. / res.x[0],   # electron density parameter, s
                  r_core2 = 1. / res.x[1], # electron density parameter, se
                  beta = res.x[4] / 1.5,  # electron density parameter, see
                  beta2= res.x[5] / 1.5, # electron density parameter, see
                  eta = etavar, # scaling of B-field with electron denstiy
                  kL = 0.42, # maximum turbulence scale in kpc^-1, taken fr
                  kH = 12,  # minimum turbulence scale, taken from XMAGNETI
                  q = -2.5, # turbulence spectral index, taken from XMAGNET
                  seed=None # random seed for reproducibility, set to None
                 )


        m84.modules[0].Bfield_model.seed = None
        Bscale = m84.modules[0].nel_model.Bscale(m84.modules[0].r)
        rm84 = m84.modules[0].Bfield_model.rotation_measure(m84.modules[0].
                                                               n_el=m84.mo
                                                               Bscale=Bscal
                                                               nsim=nsim)
```

In [ ]:

```
# plot sigma(RM) vor M87

fig, ax = plt.subplots()
bb, ee = np.meshgrid(var_B0, var_eta, indexing='ij')
print(bb.shape, ee.shape, np.sqrt(var).shape)
im = ax.pcolormesh(bb, ee, np.sqrt(var).T, cmap="coolwarm")
plt.colorbar(im)
```

In [ ]:

```
# plot sigma(RM) vor M84

fig, ax = plt.subplots()
bb84, ee84 = np.meshgrid(var_B0, var_eta, indexing='ij')
print(bb84.shape, ee84.shape, np.sqrt(var84).shape)
im = ax.pcolormesh(bb84, ee84, np.sqrt(var84).T, cmap="coolwarm")
plt.colorbar(im)
```

In [ ]:

```
from scipy.interpolate import RectBivariateSpline
```

In [ ]:

```
# prepare finer grid

spl  = RectBivariateSpline(var_B0, var_eta, np.sqrt(var).T, kx=2, ky=2, s=0)
spl84 = RectBivariateSpline(var_B0, var_eta, np.sqrt(var84).T, kx=2, ky=2,
```

In [ ]:

```
plot_eta = np.arange(var_eta.min(), var_eta.max(), 0.01)
plot_B = np.arange(var_B0.min(), var_B0.max(), 0.5)

print (plot_eta.shape, plot_B.shape)

bb, ee = np.meshgrid(plot_B, plot_eta, indexing='ij')
vv = spl(plot_B, plot_eta)

print (bb.shape, ee.shape, vv.shape)
```

In [ ]:

```
# RM contour lines for M87

fig, ax = plt.subplots()
im = ax.pcolormesh(bb, ee, vv, cmap="coolwarm")
plt.colorbar(im)
cs = ax.contour(bb, ee, vv, levels=np.arange(1000.,3500.,500), colors='k',
ax.clabel(cs, fmt="%.0f")
ax.set_xlabel("$B$ ($\mu$G)")
ax.set_ylabel("$\eta$")
#ax.set_ylim(0.1,0.7)
#ax.set_xlim(14.,62,)
#plt.savefig("m87_RMcomplete.png", dpi = 150)
```

In [ ]:

```
plot_eta84 = np.arange(var_eta.min(), var_eta.max(), 0.01)
plot_B84 = np.arange(var_B0.min(), var_B0.max(), 0.5)

print (plot_eta84.shape, plot_B84.shape)

bb84, ee84 = np.meshgrid(plot_B84, plot_eta84, indexing='ij')
vv84 = spl84(plot_B84, plot_eta84)

print (bb84.shape, ee84.shape, vv84.shape)
```

In [ ]:

```
# RM contour lines for M84

fig, ax = plt.subplots()
im = ax.pcolormesh(bb84, ee84, vv84, cmap="coolwarm")
plt.colorbar(im)
cs = ax.contour(bb84, ee84, vv84, levels=np.arange(0.,16.,2), colors='k', l
ax.clabel(cs, fmt="%.0f")
ax.set_xlabel("$B$ ($\mu$G)", fontsize='xx-large')
ax.set_ylabel("$\eta$", fontsize='xx-large')
ax.set_title('RM measure for M84 at minimum distance to central AGN', fonts
#ax.set_ylim(0.1,0.6)
#ax.set_xlim(23.,var_B0.max())
#plt.savefig("m84_RMminimumdist.png", dpi = 150)
```

In [ ]:

```
# combining contour lines of M87 and M84

fig, ax = plt.subplots()
im = ax.pcolormesh(bb, ee, vv, cmap="coolwarm")
plt.colorbar(im)
cs = ax.contour(bb, ee, vv, levels=np.arange(1000.,3500.,500), colors='k',
cs1 = ax.contour(bb84, ee84, vv84, levels=np.arange(0.,15.,2.5), colors='k'
ax.clabel(cs, fmt="%.0f")
ax.clabel(cs1, fmt="%.0f")
ax.set_xlabel("$B$ ($\mu$G)")
ax.set_ylabel("$\eta$")
ax.set_ylim(0.2,0.6)
#ax.set_xlim(23.,var_B0.max())
#plt.savefig("m8784RMcomplete.png", dpi = 150)
```

In [ ]:

Here the photon survival probability for the selected ALP masses and couplings are calculated für 500 realizations each

In [ ]:

```
from gammaALPs.core import Source, ALP, ModuleList
from gammaALPs.base import environs, transfer
import numpy as np
import matplotlib.pyplot as plt
from matplotlib.patheffects import withStroke
from ebltable.tau_from_model import OptDepth
from astropy import constants as c
from scipy import optimize
```

In [ ]:

```
import astropy
```

In [ ]:

```
from pathlib import Path
import astropy.units as u
from astropy.coordinates import SkyCoord, Angle
```

In [ ]:

```
%matplotlib inline
```

In [ ]:

```
m, g = 1.,1.
alp = ALP(m,g)
```

In [ ]:

```
# M87  -  g
ngc4486 = Source(z = 0.00436, ra = '12h30m49.4s', dec = '+12d23m28s')
print (ngc4486.z)
print (ngc4486.ra, ngc4486.dec)
print (ngc4486.l, ngc4486.b)
```

In [ ]:

```
EGeV = np.logspace(2.,4.7,200) # energy bins
energy_range = [0.1, 50] * u.TeV
energy = EGeV * u.GeV
```

In [ ]:

```
pin = np.diag((1.,1.,0.)) * 0.5
```

In [ ]:

```
# Calculate photon survival probability (pgg) für a selection of ALP masses


m_list = np.logspace(1.5, 3., 4)
g_list = np.logspace(-1, 1, 5)
real = np.arange(500) # number of magnetic field realizations

m_dim = []

for mm in m_list:

    print(mm)

    g_dim = []

    for gg in g_list:

        B_dim = []

        for i in real:



            # initialize intra cluster magnetic field
            # here: Virgo Cluster - electron density fitted using a "double
            # see Churazov et al. 2003, Eq. 4, gaussian turbulence assumed

            m = ModuleList(alp, ngc4486, pin = pin, EGeV = EGeV)

            m.alp.g = gg
            m.alp.m = mm


            # cluster magnetic field up to 2kpc away from source (M87 AGN):

            kH = 6800
            m.add_propagation("ICMGaussTurb",
                  0, # position of module counted from the source.
                  nsim = 1, # number of random B-field realizations
                  B0 = 36.9, # rms of B field - selected from rotation meas
                  n0 = 1.23725923137820 * 1e3 ,  # normalization of electro
                  n2 = 0.16415354238379992 * 1e3, # second normalization of
                  r_abell = 2., # Cluster up to 2 kpc from source
                  r_core = 1. / 6.505152014385795,   # electron density par
                  r_core2 = 1. / 0.5824511272785253, # electron density par
                  beta = 2.2475041074705784 / 1.5,  # electron density para
                  beta2= 0.5525452714980288 / 1.5, # electron density param
                  eta = 0.44, # scaling of B-field with electron denstiy, s
                  kL = 0.42, # maximum turbulence scale in kpc^-1, chosen s
                  kH = 6800,  # minimum turbulence scale, chosen such that
                  q = -2.9, # turbulence spectral index, taken from XMAGNET
                  seed=i, # random seed for reproducability, set to None fo
                  thinning = 10
                 )


            # cluster magnetic field beginning from 2kpc away from source u

            kH = 12.
            m.add_propagation("ICMGaussTurb",
                  1, # position of module counted from the source.
                  nsim = 1, # number of random B-field realizations
```

```
                  beta2= 0.5525452714980288 / 1.5, # electron density param
                  eta = 0.44, # scaling of B-field with electron denstiy, s
                  kL = 0.42, # maximum turbulence scale in kpc^-1, taken fr
                  kH = 12,  # minimum turbulence scale, taken from XMAGNETI
                  q = -2.5, # turbulence spectral index, taken from A New E
                  seed=i # random seed for reproducibility, set to None for
                 )

            m.modules[1].B *= (m.modules[0].B[-1] / m.modules[1].B[0])

            m.add_propagation("EBL",2, model = 'finke') # EBL attenuation c

            # galactic magnetic field:

            m.add_propagation("GMF",3, model = 'jansson12', model_sum = 'AS
            px,py,pa = m.run(multiprocess=2)
            pgg = px + py

            B_dim.append(pgg)
            del m

        g_dim.append(B_dim)

    m_dim.append(g_dim)

pgg_array = np.array(m_dim)
```

In [ ]:

```
#np.save("pgg_array.npy", pgg_array)
#np.save("pgg4m4g1000b100e.npy", pgg_array)
#np.save("pgg4m5g500b200e.npy", pgg_array)
```

This code processes the H.E.S.S. data and calculates all the fits (with and without assumed photon - ALP conversion). Only the logParabola model code is shown

In [ ]:

```python
from gammaALPs.core import Source, ALP, ModuleList
from gammaALPs.base import environs, transfer
import numpy as np
import matplotlib.pyplot as plt
from matplotlib.patheffects import withStroke
from ebltable.tau_from_model import OptDepth
from astropy import constants as c
from scipy import optimize
```

In [ ]:

```python
import astropy
import gammapy
```

In [ ]:

```python
from iminuit import Minuit

from pathlib import Path
import astropy.units as u
from astropy.coordinates import SkyCoord, Angle
from regions import CircleSkyRegion
from gammapy.maps import Map, MapAxis
from gammapy.modeling import Fit
from gammapy.data import DataStore
from gammapy.datasets import (
    Datasets,
    SpectrumDataset,
    SpectrumDatasetOnOff,
    FluxPointsDataset,
)
from gammapy.modeling.models import (
    PowerLawSpectralModel,
    create_crab_spectral_model,
    SkyModel,
)
from gammapy.makers import (
    SafeMaskMaker,
    SpectrumDatasetMaker,
    ReflectedRegionsBackgroundMaker,
)
from gammapy.estimators import FluxPointsEstimator
from gammapy.visualization import plot_spectrum_datasets_off_regions


from gammapy.modeling.models import (
    Models,
    PowerLawSpectralModel,
    LogParabolaSpectralModel,
    PiecewiseNormSpectralModel,
    SkyModel,
    TemplateSpectralModel,
)
```

In [ ]:

```python
%matplotlib inline
```

In [ ]:

```python
m, g = 1.,1.
alp = ALP(m,g)
```

In [ ]:

```
EGeV = np.logspace(2.,4.7,200)
energy_range = [0.1, 50] * u.TeV
energy = EGeV * u.GeV
```

In [ ]:

```
# read in datasets (here: H.E.S.S. data)

datasets = Datasets.read(filename="/Users/TinePhill/m87dataset1/com_rl_data
                         filename_models = "/Users/TinePhill/m87dataset1/co


dataset_stacked = Datasets(datasets).stack_reduce()
```

In [ ]:

```
# reduce fitting energy range

dataset_stacked.mask_safe.data[-1] = False
dataset_stacked.mask_safe.data[-2] = False
dataset_stacked.mask_safe.data[-3] = False
dataset_stacked.mask_safe.data[-4] = False
dataset_stacked.mask_safe.data[-5] = False
dataset_stacked.mask_safe.data[-6] = False
dataset_stacked.mask_safe.data[-7] = False
dataset_stacked.mask_safe.data[-8] = False
dataset_stacked.mask_safe.data[-9] = False
dataset_stacked.mask_safe.data[-10] = False
dataset_stacked.mask_safe.data[-11] = False
dataset_stacked.mask_safe.data[-12] = False
dataset_stacked.mask_safe.data[-13] = False
dataset_stacked.mask_safe.data[-14] = False
dataset_stacked.mask_safe.data[-15] = False
dataset_stacked.mask_safe.data[-16] = False
dataset_stacked.mask_safe.data[-17] = False
```

In [ ]:

```
# import photon survival probabilities and EBL attenuation

pgg_array4 = np.load('pgg_arrayEBL.npy',  allow_pickle=True)
atten = np.load('atten.npy',  allow_pickle=True)
```

In [ ]:

```
e_min, e_max = 0.5, 30
energy_edges = np.logspace(np.log10(e_min), np.log10(e_max), 11) * u.TeV
```

In [ ]:

```
# fit data using a logparabola spectral model
# template model to account for EBL attenuation
# multiplication of LogParabola model with template model includes EBL atte
# to the spectral model

template = TemplateSpectralModel(energy=EGeV * u.GeV, values = atten)
new_model = template * LogParabolaSpectralModel(
                                amplitude=5.1497e-13 * u.Unit("cm-2 s-1 TeV
                                reference=1 * u.TeV, alpha=2.2206e+00, beta

model = SkyModel(spectral_model=new_model)


for dataset in datasets:
    dataset.models = model
```

In [ ]:

```
# fitting the model

dataset_stacked.models = model
stacked_fit = Fit([dataset_stacked])
result_stackedLP = stacked_fit.run()

# make a copy to compare later
model_best_stackedLP = model.copy()
```

In [ ]:

```
# powerlaw model best fit parameter (take these as start value for compound

model_best_stackedLP.parameters.to_table()
```

In [ ]:

```
# likelihood value for powerlaw model

result_stackedLP.total_stat
```

In [ ]:

```
# calculate flux points

fpe = FluxPointsEstimator(energy_edges=energy_edges, source=0)
flux_points = fpe.run(datasets=dataset_stacked)
```

In [ ]:

```
# fitting H.E.S.S dataset with LogParabola * template (photon survival prob


m_dim_ampLP = []
m_dim_dampLP = []
m_dim_statLP = []
m_dim_a = []
m_dim_da = []
m_dim_b = []
m_dim_db = []

for i in range(len(pgg_array4)):
    print(i)
    g_dim_ampLP = []
    g_dim_dampLP = []
    g_dim_statLP = []
    g_dim_a = []
    g_dim_da = []
    g_dim_b = []
    g_dim_db = []
    for j in range(len(pgg_array4[i])):
        print(j)
        B_dim_ampLP = []
        B_dim_dampLP = []
        B_dim_statLP = []
        B_dim_a = []
        B_dim_da = []
        B_dim_b = []
        B_dim_db = []

        for k in range(len(pgg_array4[i][j])):

            template = TemplateSpectralModel(energy=EGeV * u.GeV, values =
            new_model = template * LogParabolaSpectralModel(
                                amplitude=5.1497e-13 * u.Unit("cm-2 s-1 TeV
                                reference=1 * u.TeV, alpha=2.2206e+00, beta

            new_model.parameters['alpha'].min=1.0
            new_model.parameters['alpha'].max=5.5
            new_model.parameters['beta'].min=0.05e-01
            new_model.parameters['beta'].max=8.5e-01
            new_model.parameters['amplitude'].min=2.5e-13 #* u.Unit("cm-2 s
            new_model.parameters['amplitude'].max=15.5e-13 #* u.Unit("cm-2
            spectral_model = new_model
            model = SkyModel(spectral_model=spectral_model)
            dataset_stacked.models = model
            stacked_fit = Fit([dataset_stacked])
            result_stackedLP = stacked_fit.run()

            statLP = result_stackedLP.total_stat
            ampLP = result_stackedLP.parameters.to_table()[0][1]
            dampLP = result_stackedLP.parameters.to_table()[0][-1]
            a = result_stackedLP.parameters.to_table()[2][1]
            da = result_stackedLP.parameters.to_table()[2][-1]
            b = result_stackedLP.parameters.to_table()[3][1]
            db = result_stackedLP.parameters.to_table()[3][-1]


            B_dim_statLP.append(statLP)
            B_dim_ampLP.append(ampLP)
            B_dim_dampLP.append(dampLP)
            B_dim_a.append(a)
```

```
        g_dim_a.append(B_dim_a)
        g_dim_da.append(B_dim_da)
        g_dim_b.append(B_dim_b)
        g_dim_db.append(B_dim_db)

    m_dim_statLP.append(g_dim_statLP)
    m_dim_ampLP.append(g_dim_ampLP)
    m_dim_dampLP.append(g_dim_dampLP)
    m_dim_a.append(g_dim_a)
    m_dim_da.append(g_dim_da)
    m_dim_b.append(g_dim_b)
    m_dim_db.append(g_dim_db)



total_statLP = np.array(m_dim_statLP)
amplitudeLP = np.array(m_dim_ampLP)
amplitude_errorLP = np.array(m_dim_dampLP)
alpha = np.array(m_dim_a)
alpha_error = np.array(m_dim_da)
beta = np.array(m_dim_b)
beta_error = np.array(m_dim_db)
```

In [ ]:

```
# best fit alpha histogramm (E bins < 20TeV) + EBL

a = alpha.flatten()
n, bins, patches = plt.hist(a, bins = 50, density = True, facecolor='b', al
plt.xlabel(r'$ \alpha$', fontsize='x-large', fontweight='bold', fontstyle='
plt.ylabel('Density', fontsize='large', fontweight='demibold', fontstyle='
plt.axvline(x = 2.1922e+00, color = 'red', label = 'Model without ALPs')
#plt.axvline(x = 2.2559323828628957, color = 'purple', label = 'worst fit 
plt.title('Best fit alpha values', fontsize='large', fontweight='demibold',
plt.xticks(fontsize='large', fontweight='demibold', fontstyle='oblique')
plt.yticks(fontsize='large', fontweight='demibold', fontstyle='oblique')
plt.legend(loc = 'upper left', fontsize='large')
plt.xlim([a.min(), a.max()])
#plt.savefig("LPalphahist.png", dpi = 150)
```

In [ ]:

```
# best fit beta histogramm (E bins < 20TeV) + EBL

b = beta.flatten()
n, bins, patches = plt.hist(b, bins = 50, density = True, facecolor='b', al
plt.xlabel(r'$ \beta$', fontsize='x-large', fontweight='bold', fontstyle='
plt.ylabel('Density', fontsize='large', fontweight='demibold', fontstyle='
plt.axvline(x = 1.0507e-01      , color = 'red', label = 'Model without AL
#plt.axvline(x = 2.2559323828628957, color = 'purple', label = 'worst fit 
plt.title('Best fit beta values', fontsize='large', fontweight='demibold',
plt.xticks(fontsize='large', fontweight='demibold', fontstyle='oblique')
plt.yticks(fontsize='large', fontweight='demibold', fontstyle='oblique')
plt.legend(loc = 'upper right', fontsize='large')
plt.xlim([b.min(), b.max()])
#plt.savefig("LPbetahist.png", dpi = 150)
```

In [ ]:

```
# best fit amplitude histogramm (E bins < 20TeV) + EBL

amp = amplitudeLP.flatten()
n, bins, patches = plt.hist(amp, bins = 50, density = True, facecolor='b',
plt.xlabel(r'Amplitude $\phi_{0}$', fontsize='large', fontweight='bold', fc
plt.ylabel('Density', fontsize='large', fontweight='demibold', fontstyle='c
plt.axvline(x = 5.3483e-13, color = 'red', label = 'Model without ALPs')
#plt.axvline(x = 1.9141e-13, color = 'purple', label = 'worst fit with ALPs
plt.title('Best fit amplitude values', fontsize='large', fontweight='demibc
plt.xticks(fontsize='large', fontweight='demibold', fontstyle='oblique')
plt.yticks(fontsize='large', fontweight='demibold', fontstyle='oblique')
plt.xlim([amp.min(), amp.max()])
plt.legend(loc = 'upper right', fontsize='large')
#plt.savefig("LPamphist.png", dpi = 150)
```

In [ ]:

```
# best fit likelihood histogramm (E bins < 20TeV) + EBL

like = total_statLP.flatten()
n, bins, patches = plt.hist(like, bins = 50, density = True, facecolor='b',
plt.xlabel('Likelihood', fontsize='large', fontweight='bold', fontstyle='ob
plt.ylabel('Density', fontsize='large', fontweight='demibold', fontstyle='c
plt.axvline(x = 44.14, color = 'red', label = 'Model without ALPs')
#plt.axvline(x = 70.36510213906509, color = 'purple', label = 'worst fit wi
#plt.axvline(x = 40.835434362813544, color = 'darkgreen', label = 'best fit
plt.title('Best fit likelihood values', fontsize='large', fontweight='demib
plt.xticks(fontsize='large', fontweight='demibold', fontstyle='oblique')
plt.yticks(fontsize='large', fontweight='demibold', fontstyle='oblique')
plt.xlim([like.min(), like.max()])
plt.legend(loc = 'upper right', fontsize='large')
#plt.savefig("LPlikehist.png", dpi = 150)
```

In [ ]:

```
# new fit likelihood histogramm (E bins < 20TeV) + EBL

sig = like -  44.13978134135573
```

In [ ]:

```
n, bins, patches = plt.hist(sig, bins = 50, density = True, facecolor='b',
plt.xlabel(r'Teststatistic $TS$', fontsize='large', fontweight='bold', font
plt.ylabel('Density', fontsize='large', fontweight='demibold', fontstyle='c
plt.axvline(x = 0, color = 'red', label = 'Model without ALPs')
plt.axvline(x = sig.min(), color = 'orange', label = 'Best fit with ALPs')
plt.axvline(x = sig.max(), color = 'black', label = 'Worst fit with ALPs')
plt.title('Likelihood difference', fontsize='large', fontweight='demibold',
plt.xticks(fontsize='large', fontweight='demibold', fontstyle='oblique')
plt.yticks(fontsize='large', fontweight='demibold', fontstyle='oblique')
plt.legend(loc = 'upper right', fontsize='large')
#plt.xlim([35, 75])
#plt.ylim([0,550])
#plt.savefig("LPdifflikehist.png", dpi = 150)
```

In [ ]:

```
# sort likelihood values from worst to best

LHLP = np.sort(total_statLP)
```

In [ ]:

```
LHLP100 = LHLP[:,:,0] # 100% quantile
LHLP95 = LHLP[:,:,24]  # 95% quantile
LHLP50 = LHLP[:,:,249] # 50% quantile
LHLP00 = LHLP[:,:,499] # 0% quantile
```

In [ ]:

```
# find corresponding B field realization
indexLHLP = np.argsort(total_statLP)
```

In [ ]:

```
indexLHLP[0,3,24]
```

In [ ]:

```
amp100 = amplitudeLP[0,3,475]
amp95 = amplitudeLP[0,3,435]
amp50 = amplitudeLP[3,4,168]
amp00 = amplitudeLP[0,2,129]
```

In [ ]:

```
a100 = alpha[0,3,475]
a95 = alpha[0,3,435]
a50 = alpha[3,4,168]
a00 = alpha[0,2,129]
```

In [ ]:

```
b100 = beta[0,3,475]
b95 = beta[0,3,435]
b50 = beta[3,4,168]
b00 = beta[0,2,129]
```

In [ ]:

```
# test statistic of hypothesis test

m_list = np.logspace(1.5, 3., 5)
g_list = np.logspace(-1, 1, 6)

fig, ax = plt.subplots()
mm, gg = np.meshgrid(m_list, g_list, indexing='ij')
# print(bb.shape, ee.shape, np.sqrt(var).shape)
im = ax.pcolormesh(mm, gg, (LHLP95 - 44.14), cmap="coolwarm")
ax.set_xlabel(r"$m_{a}$ ($neV$)", fontsize='x-large', fontweight='demibold'
ax.set_ylabel(r"$g_{a\gamma}$ ($x\ 10^{-11}GeV^{-1}$)", fontsize='x-large',
ax.set_title(r"$\Delta$TS (logParabola model)", fontsize='large', fontweigh
plt.xticks(fontsize='large', fontweight='demibold', fontstyle='oblique')
plt.yticks(fontsize='large', fontweight='demibold', fontstyle='oblique')
plt.colorbar(im)
plt.xscale('log')
plt.yscale('log')
# plt.savefig("TS_LP.png",bbox_inches='tight', dpi = 150)
```

In [ ]:

```
# profile likelihood evaluation (95% quantile)

m_list = np.logspace(1.5, 3., 5)
g_list = np.logspace(-1, 1, 6)

fig, ax = plt.subplots()
mm, gg = np.meshgrid(m_list, g_list, indexing='ij')
# print(bb.shape, ee.shape, np.sqrt(var).shape)
im = ax.pcolormesh(mm, gg, (LHLP95), cmap="coolwarm")
ax.set_xlabel(r"$m_{a}$ ($neV$)", fontsize='x-large', fontweight='demibold'
ax.set_ylabel(r"$g_{a\gamma}$ ($x\ 10^{-11}GeV^{-1}$)", fontsize='x-large',
ax.set_title("TS (logParabola model)", fontsize='large', fontweight='demibo
plt.xticks(fontsize='large', fontweight='demibold', fontstyle='oblique')
plt.yticks(fontsize='large', fontweight='demibold', fontstyle='oblique')
plt.colorbar(im)
plt.xscale('log')
plt.yscale('log')
#plt.savefig("TS_LP.png", dpi = 150)
```

In [ ]:

```
# setup spektral model for selected B field realization

template = TemplateSpectralModel(energy=EGeV * u.GeV, values = pgg_array4[
new_model = template * LogParabolaSpectralModel(
                                          amplitude=amp95 * u.Unit("cm-2 s-
                                          reference=1 * u.TeV,
                                          alpha=a95,
                                          beta=b95)


spectral_model = new_model
model = SkyModel(spectral_model=spectral_model)
```

In [ ]:

```
# fitting spectral model with ALPs

dataset_stacked.models = model
stacked_fit = Fit([dataset_stacked])
result_stacked = stacked_fit.run()

# make a copy to compare later
model_best_stackedALPLP = model.copy()
```

In [ ]:

```
# plot spectral model with and without ALPs
# together with flux points

plot_kwargs = {
    "energy_range": [0.1, 30] * u.TeV,
    "energy_power": 2,
    "flux_unit": "erg-1 cm-2 s-1",
}



plt.figure(figsize=(8, 5))
flux_points.table["is_ul"] = flux_points.table["ts"] < 4
ax = flux_points.plot(
    energy_power=2, flux_unit="erg-1 cm-2 s-1", color="darkorange"
)
#flux_points.to_sed_type("e2dnde").plot_ts_profiles(ax=ax);
model_best_stackedLP.spectral_model.plot(
    **plot_kwargs, label="Model without ALPs"
)
model_best_stackedLP.spectral_model.plot_error(**plot_kwargs)

model_best_stackedALPLP.spectral_model.plot(
    **plot_kwargs, label="Model with ALPs (95% quantile)",
    color="black",
)
model_best_stackedALPLP.spectral_model.plot_error(**plot_kwargs)

plt.xticks(fontsize='large', fontweight='demibold', fontstyle='oblique')
plt.yticks(fontsize='large', fontweight='demibold', fontstyle='oblique')
plt.ylabel(r'$E^{2}\times Flux\ [\frac{erg}{cm^{2}s}]$',fontsize='x-large',
plt.xlabel('Energy $(TeV)$',fontsize='large', fontweight='demibold', fontst
plt.title("Fluxpoints / logParabola fit", fontsize='large', fontweight='dem

plt.legend()

plt.savefig("fluxpoints_ALPLP95.png", dpi=150)
```

In [ ]:

```
```

References

Abdalla, H., Abe, H., Acero, F., Acharyya, A., Adam, R., Agudo, I., … Živec, M. (2021, February). Sensitivity of the cherenkov telescope array for probing cosmology and fundamental physics with gamma-ray propagation. *Journal of Cosmology and Astroparticle Physics*, *2021*, 048. Retrieved from `https://ui.adsabs.harvard.edu/abs/2021JCAP...02..048A` doi: 10.1088/1475-7516/2021/02/048

Abramowski, A., Acero, F., Aharonian, F., Ait Benkhali, F., Akhperjanian, A. G., Angüner, E., … Balenderan (2013, November). Constraints on axionlike particles with h.e.s.s. from the irregularity of the pks 2155-304 energy spectrum. *Physical Review D*, *88*, 102003. Retrieved from `https://ui.adsabs.harvard.edu/abs/2013PhRvD..88j2003A` doi: 10.1103/PhysRevD.88.102003

Aghanim, N., Akrami, Y., Ashdown, M., Aumont, J., Baccigalupi, C., Ballardini, M., … Zonca, A. (2020, September). Planck 2018 results. vi. cosmological parameters. *Astronomy and Astrophysics*, *641*, A6. Retrieved from `https://ui.adsabs.harvard.edu/abs/2020A&A...641A...6P` doi: 10.1051/0004-6361/201833910

Ajello, M., Albert, A., Anderson, B., Baldini, L., Barbiellini, G., Bastieri, D., … et al. (2016, Apr). Search for spectral irregularities due to photon–axionlike-particle oscillations with the fermi large area telescope. *Physical Review Letters*, *116*(16). Retrieved from `http://dx.doi.org/10.1103/PhysRevLett.116.161101` doi: 10.1103/physrevlett.116.161101

Algaba, J. C., Asada, K., & Nakamura, M. (2016, June). Resolving the rotation measure of the m87 jet on kiloparsec scales. *The Astrophysical Journal*, *823*, 86. Retrieved from `https://ui.adsabs.harvard.edu/abs/2016ApJ...823...86A` doi: 10.3847/0004-637X/823/2/86

Alves, E. P., Zrake, J., & Fiuza, F. (2018, Dec). Efficient nonthermal particle acceleration by the kink instability in relativistic jets. *Phys. Rev. Lett.*, *121*, 245101. Retrieved from `https://link.aps.org/doi/10.1103/PhysRevLett.121.245101` doi: 10.1103/PhysRevLett.121.245101

Anastassopoulos, V., Aune, S., Barth, K., Belov, A., Bräuninger, H., Cantatore, G., … Collaboration, C. A. S. T. (2017). New cast limit on the axion-photon interaction. *Nature Physics*, *13*(6), 584–590. Retrieved from `https://doi.org/10.1038/nphys4109` doi: 10.1038/nphys4109

Arias, P., Cadamuro, D., Goodsell, M., Jaeckel, J., Redondo, J., & Ringwald, A. (2012). Wispy cold dark matter. *Journal of Cosmology and Astroparticle Physics*, *2012*(06), 013-013. Retrieved from `http://dx.doi.org/10.1088/1475-7516/2012/06/013` doi: 10.1088/1475-7516/2012/06/013

Baker, C. A., Doyle, D. D., Geltenbort, P., Green, K., van der Grinten, M. G. D., Harris,

P. G., … et al. (2006, Sep). Improved experimental limit on the electric dipole moment of the neutron. *Physical Review Letters*, *97*(13). Retrieved from `http://dx.doi.org/10.1103/PhysRevLett.97.131801` doi: 10.1103/physrevlett.97.131801

Bassan, N., & Roncadelli, M. (2009). *Photon-axion conversion in active galactic nuclei?*

Battesti, R., Béard, J., Böser, S., Bruyant, N., Budker, D., Crooker, S., … Zavattini, G. (2018, 03). High magnetic fields for fundamental physics. *Physics Reports*, *765-766*. doi: 10.1016/j.physrep.2018.07.005

Berg, M., Conlon, J. P., Day, F., Jennings, N., Krippendorf, S., Powell, A. J., & Rummel, M. (2017, October). Constraints on Axion-like Particles from X-Ray Observations of NGC1275. , *847*(2), 101. doi: 10.3847/1538-4357/aa8b16

Bähre, R., Döbrich, B., Dreyling-Eschweiler, J., Ghazaryan, S., Hodajerdi, R., Horns, D., … Willke, B. (2013, September). Any light particle search ii – technical design report. *Journal of Instrumentation*, *8*, T09001. Retrieved from `https://ui.adsabs.harvard.edu/abs/2013JInst...8.9001B` doi: 10.1088/1748-0221/8/09/T09001

Binggeli, B. (1999). The virgo cluster – home of m 87. In H.-J. Röser & K. Meisenheimer (Eds.), *The radio galaxy messier 87* (pp. 9–30). Berlin, Heidelberg: Springer Berlin Heidelberg.

Binggeli, B., Sandage, A., & Tammann, G. A. (1985, September). Studies of the virgo cluster. ii. a catalog of 2096 galaxies in the virgo cluster area. *The Astronomical Journal*, *90*, 1681–1758. Retrieved from `https://ui.adsabs.harvard.edu/abs/1985AJ.....90.1681B` doi: 10.1086/113874

Boldyrev, S., & Cattaneo, F. (2004, Apr). Magnetic-field generation in kolmogorov turbulence. *Physical Review Letters*, *92*(14). Retrieved from `http://dx.doi.org/10.1103/PhysRevLett.92.144501` doi: 10.1103/physrevlett.92.144501

Bonafede, A., Vazza, F., Brüggen, M., Akahori, T., Carretti, E., Colafrancesco, S., … Scaife, A. (2015, April). Unravelling the origin of large-scale magnetic fields in galaxy clusters and beyond through Faraday Rotation Measures with the SKA. In *Advancing astrophysics with the square kilometre array (aaska14)* (p. 95).

Borsanyi, S., Fodor, Z., Guenther, J., Kampert, K.-H., Katz, S. D., Kawanai, T., … Szabo, K. K. (2016). Calculation of the axion mass based on high-temperature lattice quantum chromodynamics. *Nature*, *539*(7627), 69–71. Retrieved from `https://doi.org/10.1038/nature20115` doi: 10.1038/nature20115

Cantiello, M., Biscardi, I., Brocato, E., & Raimondo, G. (2011, August). VLT optical BVR observations of two bright supernova Ia hosts in the Virgo cluster. Surface brightness fluctuation analysis. , *532*, A154. doi: 10.1051/0004-6361/201116667

Christenson, J. H., Cronin, J. W., Fitch, V. L., & Turlay, R. (1964, July). Evidence for the 2π decay of the k_2^0 meson. *PRL*, *13*(4), 138–140. Retrieved from `https://link.aps.org/doi/10.1103/PhysRevLett.13.138` doi: 10.1103/PhysRevLett.13.138

Churazov, E., Forman, W., Jones, C., & Böhringer, H. (2003, June). Xmm-newton observations of the perseus cluster. i. the temperature and surface brightness structure. *The Astrophysical Journal*, *590*, 225–237. Retrieved from `https://ui.adsabs.harvard.edu/abs/2003ApJ...590..225C` doi: 10.1086/374923

Collaboration, T. E. H. T. (2019). First m87 event horizon telescope results. i. the shadow of the supermassive black hole. *ApJL*, *875*(L1), 1-17. Retrieved from `https://iopscience-event-horizon.s3.amazonaws.com/article/10.3847/2041-8213/ab0ec7/The_Event_Horizon_Telescope_Collaboration_2019_ApJL_875_L1.pdf`

Conrad, J., Meyer, M., & Montanino, D. (2016, may). Axion-like particles from extra-galactic high energy sources. *Journal of Physics: Conference Series*, *718*, 052026. Retrieved from `https://doi.org/10.1088/1742-6596/718/5/052026` doi: 10.1088/1742-6596/718/5/052026

Dafni, T., O'Hare, C. A., Lakić, B., Galán, J., Iguaz, F. J., Irastorza, I. G., ... Ruiz Chóliz, E. (2019, Feb). Weighing the solar axion. *Physical Review D*, *99*(3). Retrieved from `http://dx.doi.org/10.1103/PhysRevD.99.035037` doi: 10.1103/physrevd.99.035037

Di Luzio, L., Giannotti, M., Nardi, E., & Visinelli, L. (2020). The landscape of qcd axion models. *Physics Reports*, *870*, 1–117. Retrieved from `https://www.sciencedirect.com/science/article/pii/S0370157320302477` doi: 10.1016/j.physrep.2020.06.002

Dominguez, A., Sanchez-Conde, M., & Prada, F. (2011, June). Axion-like particle imprint in cosmological very-high-energy sources. *Journal of Cosmology and Astroparticle Physics*, *2011*. doi: 10.1088/1475-7516/2011/11/020

Dress, W. B., Miller, P. D., Pendlebury, J. M., Perrin, P., & Ramsey, N. F. (1977, Jan). Search for an electric dipole moment of the neutron. *Phys. Rev. D*, *15*, 9–21. Retrieved from `https://link.aps.org/doi/10.1103/PhysRevD.15.9` doi: 10.1103/PhysRevD.15.9

Dyrda, M., Wierzcholska, A., Hervet, O., Moderski, R., Janiak, M., Ostrowski, M., & Łukasz Stawarz. (2015). *Discovery of vhe gamma-rays from the radio galaxy pks 0625-354 with h.e.s.s.*

Ellis, J. R., Gaillard, M. K., Nanopoulos, D. V., & Rudaz, S. (1981, Apr). Grand unification, the neutron electric dipole moment and galaxy formation. *Nature*, *293*, 41-43. 8 p. Retrieved from `http://cds.cern.ch/record/134376` doi: 10.1038/293041a0

Farina, M., Pappadopulo, D., Rompineve, F., & Tesi, A. (2017, Jan). The photo-philic qcd axion. *Journal of High Energy Physics*, *2017*(1). Retrieved from `http://dx.doi.org/10.1007/JHEP01(2017)095` doi: 10.1007/jhep01(2017)095

Feretti, L., Giovannini, G., Govoni, F., & Murgia, M. (2012, May). Clusters of galaxies: observational properties of the diffuse radio emission. *The Astronomy and Astrophysics Review*, *20*(1). Retrieved from `http://dx.doi.org/10.1007/s00159-012-0054-z` doi: 10.1007/s00159-012-0054-z

Finke, J. D., Razzaque, S., & Dermer, C. D. (2010). Modeling the extragalactic background light from stars and dust. *The Astrophysical Journal*, *712*(1), 238-249. Retrieved from `http://dx.doi.org/10.1088/0004-637X/712/1/238` doi: 10.1088/0004-637x/712/1/238

Gao, F., & Han, L. (2012). Implementing the nelder-mead simplex algorithm with adaptive parameters. *Computational Optimization and Applications*, *51*, 259-277.

G. G. Raffelt, F. R. H. J. T. W. P. M. M. R. N. B. H. N. N., D. M. Moltz. (1988). Construction and operation of an axion heiioscope. *Letter of Intent to the Fermi National Accelerator*

Laboratory.

Goldstone, J. (1961). Field theories with « superconductor » solutions. *Il Nuovo Cimento (1955-1965)*, *19*(1), 154–164. Retrieved from `https://doi.org/10.1007/BF02812722` doi: 10.1007/BF02812722

Gorman, W. M. (1960, July). Econometrics: An introduction to maximum likelihood methods. *Journal of the Royal Statistical Society: Series A (General)*, *123*(4), 494–496. Retrieved from `https://doi.org/10.2307/2343291` doi: 10.2307/2343291

Govoni, F. (2012). Observations of magnetic fields in intracluster medium. *Proceedings of the International Astronomical Union*, *10*(H16), 404-405. Retrieved from `https://www.cambridge.org/core/article/observations-of-magnetic-fields-in-intracluster-medium/9DEBD664B151F43FC5524BF22B8A381E` doi: 10.1017/S1743921314011739

Guidetti, D. (2011). *Magnetic fields around radio galaxies from Faraday rotation measure analysis* (Unpublished doctoral dissertation). Università di Bologna.

Halperin, I., & Zhitnitsky, A. (1998). Anomalous effective lagrangian and theta dependence in qcd at finite nc. *Physical Review Letters*, *81*, 4071-4074.

HE, X.-G., McKELLAR, B. H. J., & PAKVASA, S. (1989). The neutron electric dipole moment. *International Journal of Modern Physics A*, *04*(19), 5011-5046. Retrieved from `https://doi.org/10.1142/S0217751X89002144` doi: 10.1142/S0217751X89002144

Higaki, T., Jeong, K. S., Kitajima, N., & Takahashi, F. (2016). The qcd axion from aligned axions and diphoton excess. *Physics Letters B*, *755*, 13-16. Retrieved from `https://www.sciencedirect.com/science/article/pii/S0370269316000745` doi: https://doi.org/10.1016/j.physletb.2016.01.055

Hooper, D., & Serpico, P. D. (2007, Dec). Detecting axionlike particles with gamma ray telescopes. *Physical Review Letters*, *99*(23). Retrieved from `http://dx.doi.org/10.1103/PhysRevLett.99.231102` doi: 10.1103/physrevlett.99.231102

Jackiw, R. W. (2008). Axial anomaly. *Scholarpedia*, *3*(10), 7302. (revision #136939) doi: 10.4249/scholarpedia.7302

James, F. (1994). MINUIT Function Minimization and Error Analysis: Reference Manual Version 94.1.

Jones, C., & Forman, W. (1999, January). Einstein observatory images of clusters of galaxies. *The Astrophysical Journal*, *511*, 65–83. Retrieved from `https://ui.adsabs.harvard.edu/abs/1999ApJ...511...65J` doi: 10.1086/306646

Kass, R. E. (1989). The geometry of asymptotic inference. *Statistical Science*, *4*(3), 188–219. Retrieved from `http://www.jstor.org/stable/2245626`

Kravtsov, A. V. (2013, feb). THE SIZE-VIRIAL RADIUS RELATION OF GALAXIES. *The Astrophysical Journal*, *764*(2), L31. Retrieved from `https://doi.org/10.1088/2041-8205/764/2/l31` doi: 10.1088/2041-8205/764/2/l31

Kuster, M., Bräuninger, H., Cebrián, S., Davenport, M., Eleftheriadis, C., Englhauser, J., . . . et al. (2007, Jun). The x-ray telescope of cast. *New Journal of Physics*, *9*(6), 169–169. Retrieved from `http://dx.doi.org/10.1088/1367-2630/9/6/169` doi: 10.1088/1367-2630/9/6/169

Lea, S. M., Mushotzky, R., & Holt, S. S. (1982, November). Einstein Observatory solid state spectrometer observations of M87 and the Virgo cluster. , *262*, 24-32. doi: 10.1086/160392

Li, T. P., & Ma, Y. Q. (1983, September). Analysis methods for results in gamma-ray astronomy. , *272*, 317-324. doi: 10.1086/161295

Lucente, G., & Carenza, P. (2021). *Supernova bound on axion-like particles coupled with electrons.*

Malyshev, D., Neronov, A., Semikoz, D., Santangelo, A., & Jochum, J. (2018). Improved limit on axion-like particles from γ-ray data on perseus cluster..

Marsh, M. C. D., Russell, H. R., Fabian, A. C., McNamara, B. R., Nulsen, P., & Reynolds, C. S. (2017, December). A new bound on axion-like particles. *Journal of Cosmology and Astroparticle Physics*, *2017*, 036. Retrieved from `https://ui.adsabs.harvard.edu/abs/2017JCAP...12..036M` doi: 10.1088/1475-7516/2017/12/036

Massó, E. (2003, Feb). Axions and axion-like particles. *Nuclear Physics B - Proceedings Supplements*, *114*, 67–73. Retrieved from `http://dx.doi.org/10.1016/S0920-5632(02)01893-5` doi: 10.1016/s0920-5632(02)01893-5

Mei, S., Blakeslee, J. P., Cote, P., Tonry, J. L., West, M. J., Ferrarese, L., … Merritt, D. (2007, Jan). The acs virgo cluster survey. xiii. sbf distance catalog and the three-dimensional structure of the virgo cluster. *The Astrophysical Journal*, *655*(1), 144–162. Retrieved from `http://dx.doi.org/10.1086/509598` doi: 10.1086/509598

Meyer, M., Davies, J., & Kuhlmann, J. (2021, Jun). gammaalps: An open-source python package for computing photon-axion-like-particle oscillations in astrophysical environments. *Proceedings of 37th International Cosmic Ray Conference — PoS(ICRC2021).* Retrieved from `http://dx.doi.org/10.22323/1.395.0557` doi: 10.22323/1.395.0557

Meyer, M., Horns, D., & Raue, M. (2013). *First lower limits on the photon-axion-like particle coupling from very high energy gamma-ray observation.*

Meyer, M., Montanino, D., & Conrad, J. (2017, Jan). On detecting oscillations of gamma rays into axion-like particles in turbulent and coherent magnetic fields. *Journal of Cosmology and Astroparticle Physics*, *2014*(09), 003–003. Retrieved from `http://dx.doi.org/10.1088/1475-7516/2014/09/003` doi: 10.1088/1475-7516/2014/09/003

Moss, D., & Shukurov, A. (1996, March). Turbulence and magnetic fields in elliptical galaxies. *Mon Not R Astron Soc*, *279*(1), 229–239. Retrieved from `https://doi.org/10.1093/mnras/279.1.229` doi: 10.1093/mnras/279.1.229

Murgia, M., Govoni, F., Feretti, L., Giovannini, G., Dallacasa, D., Fanti, R., … Dolag, K. (2004). Magnetic fields and faraday rotation in clusters of galaxies. *Astronomy and Astrophysics*, *424*, 429-446.

Nambu, Y. (1960, Feb). Quasi-particles and gauge invariance in the theory of superconductivity. *Phys. Rev.*, *117*, 648–663. Retrieved from `https://link.aps.org/doi/10.1103/PhysRev.117.648` doi: 10.1103/PhysRev.117.648

Nulsen, P. E. J., & Bohringer, H. (1995, June). A rosat determination of the mass of the central virgo cluster. *Monthly Notices of the Royal Astronomical Society*, *274*, 1093–1106. Retrieved from `https://ui.adsabs.harvard.edu/abs/1995MNRAS.274.1093N` doi: 10.1093/mnras/274.4.1093

Opher, R. (1998, December). What is the Virial Radius of a Galaxy Cluster? In J. Paul, T. Montmerle, & E. Aubourg (Eds.), *19th texas symposium on relativistic astrophysics and cosmology* (p. 533).

Owen, F. N., Eilek, J. A., & Keel, W. C. (1990, October). Detection of large faraday rotation in the inner 2 kiloparsecs of m87. *The Astrophysical Journal*, *362*, 449. Retrieved from `https://ui.adsabs.harvard.edu/abs/1990ApJ...362..449O` doi: 10.1086/169282

Peccei, R. D., & Quinn, H. R. (1977, June). CP conservation in the presence of pseudoparticles. *PRL*, *38*(25), 1440–1443. Retrieved from `https://link.aps.org/doi/10.1103/PhysRevLett.38.1440` doi: 10.1103/PhysRevLett.38.1440

Pendlebury, J. M., Afach, S., Ayres, N. J., Baker, C. A., Ban, G., Bison, G., … Zsigmond, G. (2015, Nov). Revised experimental upper limit on the electric dipole moment of the neutron. *Phys. Rev. D*, *92*, 092003. Retrieved from `https://link.aps.org/doi/10.1103/PhysRevD.92.092003` doi: 10.1103/PhysRevD.92.092003

Preskill, J., Wise, M., & Wilczek, F. (1983). Cosmology of the invisible axion. *Physics Letters B*, *120*, 127-132.

Russell, H. R., Fabian, A. C., McNamara, B. R., & Broderick, A. E. (2015, July). Inside the bondi radius of m87. *Monthly Notices of the Royal Astronomical Society*, *451*, 588–600. Retrieved from `https://ui.adsabs.harvard.edu/abs/2015MNRAS.451..588R` doi: 10.1093/mnras/stv954

Schneider, P. (2008). *Einführung in die extragalaktische astronomie und kosmologie* (Korrigierter Nachdr. ed.). Berlin ; Heidelberg [u.a.]: Springer.

Sikivie, P. (1983). Experimental Tests of the Invisible Axion. *Phys. Rev. Lett.*, *51*, 1415–1417. ([Erratum: Phys.Rev.Lett. 52, 695 (1984)]) doi: 10.1103/PhysRevLett.51.1415

Sánchez-Conde, M. A., Paneque, D., Bloom, E., Prada, F., & Domínguez, A. (2009, Jun). Hints of the existence of axionlike particles from the gamma-ray spectra of cosmological sources. *Physical Review D*, *79*(12). Retrieved from `http://dx.doi.org/10.1103/PhysRevD.79.123511` doi: 10.1103/physrevd.79.123511

Stern, I. (2016, December). Admx (axion dark matter experim8ent) status.

Tikhonov, N. A., Galazutdinova, O. A., & Karataeva, G. M. (2020). *The distance to the giant elliptical galaxy m87 and the size of its stellar subsystem.*

Urban, O., Werner, N., Simionescu, A., Allen, S. W., & Böhringer, H. (2011, July). X-ray spectroscopy of the virgo cluster out to the virial radius. *Monthly Notices of the Royal Astronomical Society*, *414*, 2101–2111. Retrieved from `https://ui.adsabs.harvard.edu/abs/2011MNRAS.414.2101U` doi: 10.1111/j.1365-2966.2011.18526.x

Vacca, V., Murgia, M., Govoni, F., Feretti, L., Giovannini, G., Perley, R. A., & Taylor, G. B. (2012, April). The intracluster magnetic field power spectrum in a2199. *Astronomy and Astrophysics*, *540*, A38. Retrieved from `https://ui.adsabs.harvard.edu/abs/2012A&A...540A..38V` doi: 10.1051/0004-6361/201116622

Vogel, J. K., Avignone, F. T., Cantatore, G., Carmona, J. M., Caspi, S., Cetin, S. A., … Zioutas, K. (2013). *Iaxo - the international axion observatory.*

Walsh, J. L., Barth, A. J., Ho, L. C., & Sarzi, M. (2013, may). THE m87 BLACK HOLE MASS FROM GAS-DYNAMICAL MODELS OF SPACE TELESCOPE IMAGING

SPECTROGRAPH OBSERVATIONS. *The Astrophysical Journal*, *770*(2), 86. Retrieved from `https://doi.org/10.1088/0004-637x/770/2/86` doi: 10.1088/0004-637x/770/2/86

Weinberg, S. (1978, Jan). A new light boson? *Phys. Rev. Lett.*, *40*, 223–226. Retrieved from `https://link.aps.org/doi/10.1103/PhysRevLett.40.223` doi: 10.1103/PhysRevLett.40.223

Wilks, S. S. (1938). The Large-Sample Distribution of the Likelihood Ratio for Testing Composite Hypotheses. *The Annals of Mathematical Statistics*, *9*(1), 60 – 62. Retrieved from `https://doi.org/10.1214/aoms/1177732360` doi: 10.1214/aoms/1177732360

Wouters, D., & Brun, P. (2013, Jul). Constraints on axion-like particles from x-ray observations of the hydra galaxy cluster. *The Astrophysical Journal*, *772*(1), 44. Retrieved from `http://dx.doi.org/10.1088/0004-637X/772/1/44` doi: 10.1088/0004-637x/772/1/44

Wu, C. S., Ambler, E., Hayward, R. W., Hoppes, D. D., & Hudson, R. P. (1957, February). Experimental test of parity conservation in beta decay. *PR*, *105*(4), 1413–1415. Retrieved from `https://link.aps.org/doi/10.1103/PhysRev.105.1413` doi: 10.1103/PhysRev.105.1413

Declaration

Herewith I affirm that the submitted master thesis was written autonomously by myself and that I did not use any other sources and auxiliaries than declared in this work. Under the acknowledged rules of scientific work (lege artis) literal or analogous content borrowed from the work of others was appropriately identified. Furthermore, I insure that the submitted master thesis is not and was never part of any other examination procedures, either complete or in substantial parts.

Place, Date ……………………. Signature …………………….